ABSTRACT

DUAN, XIAOPENG. Device Design and Modeling for Beyond-CMOS Information Technology Based on Integrated Electronic-Magnetic Systems. (Under the direction of Prof. Ki Wook Kim.)

This thesis focuses on exploiting the correlation between insulating ferromagnets and 2-dimensional Dirac electronic systems in graphene and topological insulators (TI) to develop beyond-CMOS devices for information processing. The interdependence nature of magnetization and TI surface states is studied in detail. Resulting new devices could potentially be the building blocks for future information/communication systems.

These phenomena root in the exchange interaction between the surface magnetic moments and the electrons in a topological insulator surface channel or graphene. This highly correlated system makes it possible to control magnetization electrically, manipulate electron transport with magnetism and explore the coupled nonlinear dynamics. In particular, the switching of a mono-domain magnet is shown to be manipulated by the TI surface state with Fermi level modulation and a small spin current signal. Its operating reliability is verified by stochastic simulations. The resulting switching speed is within 1 ns and the power consumption is at the femtoJoule leve. This switching scheme is then applied in a circuit environment. We use TI for local magnetic manipulation and graphene as the spin channel to connect individual magnetic cells. The logic operations are demonstrated by a 1-bit full adder. We set up a fully coupled device-circuit simulation on top of the SPICE circuit simulator to evaluate the adder behavior. Correct logic operations are verified, with each adding process costing 2 ns and 15 fJ.

Apart from electrical control of magnetic rotations, the transport of TI surface electrons also shows unique characters under non-uniform exchange potential. Following the concept of quasi-optics of Dirac electrons, we investigated the electron transmission/reflection phenomenon at a magnetic boundary. A new type of anomalous Hall current is observed at the boundary. The results lead to the proposal of guiding electron propagation within an in-plane magnetic strip. It could be used to realize switchable interconnects and electron beam steering. The switching behavior for a switchable interconnect is evaluated in detail together with the design of a complementary inverter.

In some circumstances, both the magnetic impact on electron transport and the electrons' impact on magnetization have to be considered simultaneously, when neither of them has the dominant strength. By coupling the magnetization dynamics simulations and the TI surface current calculations, we have observed different phases of dynamic behaviors including reliable switches and steady oscillation. We found that the generation of the anomalous Hall current due to out-of-plane magnetization is the key to the unique dynamic behaviors. It induces the anti-damping effect, so that the final magnetization could align anti-parallelly with the driving

effective magnetic field, which was never expected before. This anti-damping effect could also result in steady oscillations at certain conditions. This ability makes it a very good spin wave generator.

Apart from the exchange interactions between TI and insulating magnets, magnetic metals bring another possible routine to exploit the correlations. When two magnetic electrodes are used to inject and absorb electrons with determined spin polarization, the transport phenomena would be nontrivial due to the unusual momentum distribution as a result of the spin-momentum interlock. Nonreciprocal electrical conductance is thus expected in the limit of infinitesimal forward and reverse biases between two spin selective electrodes. Based on the phenomenological model that include both ballistic and scattering transport, the estimated asymmetric ratio could reach several tens. The resulting ratchet like behaviors could enable radiation energy harvesting and find applications in ultra low voltage rectification circuits.

Device Design and Modeling for Beyond-CMOS Information Technology Based on Integrated Electronic-Magnetic Systems

by
Xiaopeng Duan

A dissertation submitted to the Graduate Faculty of
North Carolina State University
in partial fulfillment of the
requirements for the Degree of
Doctor of Philosophy

Electrical Engineering

Raleigh, North Carolina

2015

APPROVED BY:

Prof. David Aspnes	Prof. Robert Kolbas
Prof. Robert Trew	Prof. Ki Wook Kim Chair of Advisory Committee

DEDICATION

This dissertation is dedicated to my dear parents Guiqin Duan and Cuiying Li, who have loved and supported me no matter what.

BIOGRAPHY

The author was born on December 12, 1987, in Puyang, Henan, China. In June, 2010, he received his B.S. degree from the department of Electronic Science and Technology, Huazhong University of Science and Technology in Wuhan. There, he got the interest on the search for new mechanisms to process information. Two month later, he enrolled in the Ph.D. program in the Department of Electrical and Computer Engineering, at North Carolina State University. After serving as a teaching assistant for the first year, he worked as a research assistant supervised by Professor Ki Wook Kim. His research aims at designing the next generation of information and signal processing devices, enabled by newly discovered physics phenomena. The topics include magnetism, nanoelectronics, photonics and the the highly coupled heterostructures.

ACKNOWLEDGEMENTS

I am very thankful to my advisor Prof. Ki Wook Kim for his guidance during my graduate study. He has a wide and deep knowledge about electronic devices and the related physics theories. He taught me the rationales in research and how to form and complete a research idea. This work would not be possible without his guidance.

I would also like to thank Dr. Semenov. He is a very good physicist. Most of the work here is the result from our fruitful discussions. He has always been patient when I have troubles with the physics models.

I am also very thankful to my committee members: Prof. David Aspnes, Prof. Robert Kolbas and Prof. Robert Trew. I am very honored to have them in my committee. They have provided very valuable insights to my research and helped me to seek for more accessible ways of illustrations to promote our proposals.

Last but not least, I want to thank our group-mates as well: Dr. Byoung-Don Kong, Dr. Kostyantyn Borysenko, Dr. Xiaodong Li, Dr. Rui Mao, Zhenghe Jin, Namita Narendra and Xi-Lai Li. I have learned a lot from our discussions and broadened my views. We were always having great times together.

TABLE OF CONTENTS

LIST OF FIGURES

Chapter 1

Introduction

In the semiconductor industry, while fast development has occurred during the last several decades thanks to the continuous scaling of the silicon CMOS technology, it is widely realized that this trend may become questionable when the feature size of transistors reaches the physical limit. It is still unclear what technology can sustain the ever increasing computing power beyond the CMOS era. Facing this challenge, the International Roadmap for Semiconductors (ITRS) has categorized the current research activities into three directions, i.e. "More Moore" that tries to push CMOS to the ultimate limit, "More than Moore" that tries to integrate CMOS devices with other technologies to broaden the applications and "Beyond CMOS" that tries to find a new material and structural platform for future information processing technology.

For the beyond CMOS technologies, great effort has been devoted in searching for new materials to improve the channel properties and identifying new state variables to convey information. Particularly, the incorporation of electron spin into electronics (the "spintronics") has stimulated much excitation since the discovery of diluted magnetic semiconductors. [2, 3, 4, 5, 6] The hope was to get a ferromagnetic semiconductor so that the magnetization could be used to tune electronic properties through electron spin, and vise versa. At the same time, metallic based spintronic devices are also being extensively explored and greater research interest has arisen after the discovery of spin transfer torque (STT) and the giant spin Hall effect (GSHE). [7, 8, 9] Together with the well studied giant magnetoresistance (GMR) and tunneling magnetoresistance (TMR), several magnetic logic systems are realized. Most noticeably are the domain wall logic (DWL), multi-terminal magnetic tunneling junction (MTJ) based majority gate logic and the all spin logic (ASL). [10, 11, 12, 13]

The spirit of spintronics, as has been mentioned, is captured in the concept of controlling and propagating magnetization information by electric means. It requires both electronic and magnetic properties, together with their inter-correlation. While it is possible that both electronic and magnetic properties can be offered by one material system (e.g. magnetic semiconductor

and magnetic metal), it is often difficult to optimize both at the same time. For instance, diluted III-V semiconductors can hardly be made in p-type, and tantalum, which offers a very large spin Hall angle, has a high resistance. [5, 8] On the other hand, the combination of different materials through strong correlation may offer a promising path for magneto-electric integration. This makes it possible to optimize each property individually. One successful example is the multiferroic heterostructures, in which piezoelectric materials are combined with magnetostrictive materials and they couple together through strain to realize electrostatic control of magnetization. [14, 15]

Following this logic, we are particularly interested in the combination of ferromagnetic insulators with 2-dimensional Dirac electron gas, i.e. graphene and topological insulators (TI).

When graphene was first discovered, it immediately rose the interest in the electronic device community due to the extremely high electron mobility. [16] Yet the inability to turn off the channel due to Klein tunneling significantly hindered this progress. [17] While several prominent reports have shown the advantageous performance of graphene devices in RF (radio frequency) applications, where the advantages of symmetric electron-hole conductivity overweight the disadvantages of the high OFF current, how to exploit graphene in beyond-CMOS logic devices is still an open question. Until presently, most attempts for graphene based logic devices rely on finely trimmed edges to open a bandgap or to induce spin dependent behaviors. One such proposal of graphene based integrated circuit has been proposed and extensively studied in [18], but the precise control of edge type (Armchair or Zigzag) is still a tough task practically.

Thus, the high mobility along may not be a good starting point for designing a graphene device. The properties setting it apart from normal semiconductors/metals worth more attention. Firstly, it is the thinnest 2-dimensional electron gas (2DEG) so that the adjacent material would have a strong impact on the graphene electronic property, and vice versa. Secondly, it has a linear dispersion relation following the Dirac equation. In terms of electronic logic device utilities, one outcome is the readily proposed quasi-optic electron wave guiding devices that stems form the mathematical similarity between the two-spinor Dirac equation and Maxwell's equations; [19] another important consequence is that the density of state varies with the carrier density (or, equivalently, the chemical potential), while it is a constant in normal parabolic 2DEG. This means the susceptibility is now controllable with a voltage bias. Thirdly, the spin-obit coupling in graphene is extreme low, so that the electron spin relaxation time/length is very large (over over several micrometers). [20] It has been expected that the adoption of graphene as the spin channel for metallic spin logic circuit instead of copper would significantly improve the signal integrity.

These advantages apply to TI surface states as well except that the spin diffusion is effectively zero due to the spin-momentum interlock nature. [21, 22] The TI surface state is also described by the Dirac equation, but the two spinors of TI correspond to real electron spin,

instead of pseudospin due to valley dependence. This causes the spin to be locked to the momentum, which is a unique advantage of TI. First, its surface state is sensitive to magnetic exchange interactions that break the time reversal symmetry, while the back-scattering of non-magnetic impurity is depressed. [21, 22] Second, and more importantly, the electron spin can serve as a medium that couples magnetization to electronic states if an insulating magnetic is attached to the TI surface. The anticipated alteration of electronic structures has recently been observed on the Fe or Cr doped Bi_2Se_3 surfaces both experimentally and by first principle calculations. [23, 24, 25, 26] Thus the inter-dependence between TI surface transport properties and the proximate magnet magnetization is readily predictable. As a result, the magnetization affects TI surface transport properties and the spin polarized surface current also exerts an exchange field on the magnet, consisting a highly correlated magento-electric system. [22, 27, 28, 29, 30, 31]

For the combination of magnetic insulators and 2D electronic materials, an essential parameter is the interface exchange constant, which governs the efficiency of the coupling. While this is not a well characterized parameter, it is not without the relevant studies in the literature. A recent first principle calculation[32] reported a band gap of 54 meV in MnS capped Bi_2Se_3 (thus, the exchange coupling constant of 27 meV). Given the low Néel temperature of antiferromagnetic MnS (about 170 K), [33] significantly larger values can be expected for magnetic materials with higher Néel or Curie temperatures. Indeed, moderate magnetic doping of TI with Cr has shown a gap opening over 120 meV experimentally. [24] Moreover, a similar measurement in the closely related Ni-graphene structures resulted in the exchange bias field as large as 2000 Oe (between two thin Ni layers separated by graphene), [34] which corresponds to the proximity coupling constant of around 240 meV. Accordingly, one can reasonably anticipate G_0 to be in the tens to hundreds of meV at the well prepared TI/magnet or graphene/magnet interfaces.

Given these correlations between magnets and 2D electron systems, a list of controllable dynamic behaviors can be expected. The magnetic and electronic part become interdependent, i.e. one could be used to control the other by careful structural engineering. Several new device concepts are developed and extensively modeled following this rational. Chapter. 2 discusses the coupling between TI and an insulating monodomain nanomagnet. The dynamics of magnetic switching processes controlled by TI surface electronic states are evaluated following the Bennett clocking scheme. This scheme is then applied to develop an all spin logic platform in Chapter. 3, where TI and graphene are both attached to the magnets, offering local electrostatic magnetization control and spin propagation channel respectively. The transport properties of TI surface electrons is studied in Chapter. 4. Their applications in CMOS-like switching devices are simulated specifically.

These devices, for good controllability, has deliberately separated the magnetoelectric and electromagnetic dependence by choosing the right working regimes. A fully nonlinear scenario

that focuses on the magnetic-electric inter-coupling is also of great interest. This leads to a wide variety of dynamic behaviors, some of which are unique to the magnet-TI system, relying on the TI transport properties. Chapter. 5 discusses these phenomena in detail together with a review of the anomalous Hall effect in TI to validate the physical pictures.

Apart from the combination of insulating magnet and TI, Chapter. 6 presents the usage of metallic magnets as electrodes. Together with the spin-momentum interlocked electron transport on TI surface, the spin polarized injection/absorption results in nonreciprocal transport between two magnetic electrodes. The non-reciprocity is expected to be preserved even at infinitesimal bias. Chapter. 7 revisited the research rational and summarized the proposed devices in this thesis together with the discussion on prospective research. As each chapter in this thesis proposes one or several device ideas, they are made as self-contained as possible. So Chapter 2∼6 can be read separately each, while the logic of the whole research is illustrated here and in the summary chapter.

Chapter 2

Controlling nanomagnet magnetization with topological insulator surface states

2.1 Introduction

In this chapter, we exploit the coupling between TI and ferromagnetic insulators to assist and control magnetic switches, which is considered as one of the promising solutions for information processing beyond the current transistor based realm. In terms of magnetic switching devices, the most well developed technology in electric control of magnetization so far is the magneto-resistive random access memory (MRAM), [35] where the driving force for device operation has recently been shifted from the Ampere field to spin transfer torque (STT) of the spin polarized electric current. One near future expectation is the integration of high density electronic circuits and STT-MRAM, leading to the possibility of hybrid architectures. [36, 37] However, energy consumption continues to be a major problem as the critical current density generally remains high at around $10^6 - 10^7$ A/cm^2. [35] Recently, the giant spin Hall effect has shown the potential to improve the current to magnetization conversion efficiency, while the high resistance of the materials with large spin Hall factor is still a challenge. [8, 38] In fact, the spin momentum interlock of TI can be regarded as the extreme of a spin Hall effect: the electron spin is 100% polarized according to its momentum. Therefore, stronger effects can be expected.

In addition, another potential approach to lower the critical current for magnetic switches is to use the Bennett clocking approach; i.e., first bring the magnet to a neutral state with an external bias and then apply the signal current pulse to determine the final state. Traditionally, one of the mechanisms enabling this scheme is the strain tuned magnetic anisotropy in some multiferroic materials/structures, where variation in the tension can rotate the easy axis (thus,

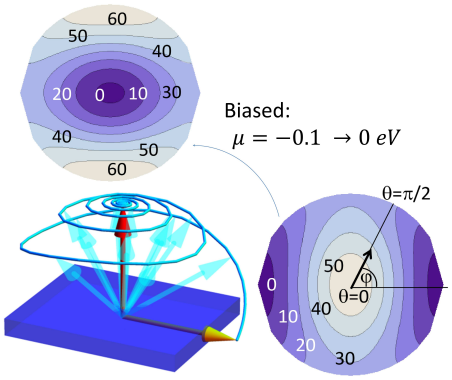

Figure 2.1: Free energy landscape in the FMI layer with different TI chemical potential conditions at 300 K (lower right: $\mu = -0.1$ eV, upper left: $\mu = 0$ eV). The iso-energy curves are calculated for a magnet of $50\times50\times2$ nm^3, $M = 4\pi \times 160$ G, and $K_1 = K_u = 0.05$ meV/nm^3. For the TI, Bi_2Se_3 is assumed as in Fig. A.2. The numerical values on the contours are in units of k_BT ($\simeq 26$ meV). Following the polar coordinate, $\theta = 0^\circ$ ($\theta = 90^\circ$) is at the center (the peripheries) of the circle. ϕ varies in the azimuthal direction. At $\mu = -0.1$ eV, two energy minima at the peripheries correspond to the in-plane easy axis (x). When the Fermi level is pushed to the Dirac point by a gate bias ($\mu = 0$ eV), the minima shift to the center ($\theta = 0^\circ$ and 180°), resulting in the out-of-plane easy axis (z). The change in the easy axis drives the magnetization to rotate from the in-plane to the out-of-plane orientations. The trajectory on the lower left is drawn according to the calculated data.

magnetization vector $\mathbf{M}$) of the ferromagnetic material by 90°. [39, 40, 41] Another mechanism utilizes the electron density dependence of the anisotropy that was reported in *3d* magnetic metals with the carrier mediated exchange interaction. [42] In terms of device stability/reliability, the mechanism based on the carrier distribution is favored as there is no structural change of any component. When an insulating ferromagnet is used with little or no free carriers, similar control of magnetic anisotropy can be envisioned by taking advantage of itinerant electrons (or holes) in an adjacent material and the subsequent surface exchange interactions with magnetic ions. [43, 44, 34, 45] Accordingly, the resulting effective magnetic field $\mathbf{H}_{ex}$ is a strong function of the carrier density at the interface with the magnetic layers rather than the electric current. [46, 47, 45] This property of $\mathbf{H}_{ex}$ combines the magnetic and electric responses inside the "meta-materials" in a strongly correlated manner that stems from the electrostatic and quantum mechanical nature of the exchange interaction. For this, the ideal choices are expected to be those with two-dimensional (2D) surface states for the possibility of strong interaction with the magnetic layers at the interface. Particularly, TIs offer a fascinating opportunity in spin magnetic applications owing to their spin-momentum entwined nature. [21, 22]

Here, we explore the magneto-electric properties of TI/ferromagnet hybrid structures for

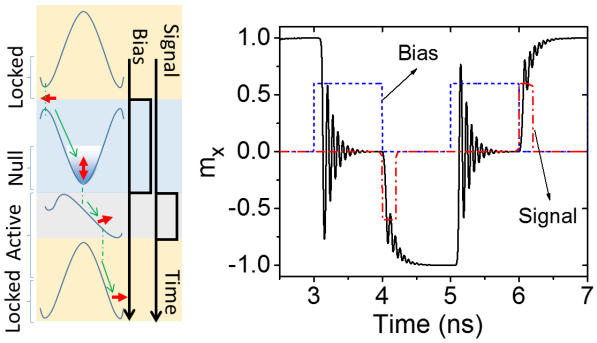

Figure 2.2: The schematic of Bennett clocking scheme (left) and the exemplary time resolved magnetic switching process in this operating scheme. The following parameters are used in this simulation: magnet size of $60 \times 60 \times 2$ nm^3, saturation magnetization $|\mathbf{M}| = 160$ Oe and hard axis anisotropy along $\hat{y}$ $K_y = 40$ fJ/μm^3, damping factor $\alpha = 0.1$, induced easy axis anisotropy along $\hat{z}$ $K_z = 0.08$ fJ/μm^2, interface coupling constant $G_0 = 40$ meV and 100% spin polarized signal current at 0.1 μA/nm.

effective modulation of magnetization via electric control. The theoretical model for the interaction between TI and ferromagnet has been established by Dr. Semenov (Appendix. A), focusing on the case where the properties of the TI influence the state of the magnet in the spirit of "meta-material" discussed earlier. Specifically, the exchange interaction of TI surface electrons is shown to appear in the form of effective magnetic anisotropy for the magnet that can be electrically tuned without any structural tension. In this chapter, we show that together with the intrinsic anisotropy terms and the demagnetization field, a transition of the easy axis from the in-plane to the out-of-plane directions (i.e., 90° rotation) can be stimulated by the variance of TI chemical potential. This transition of easy axis could result in a 90° magnetic rotation that constitute the neutralization process in Bennett clocking. Figure 2.1 schematically depicts this process. A spin polarized surface current could then serve as the signal to determine the relaxation direction and thus the final state. The ability to toggle the system between a normally unstable, neutral state and that along the easy axis (i.e., normally stable) on the flick of a bias is a key to realizing low-power spin logic devices with all electrical control presented here and in the next chapter.

2.2 Bennett clocking

The Bennett clocking [Figure 2.2] refers to the magnetic switching scheme that uses one clock to put the magnetization in a meta-stable state (the null stage) and another clock to apply the signal that generates a small tilt to determine the final state (the active stage). [48] If the first

clock that overcomes the barrier is applied electrostatically and the critical signal is small in absence of the barrier, this scheme is expected to offer very low energy consumption. Actually, the concept of Bennett clocking stems from the thermodynamic point of view on computation. When there is no barrier between two distinctive state, the deterministic transition can be induced with a driving energy of k_BTln2, where k_B is the Boltzmann constant and T is the absolute temperature. This is the thermal limit in a stochastic system according to the entropy theory. [48] Nevertheless, in a realistic situation, the final state after the barrier is recovered is important. Due to the finite duration of the driving force and the thermal fluctuation in the relaxations process, the integrity of this process is compromised so that the minimum energy required may be higher than the thermal limit, but still much lower than direct switches.

In the present device, the first stage of Bennet clocking is achieved electrically by applying a proper bias at the top gate. According to the derivation presented in Appendix. A, if the bias raises/depresses the Fermi level to the Dirac point, an increase of easy axis anisotropy along $\hat{z}$ upto 0.5 meV/nm^2 can be induced. For a normally sized nanomagnet (around 60×60 nm^2 in area), this correspond to $69k_BT$, which is sufficient to overcome a non-volatile barrier and set the magnetic easy axis to out-of-plane, resulting 90° rotation of the magnetization to the vertical orientation. Once the bias is withdrawn, it constitutes the meta-stable state in the Bennett clocking scheme. A current along the TI surface with intrinsic spin polarization can serve as the signal which provide the second effective magnetic field that tilts the magnetization slightly toward the desired relaxation direction (i.e., the active stage). The intrinsic anistropy field of the magnet would drive the magnetization relaxation process to the locked stable state after the current ends. Figure 2.2(right) shows the typical performance of a $60 \times 60 \times 2$ nm^3 magnet with saturation magnetization $|\mathbf{M}| = 160$ Oe and an additional hard axis along $\hat{y}$ of 40 fJ/μm^3.

2.3 Modeling method for magnetic switching dynamics

To model the dynamic behavior of magnetic switching processes, we adopted the well established phenomenological Landau-Lifschitz-Gilbert (LLG) equation. The bias induced anistropy variation is included in the total effective field term $\mathbf{H}_{\text{eff}}$ and an additional torque ($\mathbf{T}$) is added to account for the signal pulse for a deterministic 180° switches.

$$\frac{\partial \mathbf{m}}{\partial t} = -\gamma \mathbf{m} \times \mathbf{H}_{\text{eff}} + \alpha \mathbf{m} \times \frac{\partial \mathbf{m}}{\partial t} + \mathbf{T}, \tag{2.1}$$

where $\mathbf{m}$ is the normalized magnetization defined as $\mathbf{m} = \mathbf{M}/|\mathbf{M}|$, γ the gyromagnetic ratio, and α the Gilbert damping factor.

The magnet is treated similar to a Stoner-Wohlfarth model with mono-domain approxima-

tion. The total magnetic energy is considered to be composed of the space anisotropy (demagnetization energy), the intrinsic anisotropy term and the varying surface anisotropy anisotropy term due to the interaction with TI. We follow the ellipsoidal approximation for the space anisotropy term:

$$E_{sp} = 2\pi V M^2 \sum_{i,j} N_{ij} m_i m_j, \tag{2.2}$$

where the demagnetization factors $N_{ij} = N_i \delta_{i,j}$ and is calculated as

$$N_i = \frac{a_x a_y a_z}{2} \int_0^\infty \frac{dq}{Q_i \sqrt{Q_x Q_y Q_z}}\,. \tag{2.3}$$

with $Q_i = q + a_i^2$ and i, j denoting the coordinates x, y, z. $a_{x,y,z}$ are the ellipsoid principle axes, and for a magnet of size $60 \times 60 \times 2\text{nm}^3$, they are assumed to be $a_x = 60$ nm, $a_y = 60$ nm and $a_z = 2$ nm. Apart from the space anisotropy, we assumed another intrinsic hard axis anisotropy along $\hat{y}$:

$$E_{an} = K_y V m_y^2. \tag{2.4}$$

The total effect is an easy axis along $\hat{x}$ direction. The surface anisotropy gives the bias dependent energy term:

$$E_{surf} = -K_{eff} A m_z^2, \tag{2.5}$$

where $A = a_x a_y$ is the interface area between the magnet and TI. Note that Eq. 2.4 and Eq. 2.5 implicitly defines K_y to be the hard axis anisotropy value and K_{eff} for easy axis. This avoids adding minus signs in the numerical values in the following discussion. The total magnetization is thus the sum of the above terms:

$$E = E_{sp} + E_{an} + E_{surf} = \mu_0 M V \mathbf{H}_{eff} \cdot \mathbf{m}, \tag{2.6}$$

where the second equal sign shows the definition of the effective magnetic field $\mathbf{H}_{\text{eff}} = (\mu_0 M V)^{-1} \partial E / \partial \mathbf{m}$.

The torque term is treated in terms of the effect of an exchange field from electron spin polarization:

$$\mathbf{T} = \frac{\gamma G_0}{\mu_0 M_0 L_z} \langle \sigma_s \rangle \times \mathbf{m}, \tag{2.7}$$

where G_0 represents the coupling constant for the proximity exchange interaction in energy units, μ_0 the permeability constant, M_0 the saturation magnetization ($M_0 = |\mathbf{M}|$), L_z the thickness of the magnet, and σ_s the vector spin operator in the form of Pauli matrices. Here it is nontrivial that this effect is field like, in contrast to Sloncezwski term that appears in spin transfer torque. [7] This results in a dynamic behavior similar to magnetic field induced magnetization rotations instead of the processional switch in the STT case.

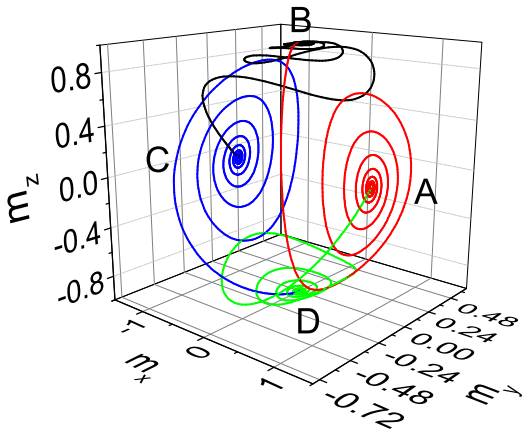

Figure 2.3: The trajectory of magnetic rotation path in the magnetization space corresponding to the exemplary switching behavior shown in Figure 2.2

More specifically, the electron spin polarization $\langle \sigma_s \rangle$ depends on the channel properties. In a TI surface channel, where the electron spin is locked to its momentum, the electric current $\mathbf{J} = (J_x, J_y, 0)$ polarizes electron spin [28] as $\langle \sigma_s \rangle = (-\frac{J_y}{ev_F}, \frac{J_x}{ev_F}, 0)$. In the present analysis, we designate the in-plane easy axis as the x direction for convenience and the TI surface current is along $\hat{y}$ so that $\langle \sigma_s \rangle \parallel \pm\hat{\mathbf{x}}$.

We numerically solve Eq. (2.1) using the Runge-Kutta method to characterize the switching dynamics. [49] A typical switching behavior is shown in Figure 2.2 (right). With the parameters outlined in the caption, the 90° rotation at the biasing stage finishes within 0.5 ns, which is composed of a direct magnetic flip followed by processional relaxation. Similar situation happens for the active stage with applied signal as well, except that the relaxation process continues after the signal ends. The magnetic trajectory is shown more clearly in the magnetic rotation path in the magnetization space in Figure 2.3. This confirms the similarity with the typical behaviors of magnetic field induced magnetic switches, which is a natural result from that all the involved interaction terms are field like.

One particularly interesting parameter that warrants additional scrutiny is the hard-axis anisotropy K_y along the y axis as it can significantly influence the details of magnetization dynamics. Our analysis suggests that the magnetization switches and relaxes faster with a larger K_y since it tends to confine the switching path to the x-z plane. We first examine its impact on the 90° rotation with m_x changing from 1 to 0 via the gate bias (see, for example, Figure 2.1 and Figure 2.2). As indicated in Figure 2.4a, K_y above approx. 20−30 fJ/μm^3 leads to the desired rotation within 0.5 ns. It should be noted that the application of hard-axis anisotropy in the y direction together with the demagnetization field amounts essentially to

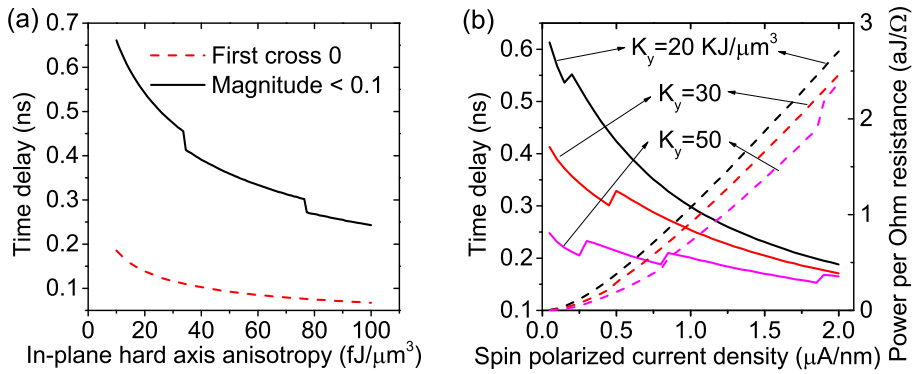

Figure 2.4: **a.** Impact of hard-axis anisotropy on the switching speed for a 90° magnetization rotation ($x \rightarrow z$) driven by the applied bias. The red dashed line represents the time when the oscillating **m** first crosses the z axis ($m_x = 0$), whereas the black solid line corresponds to the time when it essentially completes the rotation ($|m_x| < 0.1$). **b.** Time duration (solid lines) and corresponding power consumption (dashed lines) of the current driven relaxation process from $m_z = 1$ to $m_x = 1$ ($z \rightarrow x$) for the magnet with the dimension of $60 \times 60 \times 2$ nm^3. The relaxation is marked completed when $|m_x| > 0.9$. The power consumption per ohm is calculated as I^2t, where I is the total current assuming a 60-nm channel width and t is the duration of relaxation.

"the easy axis along the x direction", which has been assumed by numerous studies in the literature [13, 50]. Roughly speaking, the hard-axis anisotropy must be at least comparable to the demagnetization energy for the desired confinement effects on the switching dynamics.

The second half of the full 180° rotation is also improved by a larger hard-axis anisotropy as shown in Figure 2.4b. Here, a continuous signal current instead of a pulse is considered to drive the magnetization until it reaches the correct direction. Both the polarized current and the hard-axis anisotropy provide the driving force for relaxation, and the switching time drops when their values increase. At a small current density, the relaxation is mainly driven by the intrinsic anisotropy field so that the switching time varies significantly over different anisotropy values. As the current rises, the exchange torque also drives the switching process to reduce the switching time. When the current is high enough to dominate over the contribution from the anisotropy, the curves tend to converge (to approximately 0.1−0.2 ns). It is also worth noting that at a sufficiently large anisotropy (e.g., $K_y \gtrsim 50$ fJ/μm^3), the influence of signal amplitude becomes insignificant in the simulation range. The corresponding dashed lines indicate the energy consumption per ohm resistance. It shows a steep increase for switches with a high current even though the duration reduces. Accordingly, a large K_y appears to be generally favorable (i.e., for both fast switching and low energy consumption).

It is worth mentioning that the numbers displayed in Figure 2.4b actually overestimate

the power consumption as the envisioned device operation do not require the current applied during the entire relaxation process to the in-plane equilibrium. As indicated in Figure 2.2, a signal pulse is used to induce a tilt towards the desired direction and the rest of the rotation can be driven solely by the intrinsic anisotropy. This scheme reduces the power consumption as the duration of the applied current can be shorter. The robustness of the pulsed operation is analyzed in the following section.

2.4 Robust magnetic switches with TI surface current in Bennett clocking

For magnetic devices, it is always important to verify the operation robustness in a thermal bath. In the STT driven magnetic switching cases, a critical current exist as the current torque acts as an additional damping term that facilitate the correct relaxation once the magnetization passes the barrier; for magnetic field induced switches, the critical field is often treated as that overcomes the barrier and the duration of the applied field is normally long enough for the magnetization to sufficient relax. In contrast, the Bennett clocking scheme is composed of two 90° magnetization rotations and the second 90° rotation tries to take advantage of the self-relaxation to reduce the duration of the signal for low power consumption. Ideally, a tiny signal that tilts the magnetization slightly off the meta-stable state would be sufficient to determine the relaxation direction and thus the final state. However, the meta-stable state is very vulnerable to fluctuations. The magnetization may deviate from the perpendicular orientation due to therm fluctuations even if the system is full relaxed at the Null state. Thus the signal must overcome any possible deviations to ensure a robust switching process, which placed a lower limit of both duration and amplitude of the signal current. This section is devoted specially to statistically characterize the switching fidelity in a thermal bath. Possible engineering factors are investigated in detail.

In addition, we have not seen detailed study of magnetization dynamics driven by anisotropy variations and field-like signal torque in Bennett clocking operations so far, although the general performance of magnetic switch using magnetic field or spin transfer torque have been thoroughly studied. The analysis and results presented here would also apply to spin logic realizations in other material systems with with similar operating principles.

2.4.1 Possible error sources

In the magnetic switching process based on Bennett clocking, the switching errors are mainly caused by deviation from the meta-stable state as well as the low energy path leading to the energy minimum with unintended polarization. One such example is illustrated in Figure 2.5

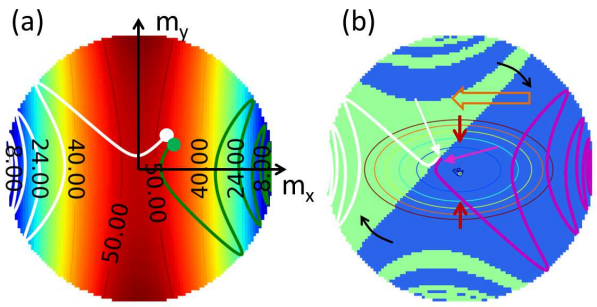

Figure 2.5: Switching characteristics related to the operation error rates. (a) Intrinsic energy landscape of the magnet that drives the relaxation after the signal pulse. The magnet has a dimension of $60 \times 60 \times 2$ nm^3 and hard y-axis anisotropy of 30 fJ/μm^3. The green line shows a path along which the magnetization relaxes to the same side of the initial state, while the white one indicates that a low energy valley can lead the magnetization to the opposite side. (b) Topology of switching success/failure with a signal current pulse of 0.2 ns at 0.2 μA/nm. The null-state magnetization that relaxes to $m_x = 1$ is shown in blue (success), while that led to $m_x = -1$ is marked in green (failure). The white and purple lines indicate the starting points of the two exemplary paths. The dot in the middle indicates the magnetization distribution at the end of a 0.5 ns biasing stage. The ellipses indicate the lowest energy contours with an increment of $2k_BT$ from the meta-stable state.

based on the magnetization phase-space analysis. As displayed by the white and green curves in Figure 2.5(a), two states with nearly identical locations in the intrinsic free energy landscape can end up with two drastically different relaxation pathes to opposite polarizations. This can be attributed to the convoluted and close entanglement in the high energy regions in the context of precessional dynamics[51]. Evidently, the rotational nature of magnetization switch adds complexities to the problem. Increasing the signal intensity, while certainly helpful, is only a part of the solution for the robust performance. Figure 2.5(b) summarizes the success/failure of the switching operation when a current pulse of 0.2 ns at 0.2 μA/nm is applied to set the state to $m_x = 1$. The darker colored (blue) region represents the initial "null" states from which the magnetization relaxes to the desired final state with the aid of signal current (i.e., $m_x = 1$; success), whereas the lighter region (green) results in the failure or error with the final polarization in the opposite direction ($m_x = -1$). An increased signal intensity moves the lighter/darker boundary towards the failure side (i.e., less failure; see the block arrow). The larger hard-axis anisotropy K_y, on the other hand, rotates the boundary clockwise (see the black arrows). Aside from the asymmetric pattern of the switching map, the concentric ellipses show the constant energy contours with an increment of $2k_BT$ from the meta-stable state. This gives a qualitative measure of random thermal fluctuation. For instance the trouble spot in

Figure 2.5(b) would be the lighter colored region within a given ellipse. Here, only the states with $m_z \geq 0$ are considered with its value determined by $\sqrt{1-m_x^2-m_y^2}$ in the 2D plot; the pattern for $m_z \leq 0$ satisfies the reflection symmetry.

To be more precise, two major sources can lead to the unintended spread in the null state distribution after the initial 90° rotation; namely, insufficient relaxation and thermal fluctuations. The former would dominate only if the operating frequency is too high, while the later always exists at the level of severity determined by the temperature. According to Figure 2.4(a), the switching time to the meta-stable state is well within 1 ns, indicating that the insufficient relaxation can easily be avoided. The exemplary case of Figure 2.5(b) clearly illustrates this point, where the applied bias of 1 ns sufficiently concentrates the distribution to the desired $|m_z| = 1$ state (see the tight distribution near the center). Consequently, the distribution of null state magnetization in a well designed operating condition will be determined by thermal fluctuations and errors would occur if the signal is not able to remedy all of the possible magnetization within this distribution including the added complexities in the precessional dynamics.

2.4.2 Error rate evaluation

The device robustness is closely related to the switching details. A conventional treatment to examine the performance in a realistic environment is to add a white thermal field to the LLG equation (stochastic LLG equation) that induces a Brownian motion by virtue of the correlation assumptions[52, 49]; i.e., $\mathbf{H}_{\text{eff}}^{'} = \mathbf{H}_{\text{eff}} + \mathbf{H}_{\text{th}}$. The random thermal field $\mathbf{H}_{\text{th}}$ is described by a Gaussian distribution with the variance determined from the fluctuation-dissipation theorem:

$$\langle H_{th}^{i}(t_1) H_{th}^{j}(t_2) \rangle = \frac{2k_B T\alpha}{\mu_0 V M_0 \gamma} \delta_{i,j} \delta(t_1 - t_2), \tag{2.8}$$

where V is the magnet volume and indices i, j correspond to the coordinate axes[52, 53]. As mentioned, this term can be readily included in the calculation. One major difficulty of the stochastic approach, however, is that the number of the required simulations increases at least linearly with the desired accuracy. For instance the simulations must be repeated 10^6 times or more in order to accurately estimate the error rate of 10^{-6} (i.e., one incorrect event out of 10^6 operations), not to mention the numerical complexities associated with various discretization issues in the actual implementation[54]. For an alternative, computationally more efficient method, it is worth noting that the magnet is most vulnerable to thermal fluctuation at the null state. Accordingly, we consider the thermal variation/noise explicitly through the null state magnetization distribution, while the relaxation dynamics is treated deterministically based on

the LLG equation. Then, the error rate P_s can be estimated as:

$$P_s = 1 - \int_{m_z \geq 0} d\mathbf{m}_\mathrm{n} R(\mathbf{m}_\mathrm{n}) F(\mathbf{m}_\mathrm{n}) / \int_{m_z \geq 0} d\mathbf{m}_\mathrm{n} F(\mathbf{m}_\mathrm{n}) \tag{2.9}$$

where $F(\mathbf{m}_\mathrm{n})$ is the distribution of the null state magnetization $\mathbf{m}_\mathrm{n}$ and $R(\mathbf{m}_\mathrm{n})$ denotes the simulated switching result. More precisely, $R(\mathbf{m}_\mathrm{n}) = 1$ if the operation results in the desired outcome and $R(\mathbf{m}_\mathrm{n}) = 0$ for the error/failure. Figure 2.6 shows the results of $R(\mathbf{m}_\mathrm{n})$ on the x-y plane for a number of cases. The plots clearly illustrate the earlier statement that the boundary between the failure and success regions moves towards the failure side when the signal current J increases and rotates clockwise when the hard-axis anisotropy K_y increases. As for $F(\mathbf{m}_\mathrm{n})$, we use a Boltzmann distribution to weigh each possible null state magnetization, i.e., $F(\mathbf{m}_\mathrm{n}) = \exp\left[-E_m(\mathbf{m}_\mathrm{n})/k_B T\right]$, where E_m represents the magnetic energy including the bias induced out-of-plane anisotropy. This choice can be justified since the thermal fluctuations would be dominant over the variation by insufficient initial relaxation under proper operating conditions (see the discussion in Section 2.4.B). Of the lowest energy contours plotted in Figure 2.6, it is interesting to note that nearly 90% of the thermal distribution is contained in the first $2k_B T$. The calculated error rates are shown in Figure 2.7 as a function of in-plane hard-axis anisotropy, magnet size, signal pulse duration, and the strength. From the results, it is evident that the device can reach the desired high degree of robustness once the hard-axis anisotropy becomes sufficiently large. In fact, K_y above approx. $20-30$ fJ/μcm^3 appears to converge without a large deviation between the different values. Accordingly, the threshold current density for a target error rate (say, 10^{-6}) is expected to be relatively insensitive to this crucial parameter [see Figure 2.7(a,b)]. When the magnet size increases, the switching becomes generally more reliable; this can be attributed to the larger surface area enabling a stronger interaction with the signal current. In the case of signal pulse duration, it shows a dependence akin to that of K_y. As can be seen from Figure 2.7**c**, the proposed device provides very comparable performances once the signal pulse is approx. 0.2 ns or longer. One key difference is that the error rate may exhibit a threshold behavior on the duration. Namely, there may be a minimum pulse length below which the operation cannot attain high fidelity even with an increase in the signal current strength (see, for example, the case of 0.1 ns). The requirement on the pulse duration may be partly compensated by a stronger in-plane hard-axis anisotropy. Figure 2.7(d) illustrates the point clearly, where the performance of the 0.1-ns case converges to an error rate similar to those of the longer pulses as the anisotropy energy increases beyond the demagnetization terms. An additional point of interest in Figure 2.7(d) is that the error rates for the longer pulses ($\gtrsim 0.4$ ns) seem to reach the minimum at around $K_y = 20$ fJ/μm^3 and then rise afterward with a converging trend in the end. This can be understood by examining evolution of the boundary discussed in Figure 2.5. The clockwise rotation may expose more thermally distributed region

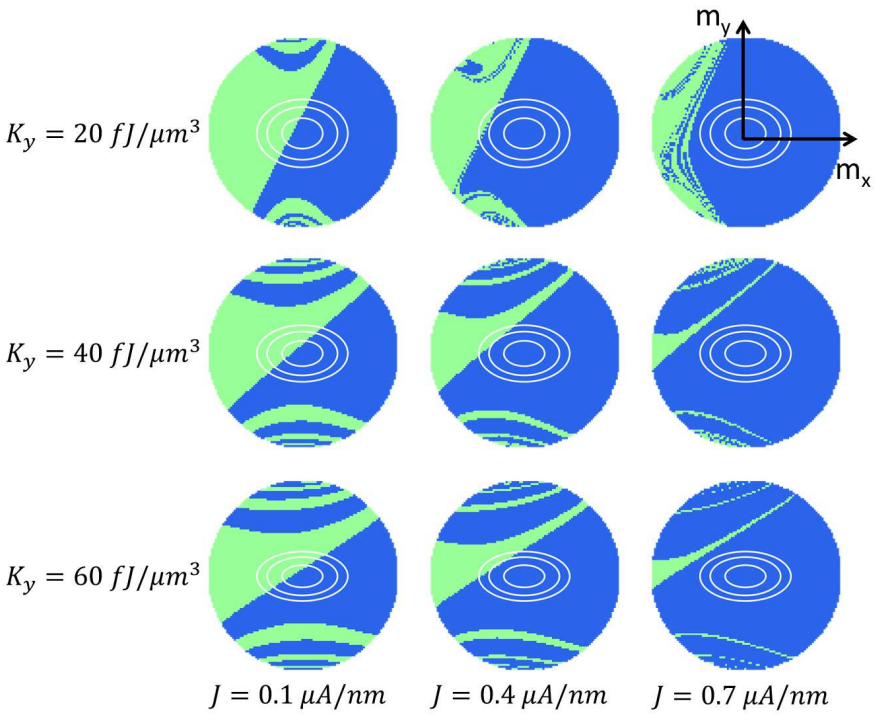

Figure 2.6: Topology of switching success/failure with a signal current pulse of 0.4 ns at different values of the strength J and anisotropy K_y. The null-state magnetization that relaxes to $m_x = 1$ is shown in blue (success), while that leads to $m_x = -1$ is marked in green (failure). The magnet has a dimension of $60 \times 60 \times 2$ nm^3. The ellipses indicate the energy contours of $2k_BT$, $4k_BT$, and $10k_BT$ from the meta-stable state.

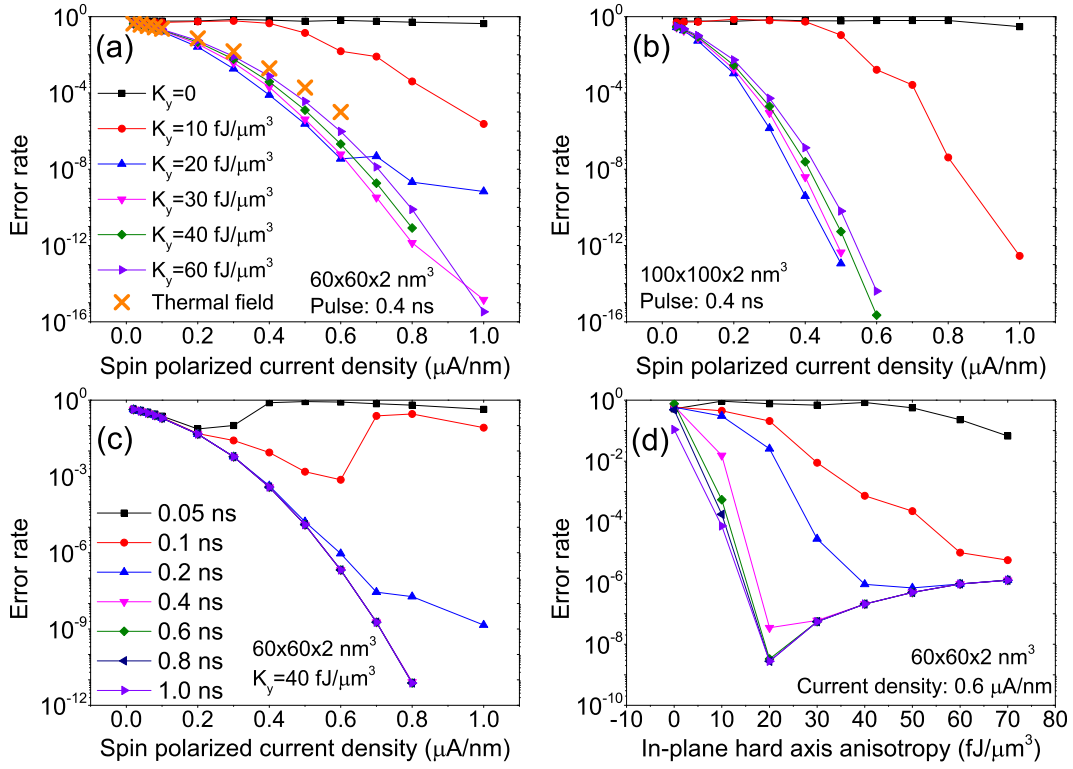

Figure 2.7: Variation of switching error rate over magnet size, signal current duration, signal current density, and hard-axis anisotropy. Identical line colors are used in (a) and (b) to denote different values of K_y, whereas (c) and (d) share the same notation on the pulse duration. The curves for pulse duration over 0.4 ns are almost identical in (c). The orange-colored data points in (a) represent the results from the random field approach with $K_y = 60$ fJ/μm^3. All other curves are obtained by considering the thermal distribution of the null-state magnetization.

to the failure part (note the lack of circular symmetry in the contours). Finally, a comparison is made with the results obtained by the conventional random field. As illustrated in Figure 2.7(a), both approaches show good agreement for the case of $K_y = 60$ fJ/μcm^3. The accuracy beyond 10^{-5} cannot be addressed in the white field treatment due to the limited number of simulation repeats (10^5).

The analysis of the robustness issues given above verifies the feasibility of the proposed devices. We can thus reasonably set the switching period to 1 ns, with 0.5 ns TI gate bias followed by 0.5 ns signal pulse, which is the chosen condition for the 1-bit adder simulation. Yet this does not stands for the optimized performance. First, the signal pulse duration can be reduced. The switching speed analysis (Figure 2.4) has shown that the switching time can easily reach around $0.2 \sim 0.3$ ns and the corresponding reliability is confirmed by the error rate

estimations (Figure 2.7). Second, the duration of the neutralization stage can also be significantly reduced given the thermal fluctuation is included. A tighter null stage magnetization distribution realized by a longer bias duration (without thermal field) would have no influence on the performance as long as it is tighter than the thermal distribution. Consequently, a total 180° switching period as short as 0.5 ns can be expected. The sub-nanosecond switching time is a very competitive performance considering the femtojoule level energy consumption, which is estimated at 0.6 μA/nm with assumed channel resistance at $1 \sim 10\text{k}\Omega$. This ensures an error rate below 10^{-6}. In addition, the built-in non-volatility appears attainable with little or no overhead to the performance specifications. The estimated free-energy barrier of the magnet under discussion ($60 \times 60 \times 2$ nm^3, 30 fJ/μm^3) is well over $40k_BT$.

2.5 Summary

The interface coupling between TI and adjacent magnet is exploited to realize electric control of magnetization switches. The switching process follows the Bennett clocking scheme, in which the barrier between stable in-plane magnetization states is overcome electrostatically by a gate bias that adjust TI surface chemical potential. A spin polarized TI surface current is used as the signal to determine the direction of relaxation. The switching dynamics is comprehensively studied to identify the minimum requirement on signal intensity and duration. A low power consumption is confirmed at the femto-Joule level with the switching period around 1 ns.

Although the calculation and analysis use the specific parameter values in the TI-FM hybrid system, the results and method apply to other material systems as long as the neutralization process is achieved by an effective anisotropy variation and the signal can be treated as a field-like term. This constitute the basis for the all spin logic constructed in the next chapter.

Chapter 3

Implementation of correlated magneto-electric systems in all spin logic

3.1 Introduction

Strong correlation between electronic and magnetic subsystems offers a significant opportunity in the development of low-power, highly-functional devices[42, 55, 56]. Particularly, the ability to induce and control the magnetic properties via an electrical means is a key enabling feature[56, 57]. Two-dimensional Dirac fermion states provide an ideal environment to facilitate effective coupling through the surface interactions with proximate materials[1, 20, 22, 27, 28, 58, 59, 60, 61, 62]. As has been demonstrated in the previous chapters, the interactions between ferromagnetic materials with graphene and TI are applicable to control magnetization rotations. While these investigated phenomena can be readily proposed as memory devices, the full potential of the highly correlated magneto-electric hetero-structures resides in logic applications.

By using magnetization/spin as additional state variables, one of the most promising approach is the all spin logic (ASL), which has been proposed in metallic magnetic/nonmagnetic systems. [13, 50] The idea is to propagate magnetization state in terms of the electron spin polarization that avoids the expansive conversion to electric signals. In the metallic realization, although Bennett clocking has been applied, electric current is used for both neutralizing the magnet and conveying the spin signal, because of which the Joule heating is still an limitation.

The essential operations in a magnetic/spin logic can be separated into manipulating and propagating the magnetization states. In this context, the topological insulator (TI) and graphene forms an excellent combination, each representing a unique extreme: [20, 22, 58] spin-manipulating

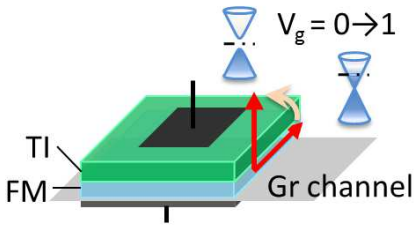

Figure 3.1: The basic component consists of a two-layer structure of topological insulator (TI) and ferromagnet (FMI) plus the control gates. With the gate bias, an effective out-of-plane anisotropy can be induced in the magnetic layer that rotates the magnetization by 90° from the in-plane orientation[1]. The graphene (Gr) channel interconnects the elemental cells.

and spin-conserving, respectively. The method of manipulating magnetization switches by TI surface states has been formulated in detail in the previous chapter, relying on the spin-momentum interlock nature. On the other hand, graphene has extremely weak spin-orbit coupling; the spin and the momentum can be treated as two independent quantum numbers and the spin relaxation length could reach several microns. [20] Plus, the two-dimensional nature of the graphene crystal enables strong surface interaction with a proximate ferromagnet (FMI) that can induce electron spin polarization. [59, 63, 61] The linear dispersion relation of graphene electrons also indicates that the induced spin polarization can be controlled electrostatically. [62]

Hence, the combination of TI, nanomagnet and graphene possesses ideal qualities to meet the two major requirements of logic device design: (i) manipulation of the desired information state variable (i.e., magnetization) by electrostatic control at the TI-FMI interface and (ii) robust propagation of information via the (FMI induced) spin polarization in the graphene interconnect. As no lattice displacement is involved, no risk of structural instability exists in contract to normal strain based multiferroic materials. Moreover, dynamical control of magnetic susceptibility and consequent logic reconfiguration offered by Dirac fermions [62] is difficult to be matched in the metal based spin circuits.

In this chapter, such a logic device is put forth and evaluated in detail. Section 3.2 outlines the overall operating principles following the Bennett clocking scheme. Two approaches for information transfer between adjacent cells are formulated and modeled in Sec. 3.3, followed by the discussion on logic circuit in terms of a 1-bit full adder (Sec. 3.4).

3.2 Spin logic operation principles

Starting from the well controlled 180° magnetic switch investigated in Chapter. 3, we need to decouple the signal from the direction of electron flow, i.e. the magnetic input signal that

determines the final state must be supplied by the preceding cell(s) in a circuit implementation. Accordingly, the structure is modified to include a graphene layer as the spin channel, as shown in Fig. 3.1, which consists of a FMI-TI stack placed on top of the graphene channel. Thus the top surface of the magnetic is coupled to the TI layer, which induces controllable in-plane to out-of-plane switch for the neutralization process in Bennett clocking. The bottom surface is coupled to the graphene layer, through which a propagating spin polarization could play the same role as the spin polarized current on TI surface in Chapter. 3 to determine the relaxation direction of a null state magnet. Consequently, the remaining problem in realizing a spin logic circuit is to generate the spin polarization signal through the graphene layer to propagate the information.

Here, it is important to note that the magnet used in this system needs to be insulating to avoid inducing unintended changes in electron density of both graphene and TI surface. Unlike metallic magnets that can directly inject polarized electrons into the interconnect medium to output the information, the insulating magnet does not have free carriers. Instead, the controllable surface exchange interaction at the FMI-graphene interface offers an alternatively mechanism to directly induce a spin dependent behavior in graphene that supports transfer of magnetization information. Specifically, two types of operations are possible; one with and the other without the involvement of electrical current flow. The first scheme relies on the spin dependent carrier transport induced by the exchange barrier at the FMI-graphene interface, while the other takes advantage of graphene electron mediated coupling between adjacent magnets. The corresponding physical pictures accounts for each outlined dynamics are detailed in the following.

3.3 Information transfer between adjacent cells

For an efficient spin logic implementation, it is preferred that the information is transferred in the form of electron spin polarization to avoid the intrinsically inefficient conversion to the electric current. One constraint, however, is the limited distance for reliable signals, which is set by the spin relaxation length. As such, transmission of the information is often accomplished in a cascade, where the state propagates cell by cell along the path. Thus, the issue of information transfer is essentially the interaction between the adjacent cells. At the same time, it is highly desirable if both duplication (COPY) and inversion (NOT) of the upstream spin state can be realized in each of the cascading stage with a relatively simple control and layout arrangement. These are the underlying principles that motivate the approaches described below. Another side note is that for large scale integrated circuit where signal may need to propagate from one functional unit to another over a large distance (over 10 μm), electron spin may not be a good information carrier due to the much faster decaying in comparison with electric signals and a

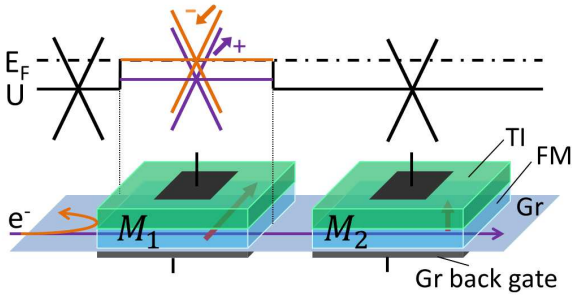

Figure 3.2: (a) COPY/NOT connection of two unit cells. The surface exchange interaction with the magnet induces a spin dependent barrier. By controlling electron transmission through the spin split bands (via the back gate bias at $\mathbf{M}_1$), spin polarization of electrons arriving at $\mathbf{M}_2$ can be selected.

large number of repeaters may be needed. Thus signal conversion may still be a necessity. The considerations here are constraint to the communication within a functional unit that performs a set of closely related logic and where adding several repeaters is not a big overhead.

3.3.1 Via spin polarized electrical currents

The unique advantage of graphene in maintaining electron spin polarization (i.e., the extremely weak spin-obit interaction) also makes it very difficult to realize electrical modulation of this information state variable. One possibility is to utilize magnetic impurities or defects that could locally enhance the spin-orbit coupling[20]. The surface exchange interaction between graphene and a magnetic material can introduce a similar effect with much greater control.

Such an impact of exchange interaction on graphene transport properties is modeled as spin dependent barriers. As shown in Figure 3.2, the exchange field raises the potential for spin projection antiparallel to the magnet magnetization ($-1/2$; a higher barrier $U+G_0$) and lowers that for the parallel spin ($+1/2$; a lower barrier $U-G_0$). The different barrier heights evidently translate to different transmission probabilities, resulting in a spin dependent conductance. A relevant theoretical account is given in ref. [59], where variation of the conductance was examined at the Fermi level. The transmission probability depends on the quantum state of electrons that induces the Klein tunneling phenomenon. The resulting expression, when an electron of energy E in the graphene channel encounters a potential barrier of U_g, is found to be[59]:

$$T = \frac{(\xi^2 - u^2)(1-u^2)}{(\xi^2-u^2)(1-u^2) + u^2(1-\xi)^2 \sin^2\left(k_F L\sqrt{\xi^2-u^2}\right)}, \tag{3.1}$$

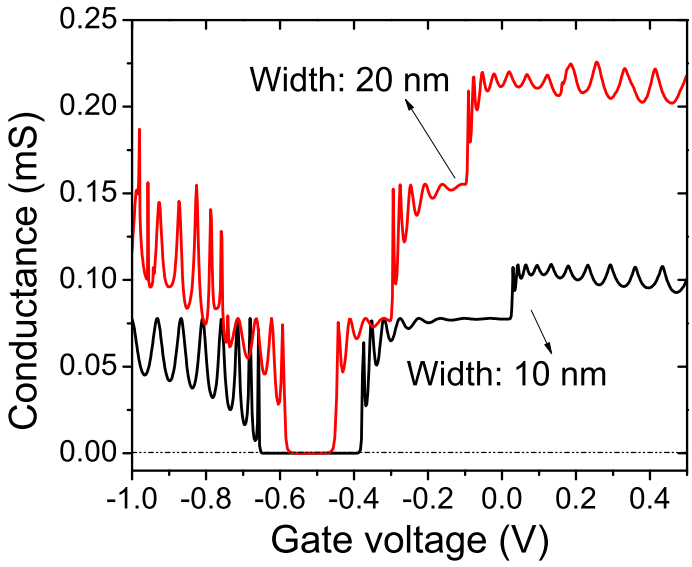

Figure 3.3: Calculated conductance of narrow graphene channels as a function of back gate bias that modulates the barrier potential. The graphene channel is assumed to have a intrinsic chemical potential of 0.3 eV and the gate capacitance is assumed to be $0.05\mathrm{F/m}^2$ which is connected in serial with the quantum capacitance of graphene. The interface exchange coupling constant with the magnet is assumed to be 40 meV.

where $\xi = (E - U_g)/E_F$ and $u = k_x/k$ ($k = \frac{|E|}{\hbar v_F}$; the magnitude of wave vector $\mathbf{k}$). In addition, the transverse wave vector (k_y) is quantized in a narrow channel. Assuming the vanishing/zero wave functions at/outside the channel boundaries (i.e., the extreme quantum limit), we can obtain $k_y = (n + 1/2)\pi/W$, where W is the channel width and the integer quantum number n is confined within $[0,\ kW/\pi - 1/2]$. Considering the contribution from multiple energy levels at a finite temperature and the valley degeneracy $g_v = 2$, the conductance of one spin channel is calculated in the Landauer-Büttiker formalism as

$$G(E_F, U_g) = g_v \frac{e^2}{\pi h} \int_{-\infty}^{\infty} dE \sum_n T(n, E, U_g) F(E, E_F, T) \tag{3.2}$$

where $F(E, E_F, T) = -\partial f(E, E_F, T)/\partial E$ and $f(E, E_F, T)$ is the Fermi-Dirac distribution.

Figure 3.3 shows the typical conductance behaviors. In a very narrow channel as intrinsically required by the nanoscale devices, the conductance shows a quantized behavior. The quantization step determined by the adopted extreme quantum limit ($= \pi\hbar v_F/W$)[64] is approximately 0.2 eV and 0.1 eV for the channel width of 10 nm and 20 nm, respectively. The conductance approaches zero when the bias depletes even the $n = 0$ state. Due to the spin splitting caused

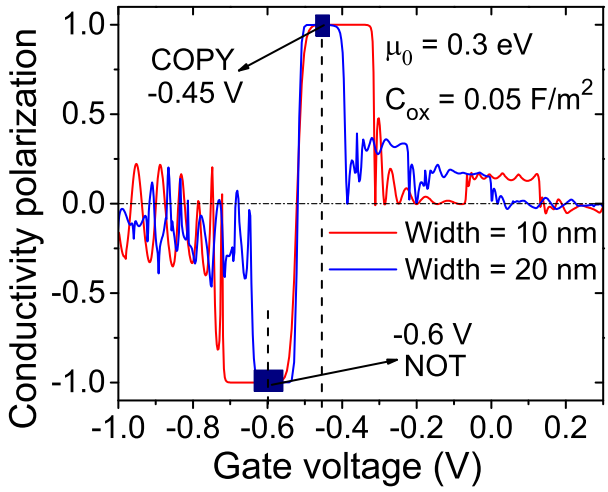

Figure 3.4: Calculated conductance polarization in the graphene interconnect as a function of gate voltage. The high polarization windows are marked by the filled rectangles.

by the exchange interaction with the adjacent magnet, the spin $-1/2$ state becomes depleted earlier in the conduction band than the spin $+1/2$ state while the opposite is the case for the valence band. The consequence is to open two windows for large polarization with opposite signs. Figure 3.4 shows the net polarization induced in the graphene channel as a function of gate voltage that is calculated as $P = (G^+ - G^-)/(G^+ + G^-)$, where $G^{+,-}$ denotes the conductance for spin $+1/2$ and $-1/2$ electrons, respectively. The polarizability P reaches almost 100% and the sign can be reversed by tuning the voltage. This means that the logic outcome of the circuit can be controlled dynamically by modulating biasing voltages instead of permanently constrained by the circuit layout.

In the computation of channel conductance polarization, one side point to note is that the quantum capacitance of graphene connected in serial with the gate capacitance [65] induces a non-linear relation between the gate voltage and the barrier potential. According to the voltage dividing principle, it satisfies

$$\left(V_g - \frac{E_F - E_{F0}}{q}\right) C_g = \frac{q}{\pi\hbar^2 v_F^2}\left(E_F^2 - E_{F0}^2\right), \tag{3.3}$$

where q is the unit charge, V_g the applied gate voltage, and C_g the gate capacitance that is normally around 0.05 F/m^3. E_{F0} and E_F denote the intrinsic and bias controlled chemical potential in graphene. As a result, the zero conductance window is broadened with a ratio inversely related to the gate capacitance. This can be used to tune the values for COPY/NOT control pulses.

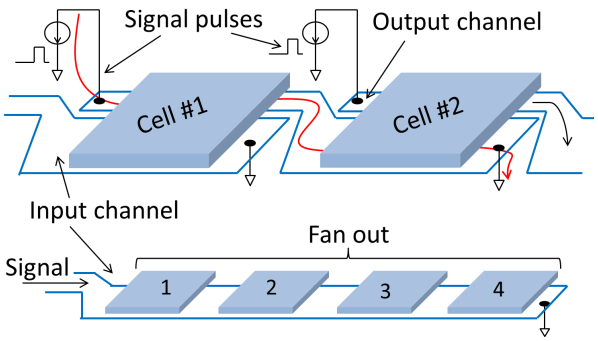

Figure 3.5: Separate input and output channels are defined for the information flow. The red curved arrow indicates the electron path between two neighboring cells. The fan-out is realized by placing multiple target cells along the same input channel.

The signal strength is determined by the spin polarization of the conductance, which is defined as the ratio of the difference between the two spin channel conductances over the total conductance. The results corresponding to Figure 3.3 are shown in Figure 3.4. The two windows for large polarization with opposite signs appear around the zero-conductance region as expected. The biasing voltage controlled COPY/NOT operations are confirmed.

One potential concern for this approach is the backward propagation of information, i.e., how to ensure that the spin polarized electrons flow only downstream. This can be addressed by patterning the graphene interconnect to separate the input and output channels as indicated in Figure 3.5. The output of the upstream cell is connected to the input in the downstream, forming an electron path indicated by the red curved arrow, where only the cells in the two neighboring stages are connected at a time. The asymmetric pattern with a wider input channel is to maximize the area of exchange interaction with the target magnet. For the fan-out, multiple cells can be placed along the same input channel to share the input, whose capacity is limited by electron spin relaxation. Given a typical relaxation length of 4 μm in graphene, [20] the upper limit may approach approximately 40. According to the reliability analysis discussed in Section. 2.4, the energy consumption for each COPY/NOT operation could be of the order of *femtojoules* that is dominated by the Joule heating from the signal current.

3.3.2 Via electron mediated exchange interactions

In contrast to the above approach, a fully electrostatic mechanism can eliminate the Joule heating and thus reduce the power requirement. As mentioned earlier, the magnetic susceptibility of graphene electrons can be modulated by a gate bias − a consequence of the linear dispersion relation. [62] This brings an opportunity to electrostatically turn on/off the effective exchange

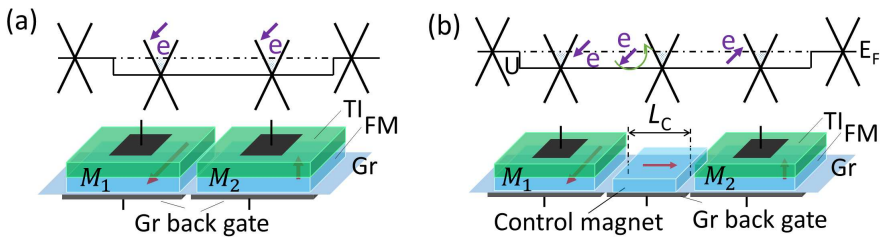

Figure 3.6: COPY (a) and NOT (b) operations in the curretless approach that are achieved via electrostatically controlled coupling between magnets when the downstream cell is in the Active state. An energy well can be introduced by simultaneously applying a bias to the graphene back gates. The gap between the gates can be ignored so long as it is smaller than the screening length which is typically several tens of nanometers in graphene.

coupling between adjacent magnets that is mediated by the graphene electrons in the channel. As shown in Figure 3.6, an electron potential well can be generated by the graphene back gate to facilitate the overlap of electron wave functions between the two involved cells to turn on the coupling. Qualitatively speaking, the upstream cell with a stable magnetization state ($\mathbf{M}_1 \| \pm\hat{\mathbf{x}}$) would induce electron spin polarization in the graphene channel that diffuses to the downstream cell. With negligible decay over the device dimension,[20] this aligns the target cell to realize the COPY operation [Figure 3.6(a)]. On the other hand, insertion of a control magnet ($\mathbf{M}_C$) in the middle (magnetized normal to $\mathbf{M}_1$) would cause spin precession as indicated in Figure 3.6(b). If its length is such that the spin experiences a 180° rotation when reaching the target cell, the anti-parallel alignment can be achieved for the NOT operation. The required distance for a π turn can be estimated as $L_C = \pi\hbar v_F/2G_0 \approx 26$ nm following the analysis described in an earlier study. [66] Note that the obtained L_C is well within the graphene electron mean free path.

The strength of the electron mediated coupling effect can be obtained by considering the induced change in the free energy of the system. For instance, the thermodynamic potential of graphene electrons is a function of magnetic states as:

$$E_c(\mathbf{m}_1, \mathbf{m}_2) = -k_B T \sum_{b,k} \ln \left\{ 1 + 2 \frac{\exp\left(\frac{E_F - E_{b,k}}{k_B T}\right)}{\left[1 + \exp\left(\frac{E_F - E_{b,k}}{k_B T}\right)\right]^2} \times \left[\cosh \frac{\Delta_k(\mathbf{m}_1, \mathbf{m}_2)}{k_B T} - 1\right] \right\}, \tag{3.4}$$

where E_F is the chemical potential, b ranges the conduction and valence bands and $2\Delta_k(\mathbf{m}_1, \mathbf{m}_2)$ corresponds to spin splitting in the graphene band caused by the exchange interaction with the

magnets. For convenience, the normalized magnetization vector (i.e., $\mathbf{m}_i = \mathbf{M}_i/|\mathbf{M}_i|$) is used as all magnets are assumed to have the same saturation magnetization. The expression clearly shows that the finite spin splitting always decreases the thermodynamic potential. Thus, the problem of finding the minimum $E_c(\mathbf{m}_1, \mathbf{m}_2)$ reduces to a search for the maximum energy splitting $\Delta_k(\mathbf{m}_1, \mathbf{m}_2)$. Subsequent calculations illustrate that the $\mathbf{m}_2 = \mathbf{m}_1$ state indeed provides the minimum E_c in Figure 3.6(a) (COPY), while it is a state near $\mathbf{m}_2 = -\mathbf{m}_1$ in Figure 3.6(b) (NOT). Appendix. B

The dependence of the free energy on the magnetization of the target cell ($\mathbf{M}_2$) may be best interpreted in terms of an effective field that determine its stable state. Adopting an approach commonly used in the magnetic system, the macroscopic field may be obtained as $\mu_0 \mathbf{H}^{\mathrm{sf}} = -\frac{1}{V_2} \partial E_c / \partial \mathbf{M}_2$ (where V_2 is the volume of the target magnet and μ_0 the permeability constant) that formally defines the orientation and strength of the spin signal. Figure 3.7 shows the calculated outcome for the NOT gate configuration ($L_{\mathrm{C}} = 26$ nm) as a function of E_F. The presence of both x and y components indicates that the energy minimum occurs slightly away from the antiparallel $\mathbf{m}_2 = -\mathbf{m}_1$ state. Nonetheless, the carrier mediated exchange interaction achieves inversion of the spin signal (i.e., polarization) as desired. The observed enhancement of the signal strength with E_F ensures a robust performance against thermal noise with an applied back gate bias. For instance, H^{sf} of approx. 1250 Oe can realize the error rate below 10^{-6} which equals the effective field corresponding to a spin polarized current of 0.6 μA/nm discussed in Section. 2.4. The necessary shift of 0.1 eV in E_F from the Dirac point translates to the back gate voltage swing of about 0.12 V. The corresponding energy requirement is approximately 10 aJ per COPY/NOT operation including the amount needed to prepare the target cell in the Bennet clocking scheme. Moreover, with only capacitor charging/discharging, a significant portion of this energy can be recovered in the clock network.[67] Accordingly, the net consumption may be reduced to the attojoule level. In this scheme, it is advantageous to have an intrinsically depleted graphene channel unlike the mechanism based on the spin polarized current.

To access the reliability of this approach, since the magnetic switch follows the same dynamics as that characterized for the current driven case, the critical field strength for a reliable operation can be found by referring to the critical signal current density. Adopting $J = 0.6$ μA/nm, the corresponding effective field gives around 1250 Oe. This is further verified by simulated switching result with $H_x = 1500$ Oe, $H_y = -280$ Oe as shown in Figure 3.8 as a function of the neutral state magnetic configuration in the target cell. The estimated error rate is less than 10^{-7}.

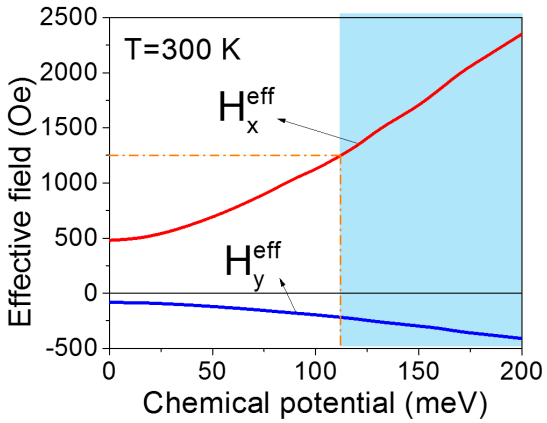

Figure 3.7: Effective field exerted on the downstream cell as a function of chemical potential in the graphene channel. The shaded region indicates the condition for error rate below 10^{-6}.

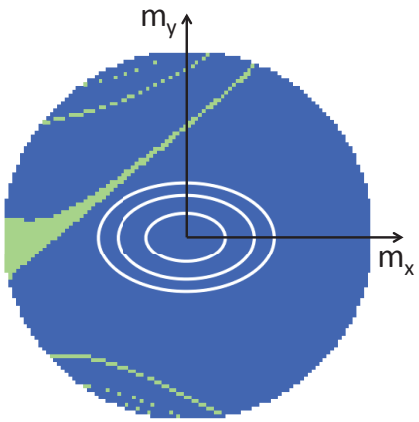

Figure 3.8: Topology of switching success/failure with the effective field of $H_x^{\text{eff}} = 1500$ Oe , $H_y^{\text{eff}} = -280$ Oe. The null-state magnetization that relaxes to $m_x = 1$ is shown in blue (success), while that led to $m_x = -1$ is marked in green (failure). The ellipses indicate the energy contours of $2k_BT$, $4k_BT$, and $10k_BT$ from the neutral state. The magnet has a dimension of $60\times60\times2$ nm^3 with a hard axis anisotropy $K_y = 40$ fJ/μm.

3.4 Construction of logic circuits

Once the elemental cell and the cell-to-cell COPY/NOT operations are established, the rest of the Boolean logic can be built on the spin logic platform with majority gates. [13, 68, 69, 70] Generally for a majority gate accepting $2l+1$ inputs, the logic output $M_{2l+1}(a_1, a_2, ... a_{2l+1})$ can be expressed as the union of all possible intersections of $l+1$ inputs. It returns true if and only if more than 50% of the inputs are true. Specially for a 3-input majority gate, we have $M_3(a_1, a_2, a_3) = a_1a_2 + a_1a_3 + a_2a_3$.

Following the majority logic approach, a simple estimation can show that the power consumption and circuit complexity are related linearly. We consider the worst case for the critical total current to ensure the intended functionality, which is identified to have one of the inputs opposite to the other two, e.g., $a = 1$, $b = 1$, $c = 0$. Assuming that logic state "1" corresponds to the magnetization along the $+x$ direction (i.e., high channel conductance for spin $+1/2$ electrons), the total conductance for the spin "$+1/2$" channel is $2G_H + G_L$ while that for the spin "$-1/2$" channel is $G_H + 2G_L$. Here G_H (G_L) represents the higher (lower) conductance value (or, equivalently, current) for the preferred (not preferred) spin. This results in the total polarization of $\frac{G_H - G_L}{3(G_H+G_L)} \approx \frac{1}{3}$ to write the C_{out} cell at the first clock (CLK1). Similarly, the electron polarization to write the S cell at the second stage (CLK2), which is effectively a 5-input majority gate, is only about $\frac{1}{5}$. As a result, the current necessary to achieve the set-level of the spin signal strength (i.e., spin polarized current) must increase proportionally with the number of inputs. Given the parallel connections of these inputs, the power consumption would also increase approximately linearly.

In this section, a concrete example is given in terms of a 1-bit full adder. The circuit layout are proposed for both information transfer approaches and the circuit simulation is discussed in detail base on the spin current approach.

3.4.1 Layout of a 1-bit adder

For a 1-bit full adder, it is important to note that the 1-bit adder logic can be decomposed to two majority gate logic components: the carry-out bit (C_{out}) is the majority gate of inputs a,b,c, and the sum bit (S) equals to a five-input majority logic of a,b,c, and two $\overline{C_{out}}$'s.

In a 1-bit full adder with inputs a,b,c, the output of the carry-out bit c_{out} is $ab + ac + bc$ that is exactly a majority logic as $M_3(a, b, c)$. The sum bit S has also been identified [50] as a majority gate logic with 5 inputs consisting of a, b, c and two $\overline{c_{out}}$'s. It can be proven with

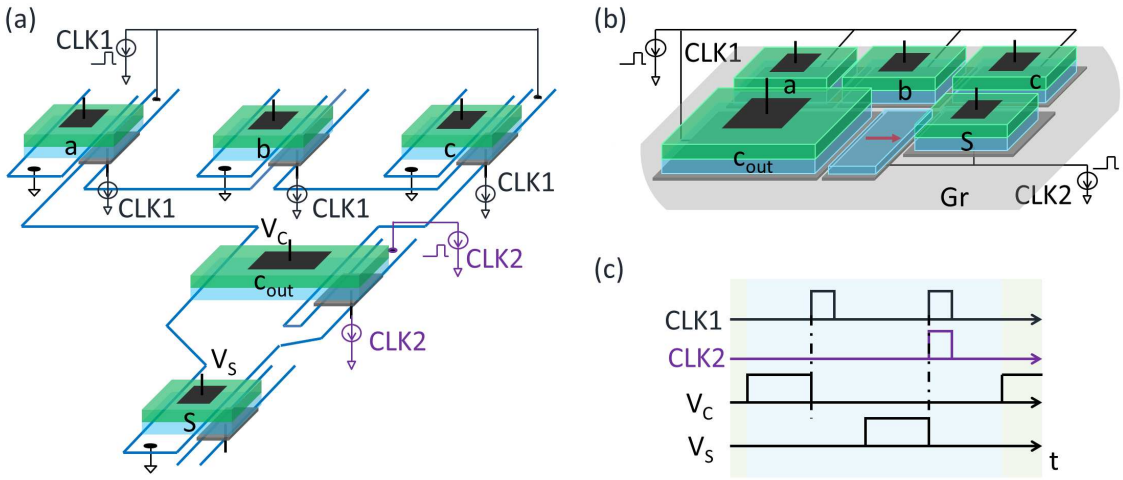

Figure 3.9: (a) Circuit layout of a 1-bit full adder based on spin polarized current through the graphene channel. A doubled strength of the outgoing signal from C_{out} (specifically, $\overline{c_{out}}$) can be achieved by adjusting the cell size or the channel driving voltage. (b) Tentative circuit layout for the 1-bit adder in the currentless approach. It uses the same control clocks and follows the 2-stage operation as in the current driven design. (c) The clocks and control signals. Two channel clock supplies (CLK1, CLK2) are used together with the corresponding biases on the TI gates. The graphene gate biases are synchronized with the channel clock, while the values are set independently according to the function.

Boolean algebra as following:

$$\begin{aligned} S &= abc + a\bar{b}\bar{c} + \bar{a}b\bar{c} + \bar{a}\bar{b}c \\ &= abc + (a+b+c)(\bar{a}\bar{b} + \bar{b}\bar{c} + \bar{a}\bar{c}) \\ &= abc + (a+b+c)\bar{M}_3 \\ &= abc + (a+b+c+ab+ac+bc)\bar{M}_3 \\ &= abc + a\bar{M}_3\bar{M}_3 + b\bar{M}_3\bar{M}_3 + c\bar{M}_3\bar{M}_3 \\ &\quad + ab\bar{M}_3 + ac\bar{M}_3 + bc\bar{M}_3, \end{aligned} \tag{3.5}$$

Based on this logic formulation, Figure 3.9 shows 1-bit adder layouts to accomplish the two-stage operations. The designs based on the spin current and electron mediated coupling share the same clocking scheme as shown in Figure 3.9c. For the spin current based case, electrons are injected by clock CLK1 through a,b,c cells to set the state of C_{out} at the first stage. The second stage also includes another clock CLK2 to inject electrons through the output channel of C_{out} with reversed polarization (i.e., $\overline{C_{out}}$). Reversing the polarization is controlled by the value of

applied graphene gate bias and doubling the C_{out} signal can be achieved by either adjusting the cell size or increasing the driving voltage at in the corresponding output channel. On the other hand, construction of logic circuits based on this current-less operating mechanism is essentially arranging each elemental cell on a universal graphene sheet with properly clocked gates. It follows a different methodology compared to the current based circuits. One characteristic is the compact layout required by the nature of local exchange interactions. A tentative 1-bit adder design is shown in Figure 3.9b following the same two-stage operating scheme. In the first stage, CLK1 induces the electron wave function overlap in the graphene channel under input cells and output cell C_{out} to achieve a 3-input majority gate. The next stage has CLK1 and CLK2 applied together to overlap all the cells for the equivalent 5-input majority logic. The inserted control magnet inverts the signal from C_{out} to $\overline{C_{out}}$. In the actual implementation, however, this trial design may need adjustments as it is based on the assumption that the outcome from our two-cell analytic prediction holds for the complex geometry at least qualitatively.

In the rest of this chapter, we focus on the spin current approach and evaluate in detail the circuit performance of the 1-bit adder.

3.4.2 Circuit model and circuit simulation

A circuit model is developed to assess the circuit performance of the device prototype with a number of simplifying assumptions. More specifically, each device is treated as a set of bias and magnetization controlled resistors. Spin relaxation in the graphene interconnect is not considered due to the short length/transit time between the two neighboring cells. Hence, two spin channels (i.e., $+1/2$ and $-1/2$) are considered independent. This leads to the equivalent device model shown in Figure 3.10(a) that depicts a 10-terminal abstraction consisting of four resistors and two gates. The resistors represent the resistance for spin $+1/2$ ($-1/2$) electrons in the input R_i^+ (R_i^-) and output R_o^+ (R_o^-) channels; see Figure 3.5 for the interconnect layout. The resistance values are determined by Eq. 3.2 as a function of the magnetization state and the bias potential barrier. The graphene back gate is applied to directly control the output (reading) channel resistance ($R_o^{+,-}$), while the input (writing) channel is unaffected by this electrode as indicated in Figure 3.9(a). The TI (i.e., top) gate impacts the resistance through modulation of the magnetization state. The applied bias pulses following the Bennett clocking scheme rotate the magnetization easy axis from in-plane to out-of-plane.

The resulting equivalent circuit model for the one bit adder is shown in Figure 3.10 which is simulated by coupling the SPICE circuit simulator with device simulations. This simulating frame work is shown in Figure 3.11. It is accomplished by implementing the extracted circuit model for each unit cell [Figure 3.10(a)] as a XSPICE user defined model in the ngSpice package. The device model contains a LLG solver to simulate the magnetization dynamics and conduc-

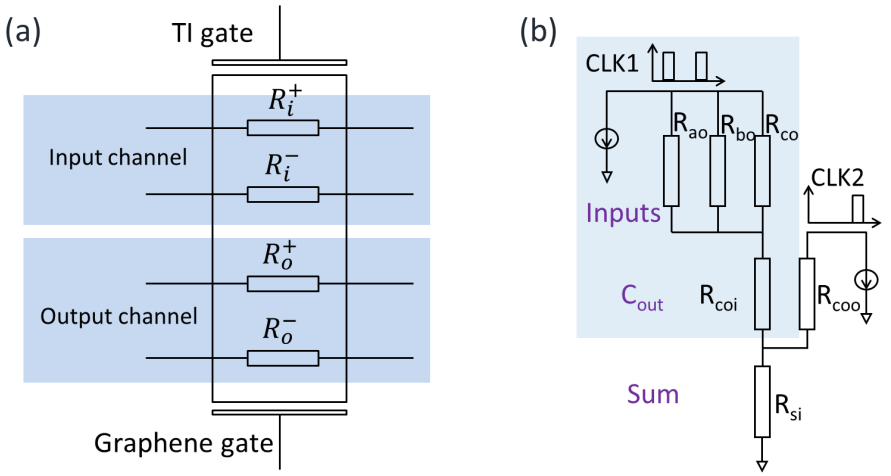

Figure 3.10: (a) Circuit model for one device cell. Two spin ($\pm 1/2$) channels are considered independent for both input and output, resulting in 4 resistors. The resistances are determined by the bias applied to the graphene back gate and the magnetization state. The back gate bias is synchronized with the signal current. The bias pulse applied to the TI top gate in a Bennett clocking scheme controls the 90° rotation. The magnetization dynamics is solved together with the transient circuit simulation. (b) Equivalent circuit of the 1-bit adder shown in Figure 3.9(a). The shaded part indicates the 3-input majority gate at the first stage. Each cell is represented by its resistance that is driven by the first pulse of CLK1. CLK2 is synchronized with the second pulse of CLK1 to drive the second stage at which the entire circuit is active, realizing a 5-input majority logic. The spin dependent conductance is treated separately at each resistor, while the total current is used for the circuit simulation at each node.

tance solver based on the Landauer-Büttiker formalism to get the conductance according to biasing and magnetic conditions. In each step of transient simulation, the magnetization state is updated according to the LLG solver and the result is used to determine the conductance values. These values are then adopted in the circuit simulation. Thus, our procedure realizes a circuit-device co-simulation, as adopted in other numerical studies of spin logic circuits, [50, 71] plus a real-time LLG solver.

Using this simulation setup, the adder behavior is verified with ten successive add operations that covers the truth table (Figure 3.12). In this simulation, we assumed all the magnets have the same parameters as previously stated and the input/output channels are divide with a ratio of 4:1. The input channel driving voltage is set to 0.3 V and increased to 0.45 V to double the signal from C_{out}. The graphene gate voltages are chosen according to Figure 3.4, -0.45 V for COPY and -0.6 V for NOT. The magnetic switch is set to a period of 1 ns, and each adding process thus finishes in 2 ns. The period of 3 ns shown here include the process of setting the input magnet states explicitly. In this exemplary condition, the total channel current is around

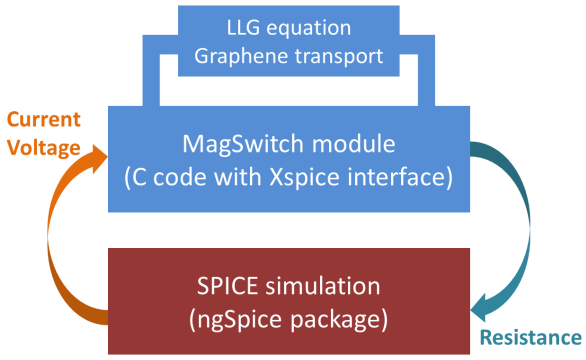

Figure 3.11: Schematic illustration of the simulation frame work.

$30 \sim 80$ μA and the resulting power consumption for each adding process is around 15 fJ due to Joule heating of the signal current with 0.5 ns pulses.

3.5 Summary

In summary, we have demonstrate the implementation of hybrid FMI-Dirac electron systems in all spin logic platform. The unique properties of each material is exploited. The coupling between FMI and TI is for local magnetization manipulation, taking advantage of the spin momentum interlock of TI; the coupling between FMI and graphene is used as the spin channel to support magnetic information propagation. The resulting logic circuit is illustrated in terms of a 1-bit full adder and a fully coupled device-circuit simulation is developed to evaluate the performance. Low power consumption is confirmed. In addition, we note that while the Boolean logic is realized to demonstrate the logic application here, other non-Boolean logic like the cellular automata and/or neuromorphic computing may also be possible, taking advantage of the dynamically configurable information transfer schemes.

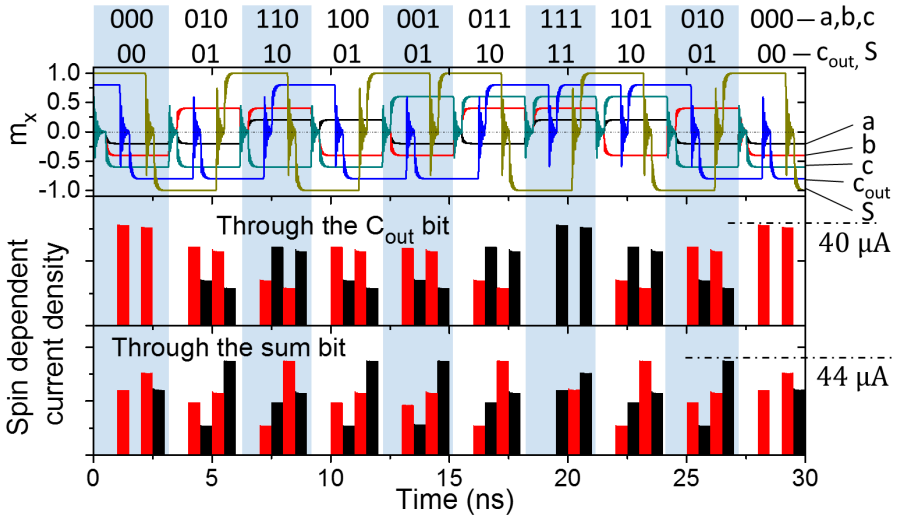

Figure 3.12: Results of ten add operations performed with the input states set dynamically in the simulation. The top panel shows the magnetization of each cell and the bottom two provide the spin parallel ($\hat{\mathbf{x}}$, black/darker) and spin anti-parallel ($-\hat{\mathbf{x}}$, red/lighter) currents through the input channels of C_{out} and S, respectively. The magnetization m_x varies between 1 and -1 in all five cases (e.g., $m_x = \pm 1$ for logic "1" and "0", respectively). The heights are adjusted artificially to distinguish the curves from each other for easier viewing. Similarly, the spin anti-parallel current is artificially shifted to the left by 0.5 ns to separate it from the spin parallel current.

Chapter 4

Electron transport on topological insulator surface with non-uniform magnetic exchange potentials

4.1 Introduction

While we have focused on the electric control of magnetization using TI in the previous chapters, the magnetization influence on electron transport in TI is still left insufficiently exploited. One progress was made by Dr. Kong that an unusual magnetoresistance was discovered with a single ferromagnetic barrier on TI surface. [27] This was then extended to the proposal of electron wave guiding devices using magnetically patterned channels by Dr. Li. [72] Although this proposal has been inspired by the electron wave guiding phenomena in graphene with electric potential barrier, the mechanism for the magnetic potential induced guiding phenomena on TI surface is fundamentally different. [19, 73]

The optical analogy of electrons origins from the mathematical similarities between the 2-spinor Dirac equations for graphene or TI surface electrons and the Maxwell's equations for electromagnetic wave. If the Dirac cone is shifted along energy by applied electric potential, the same wavevector $\mathbf{k}$ would result in difference real space motions across the boundary, which is equivalent to the refraction of light at the interface of materials with different refraction index. Electronic Veselago lens and electron wave guiding devices that resembles optical fiber have already been proposed and actively investigated based on graphene. [19, 21, 73, 74]

In the case of TI, while there are hardly anything more to discuss for the electrostatic potential induces quasi-optic effect apart from exactly the same behavior as in graphene, the unique property of spin-momentum interlock of TI surface electrons remains unused, which is expected to induce unique features. Unlike graphene, the two spinors of TI surface states

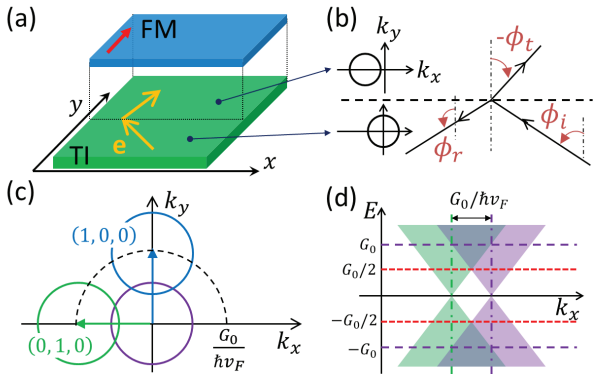

Figure 4.1: (a) Schematic illustration of the TI-magnet heterostructure inducing an effective junction in quasi-optical electron transport. The magnetization of the dielectric ferromagnet (FM) is assumed to be along the $+y$ direction, unless stated otherwise, as an example. (b) Definition of the characteristic angles used in the analysis. The angles are measured in the counterclockwise rotation with respect to the $+y$ axis. (c) Electronic band modification of the TI surface states in the k space due to the exchange interaction with a magnet. The iso-energy contour initially centered at $k = 0$ (purple) becomes displaced on the k_x-k_y plane in the presence of an in-plane magnetization (green and blue). The dashed circle traces the center of the displaced Dirac cone as the magnetization orientation rotates on the plane. (d) Alignment of TI surface electronic bands projected on the k_x axis in the capped (green) and uncapped (purple) regions [see parts (a) and (c) as well].

correspond to real electron spin instead of pseudospin (valley dependence). [21, 22] As a result, the influence of magnetic potential on electron spin can be passed on to the band structure with spin being the medium. Using finite difference time domain (FDTD) and non-equilibrium Green's function (NEGF) simulation, Dr. Li has verified the efficiency of the guiding effect and proposed the applications of switching and beam steering devices. [72]

In this chapter, this exploration is continued. Section. 4.2 illustrates the full physical model for the electron transmission/reflection phenomena across a magnetic/exchange barrier, giving a more detailed and comprehensive understanding of this phenomenon. An angle dependent transmission behavior is identified and verified by FDTD simulations, as well as the generation of anomalous Hall current. The application and performance evaluation of CMOS like switching devices are discussed afterward in Section. 4.3.

4.2 Electron wave transmission across a exchange potential boundary

4.2.1 The physics model of the electron transmission/reflection problem

Figure 4.1(a) shows the specific structure under investigation. It consists of a TI layer and an insulating magnet that covers a part of the TI surface. The electrons are assumed to be injected from one side of the surface (for instance, the uncapped region) toward the opposite (i.e., the magnet capped region) as illustrated. An effective junction is formed at the boundary due to the magnetically induced mismatch in the band structure that is schematically represented by the two shifted iso-energy contours (i.e., circles) of Figure 4.1(b). This relation is evident from the eigenvalues of the Hamiltonian for the TI surface in the presence of exchange interaction with the magnet: $H = \hbar v_F \mathbf{k} \times \sigma_s - G_0 \mathbf{m} \cdot \sigma_s + U$, where v_F is the Fermi velocity ($= 4.3 \times 10^7$ cm/s for a typical TI, Bi_2Se_3), $\mathbf{k}$ the electron momentum, σ_s the Pauli matrix for electron spin, $\mathbf{m} = (m_x, m_y, m_z)$ the normalized magnetization vector of the magnet, and U the electrostatic potential. In addition, G_0 denotes the exchange constant that is determined by the strength of the magnet as well as the effectiveness of the TI-magnet coupling. The resulting eigenenergy is

$$E = U \pm \sqrt{G_0^2 m_z^2 + (\hbar v_F k_x + G_0 m_y)^2 + (\hbar v_F k_y - G_0 m_x)^2}. \tag{4.1}$$

Thus the influence of the exchange interaction on the TI surface electrons is clear. The out-of-plane magnetization (i.e., m_z) opens a band gap at the Dirac point, while the in-plane magnetization shifts the Dirac cone by $\frac{G_0}{\hbar v_F}$ from the zone center in the two-dimensional momentum space with a 90° phase lead in the counterclockwise rotation [e.g., $\mathbf{k} = 0 \rightarrow \mathbf{k} = \frac{G_0}{\hbar v_F}\hat{\mathbf{y}}$ for $\mathbf{m} \parallel \hat{\mathbf{x}}$; see Figure 4.1(c)]. The non-zero band gap induced by the out-of-plane magnetization can play the role of an energy barrier at the boundary between the capped and uncapped regions much the same as the conventional semiconductor heterostructures. [75] Here, our analysis focuses on the junctions with in-plane magnetization.

A closer examination further reveals that the magnetization component parallel to the interface does not affect electron transport across the junction at all due to the invariance in the transverse direction. This can be seen clearly from Figure 4.1(c) by comparing two circular iso-energy contours, one at the zone center (purple) and the other shifted along the $+y$ axis (blue). An incident electron on one of the circles can always find the corresponding state on the other, while maintaining the same energy and the transverse (i.e., x) wavevector, and thus crosses the boundary without experiencing any change. On the other hand, the normal component m_y directly modifies the quasi-optical transport at the junction and, hence, must be considered explicitly. Hereafter, we assume that the magnetization of the magnet covering the upper half is along the $+y$ direction (i.e., $m_y = 1$) as depicted in Figure 4.1(a). In addition,

the electric potential U is taken zero for simplicity.

Figure 4.1(d) illustrates the corresponding alignment of TI surface electronic bands projected on the k_x axis in the capped (green) and uncapped (purple) regions. Since the transversal wavevector (k_x) must be preserved when transmitted through the junction, three distinctive scenarios can be identified in term of the electron energy for a given exchange coupling constant G_0; i.e., $[0, \frac{G_0}{2}]$, $[\frac{G_0}{2}, G_0]$, and $[G_0, E_c]$, where E_c denote the bottom of the TI bulk conduction band. Here, we examine the conduction band ($E > 0$) explicitly; the valence band shows essentially the same behavior. When the electron energy is below $\frac{1}{2}G_0$, there is no overlap between the bands in the two regions, so no transmission can occur. This is the range where the proposed electron waveguiding devices work with 100% guiding efficiency. [72] Non-zero transmission starts to occur when the electron energy exceeds $\frac{1}{2}G_0$. So long as the energy is still below G_0, however, the overlap exists only in the k space between two Dirac points ($-\frac{G_0}{\hbar v_F} < k_x < 0$) as shown. Accordingly, the electron velocity along the x axis reverses the direction across the boundary as in a Veselago lens; the left half of one circle ($v_x < 0$) overlaps with the right half of the other ($v_x > 0$). Yet the focusing effect is missing because the magnitude is not necessarily conserved. In addition, it constitutes just one half of the lens due to the asymmetric overlap. Only the electrons approaching the junction from the right (i.e., $v_x < 0$) can proceed to the capped region; those impinging on the interface from the left ($v_x > 0$) cannot find a proper final state and are totally reflected. Note also that the condition is opposite when the carriers are injected toward the uncapped region. If the electron energy surpasses G_0, the directional dependence reduces to the angular dependence. Electrons approaching from both directions may be transmitted although there is still a critical angle beyond which the flux becomes zero.

A detailed theoretical calculations further elucidate this phenomenon. It can be solved analytically as a standard reflection/transmission problem by matching the wavefunctions at the interface. A similar technique has been applied successfully in graphene with an electric potential step. [17, 76] The resulting transmitted and reflected amplitudes are given by:

$$t = \frac{e^{i\phi_i} + e^{-i\phi_i}}{e^{i\phi_i} + e^{-i\phi_t}}, \quad r = \frac{e^{-i\phi_i} - e^{-i\phi_t}}{e^{i\phi_i} + e^{-i\phi_t}} \tag{4.2}$$

where $\phi_{i,t}$ denote the incident and transmitted angles as specified in Figure 4.1(b), respectively. Note that the angles are defined as counterclockwise rotations with respect to $+y$ axis. Then the transmission probability can be written as $T = |t|^2 \cos(\phi_t)/\cos(\phi_i)$. In the present setup [see Figure 4.1(a,b)], conservation of the energy and the parallel wavevector dictates $\phi_r = \pi - \phi_i$ as well as

$$\sin(\phi_t) = \sin(\phi_i) - \frac{G_0}{\hbar v_F |\mathbf{k}|}. \tag{4.3}$$

When the right side of the above equation falls outside the range [−1,1], the resulting ϕ_t becomes

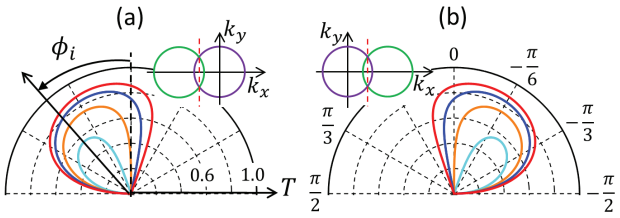

Figure 4.2: Polar plots of the transmission probability versus the incident angle. The magnetization of the capped region [i.e., the upper half in Figure 4.1(a)] is set to be along the (a) $+y$ and (b) $-y$ axes, respectively. From the outside to the inside, the plotted probability contours correspond to the electron injection energy (E/G_0) of 1.5, 1.25, 1.0 and 0.75, respectively.

complex, leading to the evanescent states. It resembles transmission of the light from a high-index to a low-index material. Concerning the magnitude of G_0, a number of relevant studies suggest that the exchange interaction energy of tens to hundreds of meV can be reasonably anticipated at the well prepared TI-magnet interfaces. [24, 72, 34, 77, 32]

Figure 4.2(a) plots the obtained transmission probability as a function of incident angle for a number of injection energies. A couple of features are apparent. Firstly, the transmission is asymmetric around $k_x = 0$ as predicted in the qualitative analysis (i.e., the dependence on the electron incident direction). Secondly, a critical angle ϕ_c ($= \sin^{-1} \frac{G_0 - E}{E}$) can be defined for each injection, identifying non-zero transmission between the range $[\phi_c, \frac{\pi}{2}]$. This criterion clearly illustrates that the case of $E < \frac{1}{2}G_0$ allows no transmission, while the range extends to the negative angle (i.e., the incidence from the left) once $E > G_0$ as discussed earlier. When the magnetization at the junction switches to the $-y$ direction, the characteristic features are maintained except the π phase difference [see Figure 4.2(b)]. In addition, it may be worth noting that the similarly asymmetric behavior can be expected even with a non-zero external electric potential ($U \neq 0$) although the picture can become complicated by the alterations in the quantitative values of the specific energy and critical angle.

The analytical results are further verified with the FDTD method. For clear visualization of the anticipated transmission phenomena, a Gaussian wavepacket is used to trace the path of the electron injected with a specified incident angle and energy toward the boundary. [78] In the numerical implementation, the staggered grid leap-frog scheme is adopted to avoid the issue of fermion doubling. [79] Figure 4.3 illustrates the behaviors at three typical energies with both the rightward- ($v_x > 0$) and leftward-traveling ($v_x < 0$) electrons. One notable result, other than those already discussed and anticipated, concerns Figure 4.3(e). Although the injection energy is higher than the effective barrier height ($E = \frac{3}{2}G_0$), no transmission is observed since the incident angle ($-\pi/4$) is wider than that of total internal reflection ($-\pi/6$). When the electrons approach from the opposite direction [Figure 4.3(f)], however, most of them transmit

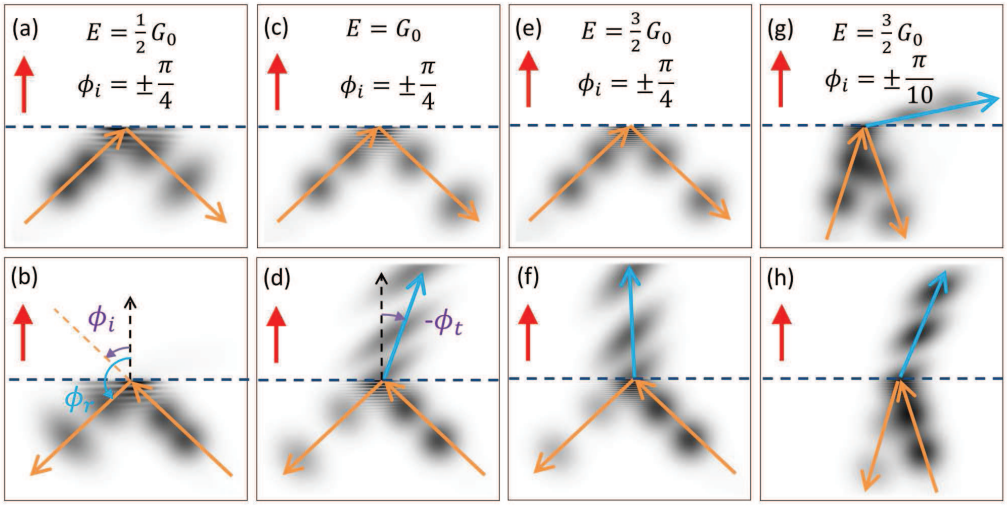

Figure 4.3: FDTD simulations of a Gaussian wavepacket incident to the magnetically induced junction from (a,c,e,g) the left and (b,d,f,h) the right with various electron energies and angles. The block arrow (red) denotes the orientation of the magnetization.

past the junction with relatively small reflection. Once the incident angle becomes narrower, the transmission is possible for those injected from either directions as shown in Figure 4.3(g) and (h). It is also worth noting that the strength of the outgoing wave remains less pronounced for the electrons with $v_x > 0$ (see the darkness of the images).

4.2.2 Generation of anomalous Hall current near the boundary

An interesting consequence of this directional transmission is the generation of an anomalous Hall current. Consider a case when an external bias is applied across the boundary in such a way to induce electron injection from one side of the structure (e.g., the uncapped region). The ensemble of electrons approaches the interface with the net momentum/flow only along the y direction (i.e., $I_x^i = 0$) although each electron can have oblique incidence individually (for instance, due to the scattering during the flight); in other words, with a balanced distribution in the $+k_x$ and $-k_x$ space. However, preferred transmission of the leftward moving electrons discussed above (for electrons with $E > \frac{1}{2}G_0$) leads to the transmitted flux with a net non-zero component in the x direction ($I_x^t \neq 0$). This also means an equal amount of the x current in the reflected electrons ($I_x^r = I_x^t$) since the conservation rule must be satisfied at the junction; i.e., $\mathbf{I}^i + \mathbf{I}^r = \mathbf{I}^t$. Hence, the applied bias or y-field induces an electron flow along the transverse x-axis.

The magnitude of the anomalous Hall current depends on the energy of the injected electrons. Assuming that the incident angles at a given energy are evenly distributed between $-\pi/2$ and $\pi/2$, the subsequent calculation plotted in Figure 4.4(a) illustrates the gradual increase with the electron energy ($> \frac{1}{2}G_0$), followed by a slow decrease with the peak around $\frac{3}{2}G_0$. The Hall angle defined as the ratio of the transverse and longitudinal currents, $\tan^{-1}[(I_x^t + I_x^r)/I_y^t]$, can further characterize the phenomenon. As shown in Figure 4.4(c), the angle asymptotically approaches to zero at high energies, while it exhibits a singular behavior near $E = \frac{1}{2}G_0$. In order to emulate the realistic conditions, however, the calculation must also account for the effect of thermal broadening. For this, we consider a thermal distribution of electrons at room temperature and integrate the relevant expressions over the available energy levels; i.e.,

$$I_{mn}^{th}(\mu) = \int I_n^m(E) M(E) \frac{\partial f(E,\mu)}{\partial E} dE \,. \tag{4.4}$$

Here, indices m and n range (i, r, t) and (x, y), respectively, superscript th symbolizes the consideration of a thermal distribution, $f(E, \mu)$ denotes the Fermi-Dirac statistics with the chemical potential μ, and $M(E) \propto |E|$ represents the density of states/modes. To actually evaluate (4.4), a numerical value must be assigned to the exchange energy since the thermal energy is given by a specific number (i.e., 300 K). Hence, we set $G_0 = 0.1$ eV for convenience. [72]

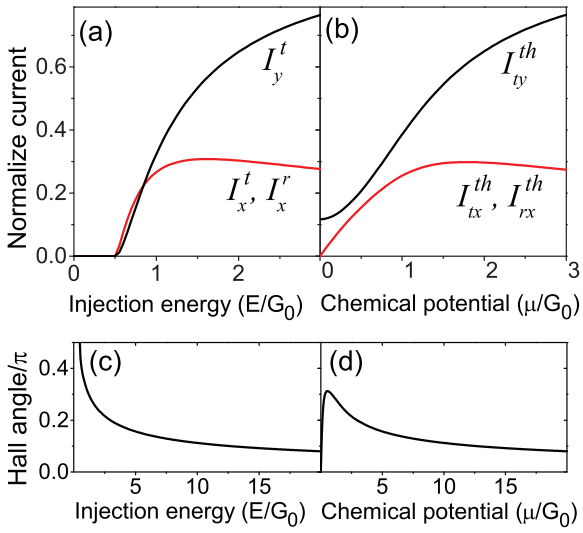

Figure 4.4: (a) Injection energy dependence of the anomalous Hall behavior. The currents are normalized to the incident current, i.e., $I^{t,r}_{x,y} \rightarrow I^{t,r}_{x,y}/I_i$. I^t_x and I^r_x overlaps as the transverse component of the flux must be conserved across the junction interface. (b) Anomalous Hall behavior as a function of the electrochemical potential when the thermal broadening of the electron distribution is accounted for at 300 K. G_0 in this case is assumed to be 0.1 eV. (c) and (d) depict the Hall angles corresponding to (a) and (b), respectively.

The corresponding outcome is given in Figure 4.4(b,d). One main difference with Figure 4.4(a,c) is that the Hall angle now sports a peak of approximately 0.3π at $\mu = \frac{1}{2}G_0$ rather than a monotonous behavior; the transmission (hence, the Hall current) is non-zero below $\frac{1}{2}G_0$. It is also worth noting that the result at a high chemical potential ($\mu \gg k_BT$) converges to the mono-energetic curves in Figure 4.4(a,c), consistent with the characteristics of a heavily degenerate system (i.e., dominated by the carriers near energy μ). The influence of bulk bands is beyond the present analysis.

The anomalous Hall phenomenon offers an experimentally verifiable effect in studying the quasi-optic behaviors of TI surface electrons. A standard Hall bar measurement can serve for this purpose. Strictly speaking, the distribution of the injected electrons at the junction depends on the applied bias and the scattering characteristics of the TI surface states; hence, it may deviate from the simple equilibrium statistics assumed earlier. Nonetheless, such details are to bring about only the quantitative differences. One potentially important point for the experimental setup is that the probe electrodes must be located at or in close vicinity to the junction boundary. Since the predicted effect is an interfacial phenomenon, it is expected to decay exponentially from the boundary over a length scale determined by the electron mean

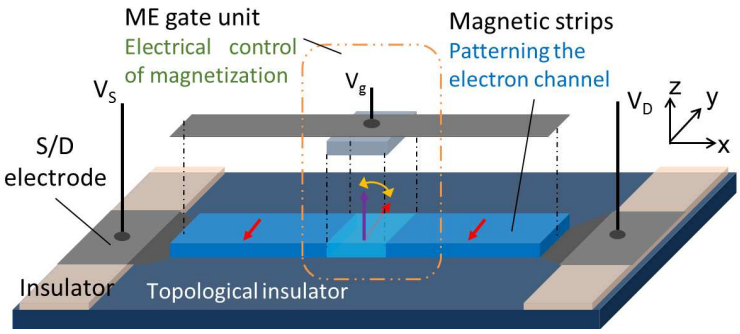

Figure 4.5: The structure of the TI based magnetoelectric transistor. The gate spans over the whole channel for uniform carrier concentration in the channel.

free path, which is around several nanometers in the currently available TI samples and may be as long as the micrometer level once the impurities can be minimized. [80, 81, 82, 83] By contrast, the size of the probes themselves does not need to be particularly small. In addition, the demagnetization field near the magnet boundary may potentially induce other complexities via the topological magnetoelectric effect that resembles axion electrodynamics. [84, 85] Yet the normally small demagnetization field indicates the relatively minor influence when compared to that of the exchange interaction.[1] Hence, this effect can be safely neglected in the analysis.

4.3 Proposal of a topological insulator based magnetoelectric transistor

Based on the electron guiding phenomena and the efficient blocking behavior of out-of-plane magnetization, a new type of transistor is proposed based on wave-guiding phenomena of topological insulator (TI) surface electrons for applications in CMOS-like circuits and switchable interactions in spin logic circuits. [72, 75] As shown in Figure 4.5, the carrier channel is patterned by the magnetic strip and the ON/OFF switch is achieved by the electrically controlled magnetic valve. In this section, the current-gate voltage (Id-Vg) relation and the time resolved performance are characterized. Very low subthreshold swing (below 10 mV/dec) and operating frequency above 1 GHz are expected.

In the device structure shown in Figure 4.5, the essential components are the insulating magnetic strips and the magnetic barrier in the middle. Based on the behaviors discussed in

[1] In a rough analysis, the demagnetization field is bounded by $4\pi M_s$ with M_s denoting the saturation magnetization. Assuming a typical value ($M_s = 140$ emu/cm^3), the resulting energy variation due to the topological magnetoelectric effect is estimated to be around 0.14 meV by following the approach of Ref. [85]. Clearly, this is much smaller than the exchange constant G_0 used in the present study.

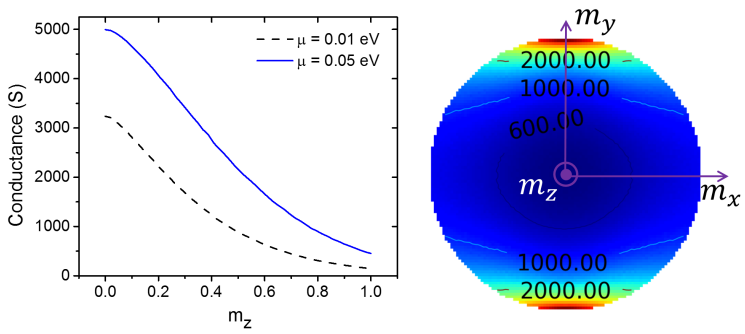

Figure 4.6: The conductance variation according to the out-of-plane magnetization of the barrier. The color plot maps the conductance to the in-plane magnetization configuration.

the previous section and Dr. Li's pioneering paper, the electron propagation path is patterned by the magnetic strip with magnetization perpendicular to the channel direction and the channel ON/OFF state is determined by the magnetic valve. [72] When the valve is magnetized along y, the injected electrons from the source propagate freely to the drain, composing the ON state; when the valve is magnetized out-of-plane, a band gap is opened beneath the valve which acts as a barrier that blocks the electron propagation, composing the OFF state.

This ON/OFF phenomenon is essentially the TI surface magnetoresistance first investigated by Dr. Kong, where the only difference is that the guiding channel was not included in the structure at that stage. [27] In fact, in a 1-dimensional treated, assuming the device is invariant along $\hat{y}$ direction, the guiding magnetic strips does not introduce any noticeable influence. While the previous has evidenced the ON/OFF behaviors at specific magnetization states, the calculation is extended to model the channel conductance at arbitrary magnetic and electrostatic conditions (Appendix. C) in order to evaluate the dynamic response of this system. This magentoresistance is recalculated for the current situation as shown in Figure 4.6. The channel conductance reaches the minimum for $\mathbf{m} \parallel \hat{z}$ and maximum for $\mathbf{m} \parallel \hat{y}$. This behavior agrees with our previous analysis that out-of-plane magnetization opens a bandgap of $2G$ while the effective transport bandgap induced by in-plane magnetization barrier is G. The magnetization perpendicular to the current direction (i.e. along the valve boundary) does not induce any barrier.

Consequently, switching the channel can be accomplished as soon as a controlled magnetization rotation from $\mathbf{m} \parallel \hat{y}$ to $\mathbf{m} \parallel \hat{z}$ is realized. We note that the electrically controlled 90 magnetic switch can be induced by adjusting the TI Fermi level with a gate as discussed in Chapter. 3 (the intrinsic approach). Better performance could be expected if an specific magnetoelectric stack is used, taking advantage of the great development that has been made

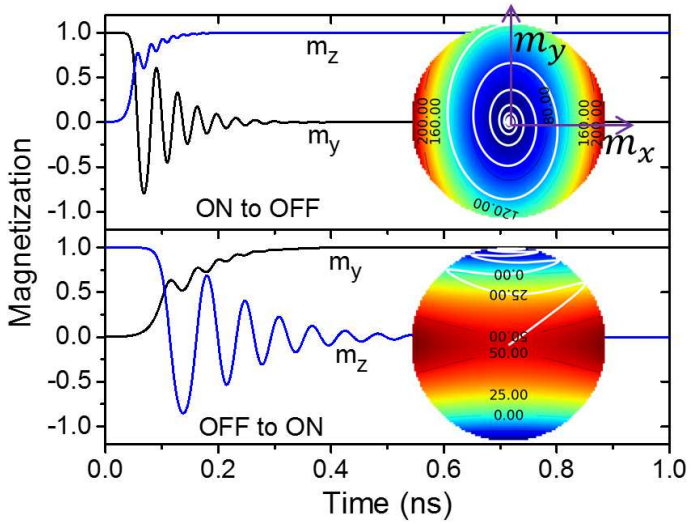

Figure 4.7: The typical magnetic switching dynamics. The color maps show the energy profile that drives the magnetic rotation and the white lines indicate the corresponding path in magnetic space.

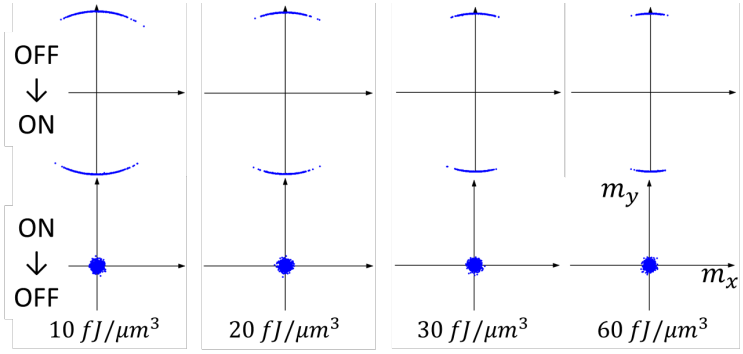

Figure 4.8: The distribution of final state over 1000 simulations, detected 1 ns after the switching begins. The hard axis anisotropy along x is assumed to be 10, 20, 30 and 60 fJ/m3.

on multiferroic materials (the multiferroic approach) [57, 86, 87, 88, 15, 86]. According to the review in Ref. [15], the magnetoelectric coupling coefficient could potentially reach 1 Oe $\cdot$ cm/V and that around 0.1 Oe $\cdot$ cm/V at room temperature has been realized experimentally. This indicate that the required voltage variation could be as low as 1 mV. Given that magnetic switches often exhibit good threshold behaviors, steep switching slopes can be expected. The following two sections will present the results for both approaches.

4.3.1 The intrinsic approach: switching with intrinsic TI-FM coupling

According to the discussion in Chapter. 3, out-of-plane magnetization is preferred when the Fermi level aligns with the Dirac point, while the demagnetization field leads to in-plane magnetization when the Fermi level is in the valence or conduction band. The insulating magnet could also play the rule of the gate dielectric to simplify the structure, while the switching performance is limited by the coupling efficiency at the TI-magnet interface. The typical magnetization switching behaviors are shown in Figure 4.7. Performance wise, The choice of operating frequency has to ensure that the magnetization sufficiently relaxes to the target state, which is normally at sub-nanosecond level. Using the stochastic Landau-Lifshitz-Gilbert equation, the final states are mapped to the $m_x - m_y$ plane with 1 ns pulse width in Figure 4.8, verifying the tight distributions for reliable operations. The dynamics can be further improved with larger hard axis anisotropy along x that confines the magnetization rotation path in y-z plane, of which a detailed discussion can be found in Chapter. 3. By coupling the LLG equation and transport calculations, typical 0.5 GHz switching operations are simulated as shown in Figure 4.9. It should be noted that the proposed devices here are intended to operate at low current, so that the torque from the TI surface is ignored.

For FET-like operations, the relation between magnetization and TI Fermi level also ensures that the ON state corresponds to higher carrier density, which helps to increase the ON current and limit the OFF current. The performance is studied by coupled magnetic-transport simulations. Figure 4.10 shows the Id-Vg curve at room temperature. The left and right halves resemble that of a PMOS and NMOS respectively. At ON state, the current is determined by the carrier concentration, while at OFF state, the magnetic barrier sufficiently blocks the current. With an assumed gate capacitance of 0.05 F/m2, the subthreshold swing reaches as low as 14.5 mV/dec at the P-side and 38.4 mV/dec at the N-side. This value is roughly inversely proportional to gate capacitance and larger capacitance can further steepen the slopes, indicating that below 10 mV/dec is achievable. Plus, the low threshold voltage (0.1$\sim$0.2 V) also ensures low energy consumption. It is also worth noting that the gate magnetic controllability can be decoupled from TI using other magnetoelectric units like multiferroic materials. [88] Even lower threshold voltage ($\sim$1 mV) can be expected at the cost of additional material integration.

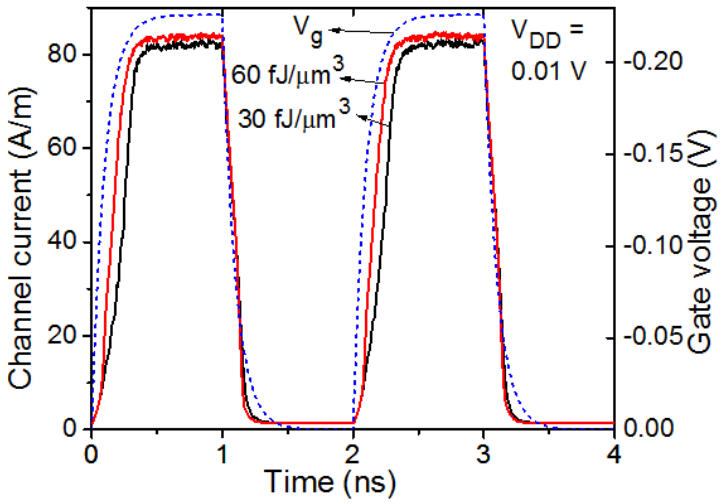

Figure 4.9: Time resolved switching events of typical transistor ON/OFF operations. The data is averaged over 100 stochastic simulations.

Based on the transistor type behaviors, an inverter is designed in a complementary manner similar to CMOS circuits (Figure 4.11). It is composed of a normally ON cell operating at the P-side and a normally OFF cell operating at the N-side. The normally ON/OFF is determined by the intrinsic chemical potential of TI, which can be induced by doping or back-gating. Several inverting operations are simulated as shown in Figure 4.11. The output voltage correctly reverses the input and the delay is well below 1 ns. It is remarkable that the output settles quicker than the magnetization, indicating the possibility of a higher working frequency than that determined by the magnetization relaxation. The resulting channel current also shows spikes during the transition period like the CMOS inverters.

4.3.2 The multiferroic approach: switching with multiferroic structures

The second approach introduces a specific magnetoelectric stack, so it could be optimized separately for the voltage controlled magnetic switch. Here the interface between magnet and TI is only used to control the current through magnetic barrier. Without loss of any generosity, the magnetoelectric effect follows Eq. 4.5.

$$K_{me}(V_g) = \frac{1}{2}\mu_0 \lambda \mathcal{E}(V_g) M_0 \tag{4.5}$$

where λ is the magnetoelectric coupling coefficient that varies around $0.01 \sim 1$ Oe $\cdot$ cm/V and M_0 is the saturation magnetization.[15] $\mathcal{E}(V_g)$ is the electric field as a response of the applied

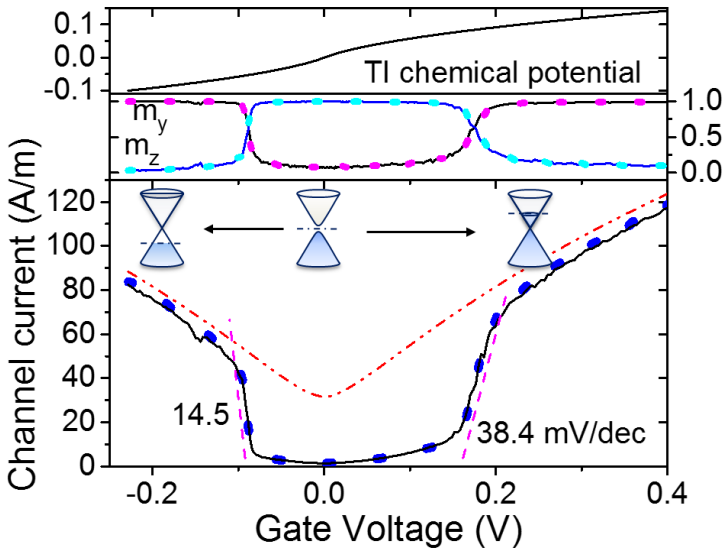

Figure 4.10: The current-gate voltage characteristics (bottom), the corresponding magnetization rotation (middle) and the TI chemical potential variation (top). The solid line and dots represent hard axis anisotropy along x to be 30 and 60 fJ/m3 respectively. The red dash-dot line indicates the current variation induced solely by the gate voltage. Subthreshold swings are marked beside the slopes.

gate bias. It should be noted that as nonmagnetic layers may be necessary for multiferroic response, the total gate dielectric thick is larger than the magnetic layer and $t = 4$ nm is used in our simulations. This anisotropy terms takes the role of the surface induced anisotropy and add to the K_z term to modulate the magnetization according to the LLG equation as shown in Eq. 2.1. Thus similar magnetization dynamics behavior can be observed as that shown in Fig. 4.7 and 4.8, which are not repeated here.

The time resolved channel current response is shown in Figure 4.12(a) with the magnetoelectric coupling coefficient $\lambda = 0.05$ and 1 Oe $\cdot$ cm/V for red and black lines respectively. The gate voltage variation range is set to $0 \sim 0.2$ V. Similar behaviors to the intrinsic approach is observed. The response delay is around 0.1 ns, which indicate GHz level operating frequency. Compared to the intrinsic approach, for witch the performance is determined by the exchange property at the interface with hardly any engineering freedom, the multiferroic approach could potential adjust the device working point through the coupling coefficient λ by material/structure engineering. It should be emphasized that the range of input gate voltage has to match the magnetoelectric coupling coefficient. Too small variation may cause unreliable switches and too large variation would cause unnecessary delay at the ON to OFF switching period, apart from the high energy consumption. A such example is shown in Figure 4.12(b)

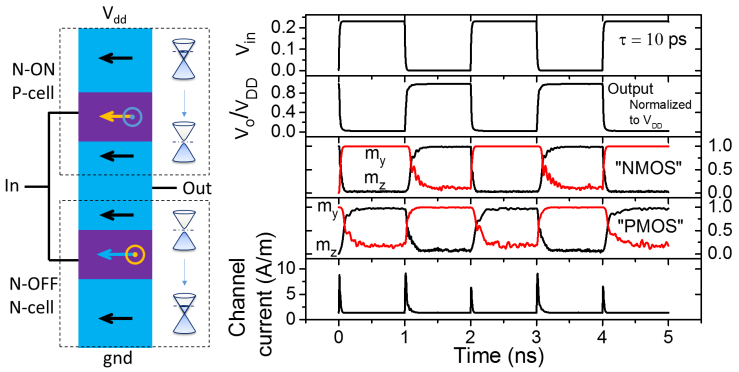

Figure 4.11: Design of a CMOS-like inverted and the simulated inverter performance. All the curves are averaged over 100 stochastic simulations and voltage supply is set to VDD = 0.01 V.

with $\beta = 1$ Oe $\cdot$ cm/V and voltage variation within 0$\sim$0.2 V. The large magnetoelectric coupling coefficient indicates that a small gate bias would be sufficient to set the magnetization in-plane, so the magnetization only returns to vertical direction at the end of the gate voltage tail when it is sufficiently low. This is indeed related to the threshold voltage of the switching process. It can be roughly estimated as the voltage that cancels the out-of-plane anisotropy. In the current setup, it is $V_{\mathrm{T}} \approx 4M_0 t/\lambda$ (where the quantum capacitance effect is approximated by a factor of 2).

A significant improvement of the multiferroic approach over the intrinsic one can be seen from the current-voltage curves, as shown in Figure 4.13. The black and blue lines depict the performance with coupling coefficient $\lambda = 0.05$ and 0.1 Oe $\cdot$ cm/V respectively. They correspond to low equivalent sub-threshold swing at 7.9 and 5.7 mV/dec. Even lower values at 0.7 mV/dec can be achieved by setting $\lambda = 1$ Oe $\cdot$ cm/V. As magnetoelectric coupling coefficient up to 0.1 Oe $\cdot$ cm/V is readily available in several heterostructures [15], threshold swing at several mV/dec is well expected in this proposed device. Nevertheless, larger magnetoelectric coupling coefficient also significantly reduce the threshold voltage while improving the threshold behavior, which potentially affect the ON state conductance. The plot in the right panel of Fig. 3(b) uses an intrinsic chemical potential of 0.05 eV to match the channel current level with the left panel in the cost of a higher OFF state current. Although assuming a larger out-of-plane easy axis anisotropy could help resolve this issue, careful tuning is necessary in the device design to meet a specific performance target.

The same design of 1-bit inverter also applies to the multiferroic approach. For the normally on p-cell, acceptor doping can be used to meet the requirement on adequate conducting states

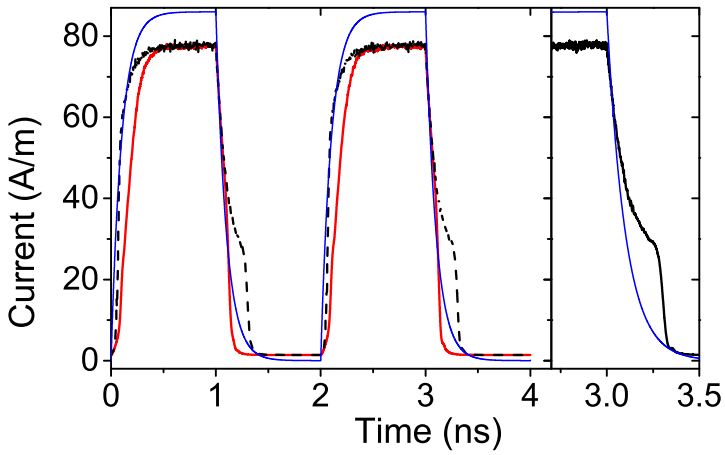

Figure 4.12: Time resolved switching events of typical transistor ON/OFF operations. The data is averaged over 100 stochastic simulations. The red solid and black dashed lines represent that for λ set to 0.05 and 1 Oe $\cdot$ cm/V respectively. The blue line indicate the driving pulse. The falling edge is enlarged on the right for $\lambda = 1$ Oe $\cdot$ cm/V case.

at low input voltage, and a negative magnetoelectric coupling coefficient could cause the magnetization to switch from in-plane to out-of-plane in positive gate bias. Plus, the out-of-plane anisotropy K_z has to be zero to ensure that the intrinsic easy axis is along $\hat{y}$. Both the sign of magnetoelectric coupling and the magnetic anisotropy profile could potentially be achieved by engineering the multiferroic heterostructure, the fabrication of which is indeed a big challenge. Figure 4.14 shows the results for several operation using the multiferroic approach when the input signal varies every 1 ns with a time constant of 10 ps (the top panel). With magnetoelectric coupling coefficient set to ± 0.1 Oe $\cdot$ cm/V and TI chemical potential set to -0.057 eV, the output correctly follows the input according to the inversion logic (the second panel). Following two panels depict the corresponding magnetization dynamics in these operations. Similar to conventional CMOS circuit, channel current has peaks during the switching process while the steady state current is kept at a low level (bottom panel).

4.4 Summary

This chapter demonstrated the detailed physical model that governs the electron transmission across a magnetic boundary. Depending on the magnetization profile and electron energy, the electrons can be either totally blocked or transmit with a well defined angle dependence. An anomalous Hall current is induced by the transmitted portion. While this quasi-optic phenomena could have various novel application, an intuitive design of a switching type device is proposed.

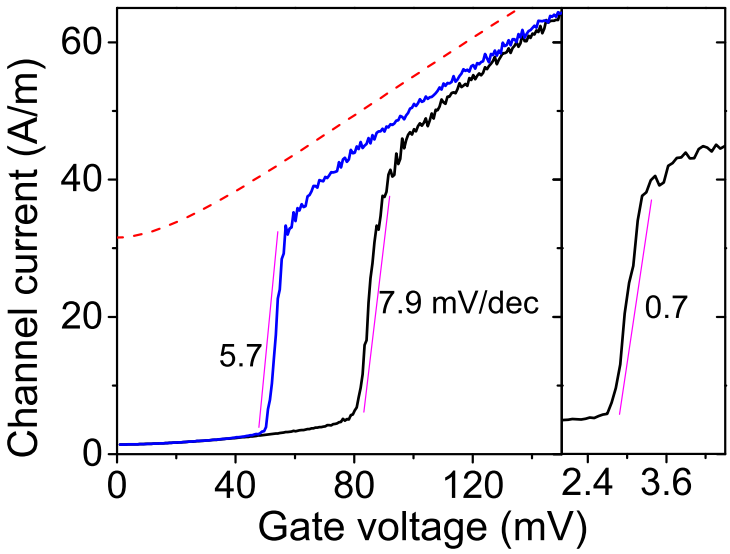

Figure 4.13: The current-voltage characteristics of the proposed devices. The numbers near the slopes mark the equivalent subthreshold swing and the red dashed lines show the current variation induced only by gate voltage without the magnetic barrier. The main panel include that with $\lambda = 0.05$ Oe $\cdot$ cm/V (black) and $\lambda = 0.1$ Oe $\cdot$ cm/V (red). The right panel shows the switching slope for $\lambda = 1$ Oe $\cdot$ cm/V.

It combines the guiding effect of magnetically patterned channels and the blocking effect of the middle magnetic valve. By coupling the magnetic and transport simulations, the performance of this device is investigated in detail. The CMOS-like operations are identified and an inverter is developed in the complementary manner.

Compared to CMOS, one possible limitation of the proposed transistor is the ON/OFF ratio, which is affected by the thermal broadening of the electron spectrum. It causes the non-zero idle current for the inverter. One potential solution is to use tunneling barrier to narrow the spectrum. Due to the large energy relaxation length (~ 1 μm), the spectrum can be conserved over the device dimension. One the other hand, a clocked supply voltage has become a typical operating scheme for spin logic circuits that also surfer from low ON/OFF ratios. This can also be adopted for the transistor proposed here.

A key advantage of this proposed switching device is the steep switching slope, while the ON-OFF ratio is limited to two orders of magnitude. Thus it would be potentially good candidate for ultra low power analog circuits to pick up ultra small signals and serve as the first stage amplification. Yet for analog applications, a well defined relation between current and voltage is essential. This is hardly a problem for conventional transistors based on electron charge. The involvement of a large number of electrons naturally averages out large fluctuations and

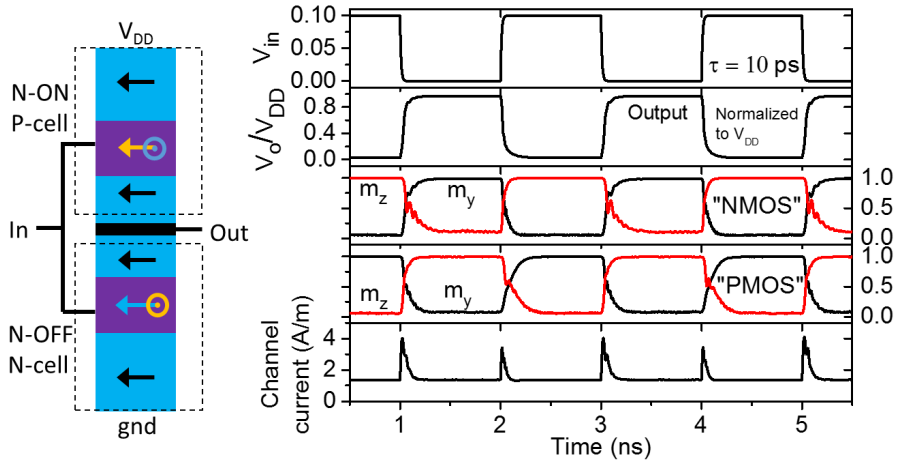

Figure 4.14: Schematic layout of a complementary inverter and its simulated inverting operations. It composes of a normally on P cell and a normally off N cell. The guiding channels are indicated with the cyan blocks and the switching magnets are in purple. Low input voltage has valve magnetization marked in orange and high input voltage has it in cyan. The input voltage switches between 0 and 0.1 V every 1 ns with a time constant 10 ps. The output curves and the magnetization variation are the response of an inverter based on the multiferroic approach with $|\lambda| = 0.1$ Oe $\cdot$ cm/V. The channel driving voltage is chosen as $V_{DD} = 0.01V$.

results in a well defined current-voltage relation. However, the "transistor" proposed in this paper relies on the rotation of a mono-domain nanomagnet, which is susceptible to thermal fluctuations. The smooth switching curves in the resulting figures are the result of averaging over 100 simulations. They represent the average performance, but do not ensure each operation would follow exactly. A feasible solution is to connect a number of identical devices in parallel to mimic the averaging process. Using the previously mentioned device setup, which has a width of 60 nm, if 100 devices are connected, it would result in a total width around 10 μm. This dimension is fully acceptable for analog applications.

Chapter 5

nonlinear magnetic dynamics in nanomagnet–topological insulator heterostructures

5.1 Introduction

Along with the development of information technology, magnetic devices have been an essential component. Information can be easily coded into and decoded from the stable magnetization states of nanomagnets. Much research effort has been devoted to improving the magnetization switching efficiency and reliability [89, 86, 57, 90, 91]. On the other hand, given the possibility to use spin wave for logic operations, steady state magnetic oscillation also picks up attention as the spin wave generators [92, 93, 94, 95, 96, 97, 98]. By coupling multiple magnetic oscillators, it could also realize on-chip communications [99].

In terms of magnetic materials, metallic magnetic compounds have been the intuitive choice for magnetic devices like magnetic random access memories based on magnetic tunneling junctions (MTJ). Instead of external magnetic field or microwave, spin transfer torque (STT) from flowing electrons could manipulate the magnetization and generate oscillations [89, 57, 90]. Electric field has also been shown able to assist this process by modulating the anisotropy profiles [86]. On the other hand, magnetic insulators are the desired materials for spin wave devices because of the low damping factor, and some of them have intrinsic multiferroic properties that could enable electrical control of magnetic tilts or switches [100, 101, 15]. However, STT does not exist due to the lack of free electrons, so that most experiments rely on rotating magnetic field or the Ampere field of a microwave current to generate oscillations with a much lower efficiency than electrical control [101]. Nevertheless it has been shown that by coupling the magnetic insulator to an adjacent topological insulator, the magnetization can be

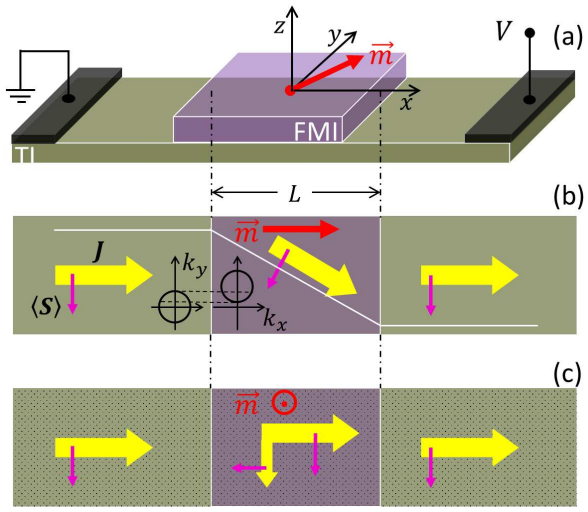

Figure 5.1: (a) the schematic of the heterostructure that generates the multiple dynamics behaviors. An insulating nanomagnet is attached to the TI surface and two electrodes are used to inject current through the TI surface. (b) and (c) shows the mechanisms for the transverse current (i.e. the anomalous Hall current) due to in-plane and out-of-plane magnetization respectively. The yellow arrows represents the electron flow and the purple arrows show the corresponding spin polarization. The inserted plots in (b) shows the alignment of the iso-energy circle in momentum space due to the in-plane magnetization.

manipulated through modulating the electronic state in the TI layer, which is enabled by the spin momentum interlock of TI surface electrons [1, 102, 28]. When a net current is applied to the TI surface, spin polarization perpendicular to the current flow are induced. Intuitively, the exchange field of the polarized electron spin could be used to switch the magnet as a first order effect. Yet because of the intrinsic nonlinearity of magnetization dynamics and the strong correlation between magnetic state and the TI surface transport properties, multiple behaviors can be expected.

The typical structure for ferromagnetic insulator (FMI) and TI combination is shown in Fig. 1(a) with the magnet touching TI surface directly and two electrodes are used to drive electron flow on TI surface. Thus the TI surface conductance is affected by the magnet magnetization while the magnetization is modulated by the spin polarization of mobile TI surface electrons in turn. With a coherent transport assumption for TI surface electrons, the fully coupled transport and magnetic dynamics calculation in Ref. [102] revealed multiple operating regimes, including reliable switches and steady oscillations. It couples the magnetization dynamics calculation based on Landau-Lifshitz-Gilbert equation with the transport calculation based on Landau's formula. The transmission probability and propagating electron wavefunction are

solved at each time step, after which the spin polarization is determined as the ensemble of all propagating states. Yet this coherent approach may apply only to the scale shorter than electron coherent length which is hardly achievable at room temperature.

In more realistic devices, the coherence may not hold even if electrons could pass the magnetic barrier ballistically. For large devices or with impure samples when scattering is non-negligible, the transport should be described in the fully diffusive regime. Here, we extend the study on the fully coupled dynamic response to the practical regimes, i.e. the noncoherent ballistic transport and the fully diffusive transport. In these situations, the TI surface spin polarization [$\mathbf{S} = (S_x, S_y, 0)$] and surface electron flow [$\mathbf{J} = (J_x, J_y, 0)$] are correlated by the simple relation $S_x = -J_y/ev_F$ and $S_y = J_x/ev_F$, according to the spin-momentum interlock. Our analysis shows that the nonzero anomalous Hall current along $\hat{y}$ is the key to the multiple dynamic behaviors. In the following, we will discuss the origins of the anomalous Hall current for each transport regimes and analyze their impact on the magnetization dynamics. To clarify the physical picture, we associate the current with electron flow in our illustration.

5.2 Origins of the anomalous Hall current

The mechanisms of the anomalous Hall current are shown schematically in Fig. 1(b) and (c). The in-plane magnetization along $\hat{x}$ shifts the TI surface dispersion relation and causes the transmitted electron to have a net momentum towards $-\hat{y}$ direction, resembling light transmission through media with different refraction index [103]. In the noncoherent ballistic regime, when the magnetic barrier length is comparable to electron mean free path (λ) on TI surface but the temperature is not low enough to ensure coherence, the transmission through the two magnetic boundaries are independent processes and the trajectory beneath the magnet is determined by the refraction at the incoming side [Fig. 1(b)]. Consequently, the nonzero net momentum along $-\hat{y}$ consist the anomalous Hall current and correspondingly a net spin polarization along $-\hat{x}$ is induced. A detailed study of the quasi-optic behavior has been reported in Ref. [103] and an anomalous Hall current ratio (the ratio between the anomalous Hall current and the driving current) around 0.5 was found, which is invariant to the current flow direction. As this anomalous Hall current is only related to the $\hat{x}$ component of magnetization, it can be expresses as $J_y = -\beta_x m_x |J_x|$ where β_x is the anomalous Hall current ratio related to m_x and $\mathbf{m} = \mathbf{M}/|\mathbf{M}| = (m_x, m_y, m_x)$ denotes the normalized magnet magnetization with $|\mathbf{M}| = M_0$ the saturated magnetization. However, for fully diffusive transport, this anomalous Hall current is negligible as the refracted momentum would be quickly relaxed by scatterings and thus $\beta_x = 0$.

On the other hand, the out-of-plane magnetization also induces transverse current by the anomalous Hall effect under both ballistic and diffusive conditions [Fig. 1(c)] [104, 105, 106, 107]. Sizable anomalous Hall effect has been discovered in both magnetically doped and mag-

net capped TI, indicating the potential importance in the coupled magnetization-current response [106, 107, 108]. The physical origin of this effect follows the traditional anomalous Hall effect models with contributions from the intrinsic effect due to electric field induced interband exchange and the extrinsic effects due to impurity scatterings (skew-scattering and side-jumps) [109]. The intrinsic effect has been shown to be dominant for most topological insulator materials [104, 105, 106, 107]. Unfortunately, it is still impossible to give simple governing equations for the amplitude of the anomalous Hall current due to the theoretical complexities. Nevertheless, there are enough results for us to make valid quasi-quantitative assumptions. In particular, three key criteria need to be considered carefully, i.e. the required materials, the scattering dependence and the temperature dependence. Firstly for the material composition, although most experimental reports uses magnetic ion doped TI, Ref. [107] shows the anomalous Hall effect in Bi_2Te_3 covered by $Cr_2Ge_2Te_6$ which is an insulating magnet. Indeed, the exchange Hamiltonian appears in the anomalous Hall theoretical calculation can be induced by surface exchange coupling as well [104, 105]. Thus, the anomalous Hall effect in magnetically capped TI can be equally expected.

The assumptions with respect to scattering and temperature are less trivial due to the lack of direct experimental observations. It is often accepted that the out-of-plane magnetization induced Hall current is dominated intrinsically. This has been demonstrated theoretically in Ref. [105] by comparing the contributions from the band structure, skew-scattering, side-jumps and magnetic impurities. Ref. [108] also reveals the nearly quadratic relation between anomalous Hall resistance ρ_{AH} and the longitudinal resistance ρ_{xx}, which is regarded as the signature of the intrinsic and side-jump contributions. The authors further ruled out the side-jump mechanism by the enhancement at lower carrier density. Given that the intrinsic contribution is independent of electron scattering rate [109], it is expected to exist for both clean samples in the ballistic transport regime and dirty samples in the diffusive regime. This also indicates the robustness over thermal fluctuations at high temperature. Nevertheless, the anomalous Hall voltage all diminishes approaching room temperature in readily reported experiments [108, 106, 107]. The necessary explanation comes with the low Curie temperature and the loss of magnetic order at high temperature. Indeed, all the magnetism measured in these experiments have Curie temperature below 100 K and the magnetic hysteresis loops in magnetic field indicate paramagnetic behaviors at high temperature. The loss of anomalous Hall signal can thus be attributed to the inability to form magnetic order even in high magnetic field around several Tesla. Consequently, if room temperature magnets (e.g. YIG) can be integrated with TI, room temperature anomalous Hall behavior should exist. Similar to the in-plane situation, this component of anomalous Hall current can be express as $J_y = -\beta_z m_z J_x$ where β_z is the anomalous Hall current ratio related to m_z.

5.3 The theoretical model for the influence of anomalous Hall current

With this discussion on anomalous Hall current, we now have a qualitative picture of the coupled TI-magnet system. In the ballistic regime, both in-plane (parallel with the driving current) and out-of-plane magnetization could induce anomalous Hall current, which brings additional spin polarization that affects the magnetization; in the diffusive regime, only the effect of out-of-plane magnetization component needs to be considered because the in-plane magnetization induced anomalous Hall current only exist around the magnetic boundaries so that the effect is negligible in terms of the whole magnet. As the anomalous Hall current induces spin polarization along the driving current direction which affects the magnetization dynamics, it is important to be included for the coupled magnetic-transport simulations. While the relation between anomalous Hall current and the driving current is given in Ref. [103] as a function of TI chemical potential for in-plane magnetization, this relation under out-of-plane magnetization is not exactly clear. Here, instead of going through the complex theoretical models that are still an unsettled research topic, we adopt the experimental measurements and extend their valid conditions to room temperature and general TI samples, validated by the previous discussion. The ratio between the anomalous Hall current and the driving current can be calculated from the measured Hall resistance following the relation $\frac{J_y}{J_x} = -\frac{\rho_{AH}}{\rho_{xx}} = -\beta_z m_z$. With rough estimation, β_z varies around 0.05 based on experimental literature [108, 110, 107]. It should be noted that with $\beta_z > 0$, the anomalous Hall current shows hole conducting characters even though the TI samples measured are almost exclusively n-type, possibly related to special TI surface electronic behaviors which is out of the scope of the current investigation.

Now, it is clear that the unique TI surface transport behaviors can be describe by the two anomalous Hall current ratios $\beta_{x,z}$ and the conductance variation according to magnetization only induces additional fluctuation of the driving current. With the driving current J_x and the corresponding anomalous Hall current $J_y = -\beta_x m_x |J_x| - \beta_z m_z J_x$, the net spin polarization can be expressed by $\mathbf{S} = \frac{J_y}{ev_F}\hat{x} - \frac{J_x}{ev_F}\hat{y}$. Considering that $\mathbf{H} = (H_x, H_y, 0) = \frac{G}{\mu_0 L_z M_0}\mathbf{S}$ with L_z the thickness of the magnet, μ_0 the magnetic constant and G the magnet-TI exchange constant, we have a well defined relation between $\hat{x}$ and $\hat{y}$ components of the exchange magnetic field:

$$H_x = -\beta_x m_x |H_y| + \beta_z m_z H_y \tag{5.1}$$

We will focus on the impact of $\beta_{x,z}$ factors according to the Landau Lifshitz equation in the following.

The Landau-Lifshitz (LL) equation is equivalent to the Landau-Lifshitz-Gilbert (LLG) equa-

tion and is expressed as

$$\frac{\partial \mathbf{m}}{\partial t} = -\frac{\gamma}{1+\alpha^2}\mathbf{m} \times \mathbf{H}_{\text{tot}} - \frac{\gamma\alpha}{1+\alpha^2}\mathbf{m} \times (\mathbf{m} \times \mathbf{H}_{\text{tot}}), \tag{5.2}$$

where γ is the gyromagnetic ratio and α is the Gilbert damping factor adopted from the LLG equation. $\mathbf{H}_{\text{tot}}$ is the total effective field that includes magnet-TI exchange interaction and the anisotropy field of the magnet. The magnetization dependent transport and the thus varying exchange field make it hardly possible to get an analytic solution of this equation. Nevertheless, some deviations could reveal the nontrivial influence of the anomalous Hall current. An immediate observation from Eq. 5.1 is that the the presence of β_x behaves like an additional hard axis anisotropy term along $\hat{x}$ with an anisotropy energy at $\frac{1}{2}\mu_0 M_0 \beta_x |H_y|$. The corresponding influence can be intuitively understood as lowering the barrier for switches between $\pm\hat{x}$ magnetization. Thus, to make the analytic illustration simpler, we ignore the β_x term together with all anisotropy components from the total effective field and focus on β_z which is the most exotic term related to magnetization dynamics. All terms are included in our numerical simulations. Indeed, the anisotropy terms can never be neglected for valid results, unless the magnet is isotropic, which is an extremely rare case.

Thus, considering only the exchange field and β_z, [i.e. $\mathbf{H}_{\text{tot}} = (-\beta_z m_z \hat{x} + \hat{y}) H_y$], the right hand side of Eq. 5.2 becomes

$$\begin{aligned} RHS =& \frac{\gamma}{1+\alpha^2}\left[\begin{pmatrix} m_z \\ 0 \\ -m_x \end{pmatrix} + \beta_z m_z \begin{pmatrix} 0 \\ -m_z \\ m_y \end{pmatrix}\right] H_y \\ &+ \frac{\gamma\alpha}{1+\alpha^2}\left[\begin{pmatrix} -m_x m_y \\ 1-m_y^2 \\ -m_y m_z \end{pmatrix} + \beta_z m_z \begin{pmatrix} 1-m_x^2 \\ -m_x m_y \\ -m_x m_z \end{pmatrix}\right] H_y \\ =& \frac{\gamma}{1+\alpha^2} H_y \begin{pmatrix} m_z - \alpha m_x m_y + \alpha\beta_z m_z \left(1-m_x^2\right) \\ (\alpha-\beta_z)\left(1-m_y^2\right) + \beta_z m_x^2 - \alpha\beta_z m_x m_y m_z \\ -m_x - (\alpha-\beta_z) m_y m_z - \alpha\beta_z m_x m_z^2 \end{pmatrix}. \end{aligned} \tag{5.3}$$

To understand this expression, it is important to note that every component containing α is the result of damping and the rest are due to effective field driven procession. While most of the parts does not show obvious characteristics, the $(\alpha - \beta_z)\left(1 - m_y^2\right)$ term indicates a competition between damping and the anomalous Hall current induced magnetic procession. Without the anomalous current, i.e. $\beta_z = 0$, this term determines that the magnetization would finally align with H_y towards the same direction, because the relaxation term $(\alpha - \beta_z)(1 - m_y^2)$ is strictly positive for any magnetization. However, if $\beta_z > \alpha$, i.e. $\alpha - \beta_z < 0$, this term becomes strictly

negative, the final magnetization could finally align opposite to H_y. When β_z is comparable with α, it effectively cancels the damping so that the magnetization could potentially enter oscillation states. This changes the magnetic dynamics qualitatively. In comparison, the β_x term only mimics hard axis anisotropy, so it could hardly induce any directional reversion of the switching results.

5.4 Simulations of the dynamics behaviors

Fig. 2 shows the several dynamic scenarios caused by nonzero β_z. β_x is set to zero to rule out its influence and this correctly reveals the characters at the full diffusive transport regime. The magnet has a dimension of $90 \times 40 \times 2.2$ nm^3 and a saturation magnetization of 1200 G. A hard axis anisotropy of 25000 J/m^3 along $\hat{y}$ is also assumed. Together with the space anisotropy, this makes the magnet to have an overall easy axis along $\hat{z}$. Diffusive TI surface resistivity ($\rho \sim 10^3$ $\Omega/\square$) and the ballistic transport through the boundaries are included to calculate the current. Its chemical potential u is assumed to 0.05 eV. The driving conditions and the magnet properties vary as illustrated in the caption. For all cases, a positive bias is applied so that electrons flow rightward and the resulting effective field points towards $-\hat{y}$, i.e. $H_y < 0$. Consequently, the intuitive behavior for a normal magnet is to relax to $-\hat{y}$ direction. This is indeed the case shown in Fig. 2(a), when $\alpha = 0.08$. However, if the damping constant is smaller compared to the β_z factor, the final state could reverse according to our previous analysis. This expectation is verified by Fig. 2(b) with $\alpha = 0.01$, which shows almost identical switching dynamics except for the $m_y = 1$ convergence. The trajectories in magnetization space for both situations are shown in Fig. 2(c).

Another important consequence from the competition between α and β_z is the generation of steady oscillations when the two values are comparable, as shown in Fig. 2(d). The oscillation keeps on with negligible damping over our simulation time range (10 ns) although only 3 ns is shown for clarity. The oscillation frequency is also controllable through voltage or the damping factor engineering as will be shown shortly. In addition, the random flip-flops between $\pm\hat{x}$ magnetization also exist as shown in Fig. 2(e). Fig. 2(f) shows the magnetic trajectories for both oscillation and flip-flops. Both of them favors a shifted m_y and develops close to a $m_x m_z$ plane.

For a comprehensive characterization of the multiple magnetic dynamics behavior, we mapped them to voltage and damping variations as shown in Fig. 3. The lines are the boundaries between different behaviors and the background color map shows the frequency of magnetization rotation. Starting from magnetization along $-\hat{x}$, the behaviors can be identified as steady

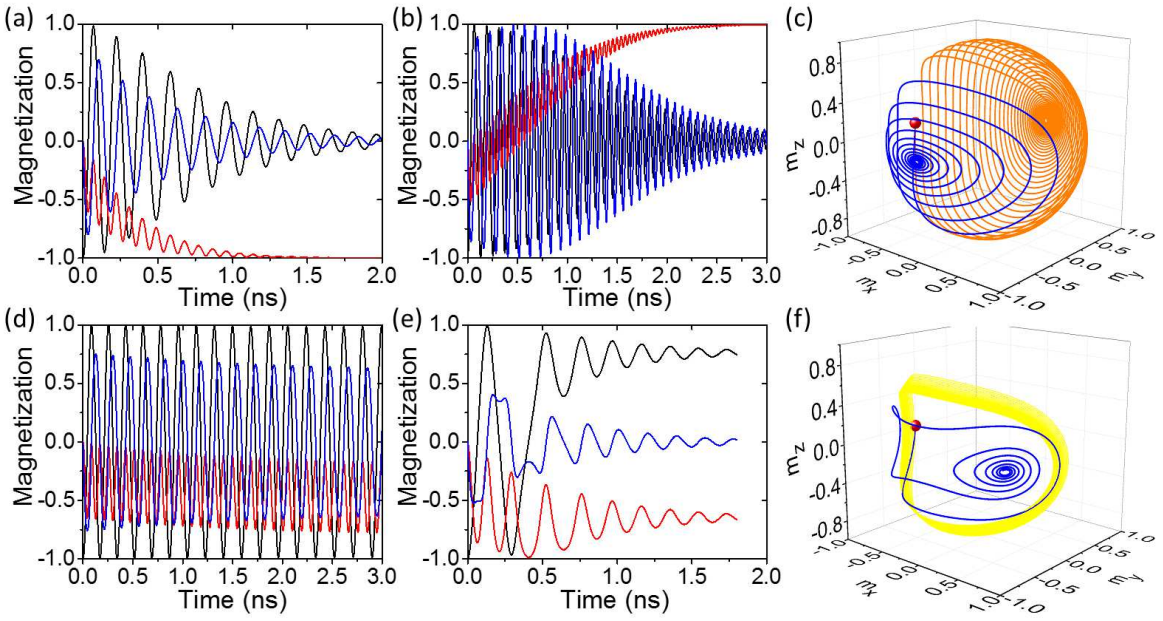

Figure 5.2: Dynamics of magnetization response to driving current with $\beta_z = 0.06$ at different conditions driving voltage V and damping constant α. (a) V=0.25 V, α=0.08; (b) V=0.25 V, α=0.01; (d) V=0.2 V, α=0.03; (e) V=0.15 V, α=0.07. The black, blue and red lines represent m_x, m_y and m_z respectively. (c) and (f) show the corresponding trajectories in the magnetization space. The big red dot marks the initial magnetization.

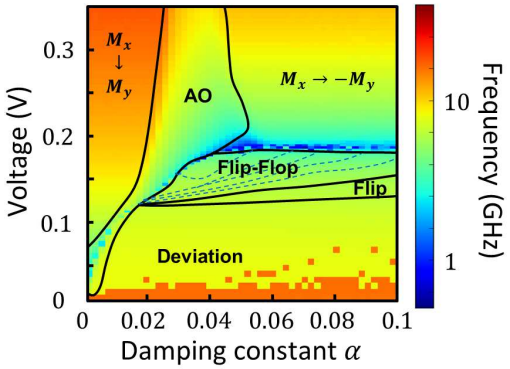

Figure 5.3: The magnetization dynamics behaviors mapped to the voltage-damping variations with $\beta_z = 0.06$. Solid lines draw the boundaries between regions. The dashed lines in the flip-flop region indicate the final magnetization direction could be $\pm\hat{x}$ but hard to define the boundary, which is the feature of the flip-flop region. The background color indicates the corresponding frequency of the magnetic rotations. $\pm M_x$ is not indicated in the legend due to the symmetric behavior.

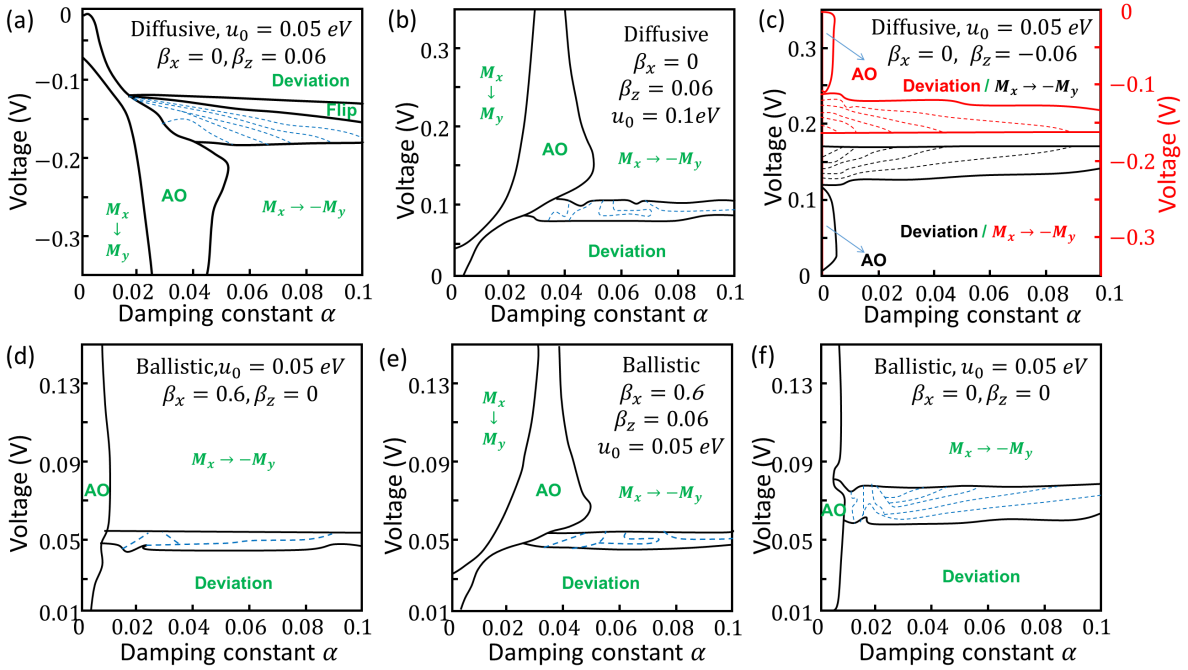

Figure 5.4: The magnetization dynamics map at different conditions. The parameters are as marked in each plot. The regions are as marked by the legends and dashed lines indicate the flip-flop region. In (c) two sets of simulations are shown together with opposite driving bias. The lines and legend are matched to the vertical axis by color.

oscillations, small deviations from $-\hat{x}$, flip-flops between $\pm\hat{x}$, switching to $+\hat{y}$ and the switching to $-\hat{y}$. The switching to $+\hat{y}$ and oscillating regions are the result of the anomalous Hall current ratio β_z, while other regions exist for normal magnetic rotation process as well. As each case covers a well defined portion of the map, they are immune to fluctuations. The magnetization rotation frequencies are measured from the simulated magnetization dynamics. For oscillations, it is the generated oscillating frequency, and for other regions, it is defined based on the rotation period extracted near the convergence. It also shows a controllable behavior with gradual variations expect some abrupt changes at the bifurcation boundaries. For steady oscillation, the available frequency ranges around $1 \sim 10$ GHz, with over one order of magnitude variability.

Moreover, as the exotic behavior is only related to α, reversing the driving current should result in the same behavior. As shown in Fig. 4(a), it is almost exact an upside down version of Fig. 3. Varying the chemical potential, on the other hand, changes the behavior quantitatively [Fig. 4(b)]. It should be noted that the antialignment with the driving field and the steady oscillation only happens for positive β_z, which is the result of the hole anomalous Hall current features of TI surface electrons. Fig. 4(c) shows an artificial verification with $\beta_z < 0$. In this

case, the damping is actually enhanced to $|\alpha - \beta_z|$, so no special behaviors are observed and the symmetry over driving voltage is preserved. It should be noted that this symmetric behavior is defined in terms of the dynamic regimes and it is a result of the noncoherent treatment that leads to Eq. 5.1. In this situation, the driving field can be taken out from the rest part as shown in Eq. 5.3. Yet in a coherent case, when the correlation is more complicated than a β_z factor, the system only shows general electromagnetic behavior, i.e. invariant over simultaneous reversal of magnetization and the driving bias [102].

While the above discussion fully accounted for the influence of β_z, the influence of β_x has to be considered in the noncoherent ballistic regime when the refracted momentum polarization at the boundary could be preserved throughout the magnet. The ballistic transport calculation for each boundary and the magnetization dynamics simulation are combined to map the magnetic behaviors as shown in Fig. 4(d) when β_z is artificially set to zero. Compared with the reference case with both $\beta_{x,z}$ set to zero [Fig. 4(f)], nothing changes expect the lowing of the critical voltage for switching. This is indeed expected as β_x is equivalent to an anisotropy term. The oscillation region, however, is just a result of low damping factor and the magnetization procession is not fully damped over the simulation period. While this condition is set to reveal the influence of β_x, in reality, perpendicular magnetization also induces anomalous Hall current in the ballistic regime as previous mentioned. Thus the system could have both nonzero β_x and β_z simultaneously. The corresponding result is depicted in Fig. 4(e). Compared to the diffusive regime, similar behaviors are observed, while the boundaries have shifted positions. The equivalent hard axis anisotropy helps to decrease the necessary driving force for the switching events.

5.5 Summary

In summary, the fully coupled transport and magnetization dynamics in the magnet-TI hybrid system has been investigated. The existence of the transverse electron flow has been identified as the reason for the unusual antialignment with the driving exchange field and the oscillations under constant channel voltage. To our knowledge, the antialignment is an extraordinary behavior that can be used as the experimental testing criteria. The oscillations are stable as the damping is overcome by the exchange field of the anomalous Hall current. Given that the oscillation is directly generated in insulating magnet with a feature size much small than that can be achieved by Ampere field, this system can be a suitable solution for the spin wave generator in the spin wave logic platform.

Chapter 6

Conductance Singularity on a Topological Insulator Surface with Magnetic Electrodes

6.1 Introduction

At the very dawn of semiconductor electronics, the two-terminal rectifier or diode was known as the device that breaks the conductance invariance with respect to the electric current (or bias) reversal. The significance of this nonlinear property along with the simple physical implementation has made major impacts on all areas of electronics including the information processing, communication, and power systems. On the other hand, the rectification effect in a conventional diode, although well defined under an applied voltage down to tens of mV, attenuates with a smaller signal; the current-voltage relation eventually recovers symmetry across the zero bias.

The physical reason for the reciprocity of low-voltage conductance is based on the principle of detailed equilibrium, i.e., the invariance of scattering characteristics with respect to the exchange of incident and scattered particles [111]. In quantum mechanics, this property is attributed to the Born approximation that is often treated as an universal property of electronic scattering [112]. A more general form is given by the Onsager relation. However, the principle of detailed equilibrium can be broken, if the solid possesses a central symmetry anisotropy, leading to numerous phenomena of fundamental physical interests [112, 113, 114, 115, 116, 117, 118, 119, 120, 121, 122, 123]. Most importantly, the difference in the backward and forward scattering invalidates the assumptions in the reciprocity principles [114, 119, 120]. Nevertheless, accessing the zero-voltage asymmetry remains a challenge. For instance, the conductance discontinuity is absent in most measurements with structural asymmetry even when the transmission probabilities are predicted nonreciprocal [123, 114, 115, 116]. The difficulty to record the asymmetric

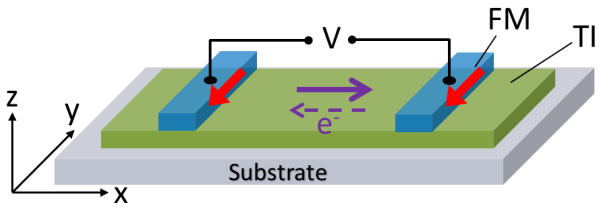

Figure 6.1: A diode-like TI structure with two magnetic electrodes on the top surface. Thin tunnel barriers separate the TI surface and the metallic electrodes (not shown). Two red arrows denote the magnetization direction of the magnets (FM), while V stands for the applied bias. The purple arrows indicate that electrons is easier to flow from the left electrode to the right on corresponding to the magnetization profiles.

boundary scattering stems from the limited difference in the forward and backward trajectory at a low voltage. A system with high intrinsic asymmetry could be far more advantageous in realizing the desired characteristics.

The recently discovered 3D topological insulators (TIs) provide a uniquely promising candidate in this regard. Due to the strong spin-obit interaction, the electron spin on the TI surface is inherently locked to its momentum [22]. Hence, the electron spin polarization follows the surface current and vice versa. For instance, the excitation of spin polarization can stimulate a net charge flow; conversely, the presence of electrical current may induce a chemical potential difference between the spin states [22, 1, 72, 124]. The subsequent directional selectivity should immediately result in the ratchet effect when combined with the ferromagnetic (FM) contacts that enable spin polarized injection and collection. Indeed, a recent measurement illustrated a small difference in the channel resistance at finite positive/negative voltages [125]. Yet for the zero-bias behavior, the transition matrix symmetry based on charge conservation imposes the reciprocal conduction in a two-terminal structure in the ballistic regime. At the same time, theoretical calculations in the literature also reveal the reversible conductance as the initial net polarization quickly undergoes relaxation after a number of scattering events (i.e., the diffusive transport in a long channel) [126, 127]. The desired nonreciprocal response clearly requires additional symmetry breaking while not causing a significant loss of electron spin polarization.

In this work, we propose a solution to the long running challenge by exploiting the advantages of a TI based structure for highly asymmetric conduction at arbitrarily small forward and reverse biases. The key variation from the conventional two-terminal assumption, as shown in Fig. 6.1, is the finite size of the FM electrodes in the driving direction (i.e., x) which are also sufficiently away from the outer edges of the TI sample. Unlike those employing large electrodes, the electrons on the TI surface directly beneath the injecting contact (with the magnetization $\mathbf{M}$ along the y axis) can retain the asymmetric distribution characterized by the

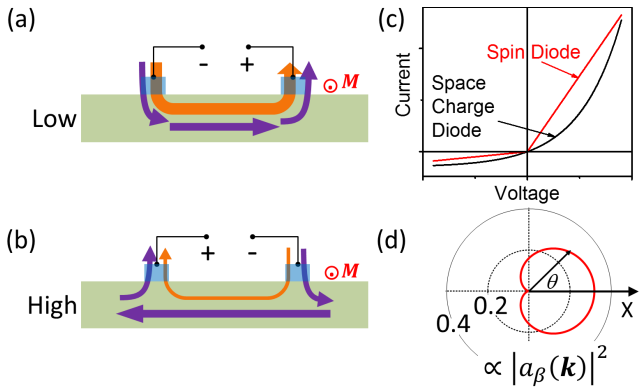

Figure 6.2: (a,b) Schematic illustration of electron flow under the forward (low resistance) and reverse (high resistance) biases, respectively. The total current is the sum of the contributions from the the direct (orange arrows; ballistic paths) and the sequential channels (purple arrows; scattered paths). The magnetization of electrodes is assumed to be along the $-y$ axis. (c) Predicted asymmetric I-V characteristics near the zero bias (red). For comparison, those of a conventional space-charge diode are also shown (black). (d) Normalized tunneling strength $|a_\beta(\mathbf{k})|^2$ between the FM electrode (with the $-y$ magnetization) and the spin-momentum interlocked TI surface states. The area under the curve is set to 1. The result clearly shows the imbalance between the right- and left-moving electron distribution.

spin-momentum interlock once the lateral dimension becomes comparable to the electron mean free path λ (hence, essentially no scattering in the region). In a sense, the TI layer may be considered as a spin sensitive scatterer that separates the electrons in the real space according to their spin momenta−analogous to that in the Stern-Gerlach experiment. Thus, spin specific electron transport can be manifested in the directional conduction so long as the polarization survives the relaxation in the channel.

6.2 Theoretical modeling of the non-reciprocal behavior

The origin of the asymmetry between the opposite bias polarities is more clearly illustrated in Figs. 6.2(a) and 6.2(b). Here, the light (orange) and dark (purple) arrows denote the ballistic and scattered paths, respectively. In the low resistive case [Fig. 6.2(a); forward bias], the electrons injected from the FM contact on average possess the TI surface momenta that are naturally aligned with the applied electrostatic force. Hence, the conduction is primarily via one spin channel directly connecting two electrodes (for both ballistic and non-ballistic transport). Once the sign of the applied voltage is flipped [Fig. 6.2(b); reverse bias], however, the contribution of the direct channel involves the minority spin injection that has a significantly limited capacity and the paths involving spin/momentum altering transition must be accounted for. The nature

of this imbalance is expected to persist when the bias tends asymptotically to zero as shown schematically in Fig. 6.2(c). Nevertheless the nonreciprocal conductance does not yield a non-zero current at zero voltage.

Our theoretical analysis illustrates the presence of nonreciprocity even at infinitesimally small biases, leading to potential discontinuance or a singularity in the channel conductance as the separation between the two electrodes (L) shrinks. In the experimental implementation, the required dimension may not be as demanding as it first looks. While the measurements of λ on the TI surface suggest only about a few nm at the moment, this is due primarily to the poor sample quality. Rather, the projected values limited by the intrinsic electron-phonon interaction could reach several μm once the unintended imperfections can be minimized [82, 81, 83]. Hence, achieving a high-quality material with the critical length around 100 nm appears entirely feasible.

Before examining the details, it is important to note that the finite sizes of the contacts and the distance between them complicate accurate evaluation of the electrical conductance. More specifically, transmission via both the ballistic (direct) and the scattered (sequential) paths must be accounted for simultaneously even when $L \lesssim \lambda$. Following an earlier analysis [see Fig. 6.2(a,b)], this is because some lucky electrons injected with a "wrong" spin (thus, a momentum in the "wrong" direction) can still turn around and complete the conduction despite the restriction on the 180° back scattering. Hence, the widely used treatment based on the Landauer-Büttiker approach is not adequate, requiring further development as discussed below.

The theoretical formulation starts with the description of electrons in the FM electrodes and the TI surface channel. In the actual realization, an atomically thin tunnel barrier may separate them (i.e., the TI and the electrodes) for highly efficient spin polarized injection as well as to avoid the modification of the TI band structure. By considering spin-up and spin-down components explicitly, the eigenfunctions in the electrodes can be written as:

$$\psi_s^{\mathrm{FM}} = \frac{u(\mathbf{r})}{\sqrt{1+s^2}} \begin{pmatrix} -is \\ 1 \end{pmatrix}, \tag{6.1}$$

where s symbolizes the spin index and $u(\mathbf{r})$ is the spatially varying function that is determined by the structure geometry and the constituent material properties. Accordingly, $\langle \psi_s^{\mathrm{FM}} | \sigma_y | \psi_s^{\mathrm{FM}} \rangle = s$, where $s = \pm 1$ corresponds to $\mathbf{M} \parallel \pm\hat{y}$, respectively. On the TI surface, a given spin polarization determines the electron momentum due to the spin-momentum interlock. The two spinor wavefunction on the TI surface is thus described by its wavevector $\mathbf{k} = (k_x, k_y)$ as:

$$\psi_\beta^{\mathrm{TI}} = \frac{w(\mathbf{r})}{\sqrt{2}} \begin{pmatrix} \hbar v_F (i\beta k_x + k_y)/E \\ 1 \end{pmatrix} \exp[i(\beta k_x x + k_y y)], \tag{6.2}$$

where $w(\mathbf{r})$ is the Bloch function (that decays exponentially from the surface along the z axis) and v_F is the Fermi velocity of TI surface electrons ($= 4.5 \times 10^5$ m/s for Bi_2Se_3). When the electrodes are elongated along the y axis as shown, the invariance in this direction can be assumed, enabling the states to be identified by the energy E and transverse wavevector k_y. As such, k_x simply becomes $\sqrt{(E/\hbar v_F)^2 - k_y^2}$ with the factor β denoting the + and − signs for the rightward and leftward traveling components, respectively. Hence, the TI electrons with a given energy and transverse wavevector can be expressed as a linear combination of the two spinor eignefunctions. While k_y can take both positive and negative values, the two components ($\pm$) of the x directional momentum are considered explicitly.

Then, electron transmission between the FM contact and the TI surface states can be treated via the tunneling process as in the scanning tunneling microscope [128]. For instance, the stimulated surface states astride the narrow FM electrode at $x = 0$ can be described as $\Psi_{\mathrm{TI}} = \sum_{\beta=\pm} a_\beta \psi_\beta^{\mathrm{TI}} \theta(\beta x)$, where $\theta(x)$ is the Heaviside step function and the coefficient a_β representing electron injection in each mode simply becomes $\left\langle \psi_\beta^{\mathrm{TI}} | H_t | \psi_s^{\mathrm{FM}} \right\rangle \approx \Delta V_b \left\langle \psi_\beta^{\mathrm{TI}} | \psi_s^{\mathrm{FM}} \right\rangle$ if a scattering potential ΔV_b is adopted as a formal representation for the tunneling Hamiltonian H_t through a uniform barrier. A straightforward calculation subsequently leads to

$$a_\beta(\mathbf{k}) = \tau_0 \frac{E - s\hbar v_F(\beta k_x + i k_y)}{2E}, \tag{6.3}$$

where τ_0 results from ΔV_b and the overlap integral of the spinor-independent parts, $u(\mathbf{r})$ and $w(\mathbf{r})$. The explicit dependence of Eq. (3) on s and β clearly illustrates the influence of spin-momentum selection; i.e., the imbalance between two transport directions when the contact is spin specific. As an example, the normalized directional dependence of $|a_\beta(\mathbf{k})|^2$ is plotted in Fig. 6.2(d) for the case of $s = -1$ (i.e., with the $-y$ magnetization). Evidently, the injected distribution favors the initial momentum along the $+x$ direction with approximately the 80:20 ratio between the majority and minority populations. This preference is independent of the electron energy E. The absorption of TI electrons by the collecting FM electrode can be handled similarly. The only difference is a slight modification in the Heaviside step function for Ψ_{TI} as the $\beta = +$ ($-$) mode now approaches the contact from the left (right).

Following the overlap integral, the direct conduction through the ballistic paths between the two electrodes can be evaluated by treating the TI surface state as the intermediary that couples the FM states. This results in the transmission coefficient $t_{\mathrm{M}}^{\mathrm{M}}(E) \approx -i\pi|\tau_0|^2 \frac{E}{\hbar v_F}\left(1 - \frac{\pi}{4} s\beta\right)$, where the proportionality to the energy originates from the density of modes on the TI surface (Appendix. D). While numerical evaluation of the transmitted flux (i.e., $|t_{\mathrm{M}}^{\mathrm{M}}|^2$) is difficult due to the uncertainty in τ_0, it is outright obvious that the relative ratio of the conductance can be obtained as the polarity of the magnetization and/or the driving bias change. Assuming both electrode are magnetized along the $-y$ axis ($s = -1$), for instance, a switch from the

forward to reverse bias ($\beta = + \rightarrow -$) yields conductance variation as large as 70 to 1 [more precisely, $(1+\pi/4)^2 : (1-\pi/4)^2$]. For convenience, this factor illustrating the dependence on the magnetization and bias polarities is defined as

$$T_{\mathrm{M}}^{\mathrm{M}} = \frac{\left(1 - s\beta\pi/4\right)^2}{2\left(1+\pi^2/16\right)}. \tag{6.4}$$

The denominator normalizes the directional contribution to the sum of both spin states that corresponds to the case of nonmagnetic electrodes. Hence, the actual flux can be obtained formally from the product of $T_{\mathrm{M}}^{\mathrm{M}}$ and the spin-independent, ballistic channel conductance (denoted as $G_{\mathrm{M}}^{\mathrm{M}}$). Following the schematic given in Fig. 6.1, we set $s = -1$ in the ensuing discussion. The case for the $+y$ magnetization (i.e., $s = +1$) can be evaluated similarly.

Along with the ballistic conduction between two FM electrodes, it is necessary to account for the role of the sequential channel involving the scattered paths even when $L \lesssim \lambda$. Due to the finite width of the contact region, the electrons initially injected with the momenta moving away from the collecting contact can turn around after a few scattering events and provide a non-zero contribution. It is particularly relevant if the conduction is in the high resistive (i.e., reverse biased) state as indicated in Fig. 6.2(b). When L is large, on the other hand, the non-ballistic current becomes dominant and the channel conductance converges to the spin-independent diffusive limit. Unfortunately, a rigorous treatment of this complex transport problem is very difficult to attain. Instead, we approach it by estimating the effective length of the non-ballistic paths where the scattering events are modeled as elastic processes. Typically, the additional distance that an electron injected into the "wrong" spin state (thus, the momentum) travels away before experiencing the turn around is of the order of the mean free path λ. Given that the back scattering on the TI surface is suppressed, the average detour $q\lambda$ is somewhat longer than λ with a value around $q \sim 4$ following a simple analysis. A similar process is also encountered in the absorbing electrode, causing additional differences in the paths. Of the two conduction conditions, the high resistive state is again expected to experience stronger reflection due to the spin mismatch and, thus, a longer path on the collecting end [see Fig. 6.2(b)]. We neglect this extra spin (or polarity) selective contribution as it is not crucial in the main focus of the investigation (i.e., demonstrating the nonreciprocal conduction). The resulting approximation tends to underestimate the asymmetry ratio; hence, a rather conservative assumption.

Then, the non-ballistic surface channel conductance can be expressed as

$$G_{\mathrm{TI}}T_{\mathrm{TI}} = G_{\mathrm{TI}} \times \begin{cases} p + (1-p)\frac{1}{(1+q\lambda/L)}, & \text{forward} \\ (1-p) + p\frac{1}{(1+q\lambda/L)}, & \text{reverse} \end{cases} \tag{6.5}$$

Here, G_{TI} represents the classical TI surface conductance and T_{TI} is for the spin/polarity

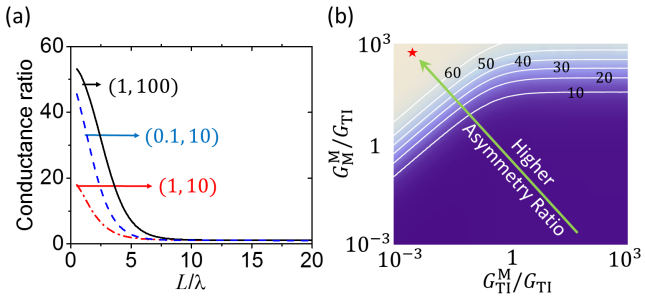

Figure 6.3: (a) Conductance ratio between the forward and reverse biases of infinitesimal amplitude (i.e., the conductance asymmetry or singularity) as a function of the normalized channel length L/λ for three different combinations of ($G^{\rm M}_{\rm TI}/G_{\rm TI}$, $G^{\rm M}_{\rm M}/G_{\rm TI}$). (b) Contour plot of the conductance asymmetry ratio in the $G^{\rm M}_{\rm TI}/G_{\rm TI}$-$G^{\rm M}_{\rm M}/G_{\rm TI}$ parameter space for $L = 3\lambda$. The star indicates the limit of approx. 70 that is set by the purely ballistic transport. The numbers denote the calculated asymmetry values. The lighter (darker) color signifies the higher (lower) ratio.

dependent transport. In addition, the factors p (≈ 0.8) and $1-p$ account for the uneven distribution of the injected electrons between the $+k_x$ and $-k_x$ components as discussed earlier in Fig. 6.2(d). To obtain the contact-to-contact transport characteristics, the (sequential) tunnel resistance between the electrode and the TI ($1/G^{\rm M}_{\rm TI}$) must also be considered. Accordingly, the total resistance in this case becomes $1/G_{\rm TI}T_{\rm TI} + 2/G^{\rm M}_{\rm TI}$.

In a steady state with a nonzero bias V, the total current is obtained by summing the contributions from both the ballistic and non-ballistic transport. Thus, the resulting total conductance [$= I(V)/V$] follows the form:

$$G_{\rm tot}(V) = \left[\exp^{-L/\lambda} G^{\rm M}_{\rm M} T^{\rm M}_{\rm M} + \frac{\frac{\lambda}{L} G_{\rm TI} G^{\rm M}_{\rm TI} T_{\rm TI}}{G^{\rm M}_{\rm TI} + 2\frac{\lambda}{L} G_{\rm TI} T_{\rm TI}}\right]. \tag{6.6}$$

As shown, the exponential decay of the ballistic contribution is considered explicitly while $\frac{\lambda}{L}G_{\rm TI}$ provides the diffusive surface conductance of length L. In this regard, the channel dimension is described in units of λ and $G_{\rm TI}$ corresponds to a normalized value. Under a small voltage, the I-V curve is expected to be linear in each of the forward and reverse bias regions but with different slopes [i.e., $G_{\rm tot}(V) \neq G_{\rm tot}(-V)$]. Such a possibility is evident from the dependence of Eqs. (6.4) and (6.5) on the relevant parameters.

6.3 Results and discussion

For the quantitative results, a parametric study is carried out as the numerical values of $G_{\mathrm{M}}^{\mathrm{M}}$, $G_{\mathrm{TI}}^{\mathrm{M}}$, and G_{TI} are not established. Figure 6.3(a) shows the conductance ratios between the forward and reverse biases of infinitesimal amplitude for three different combinations of $G_{\mathrm{TI}}^{\mathrm{M}}/G_{\mathrm{TI}}$ and $G_{\mathrm{M}}^{\mathrm{M}}/G_{\mathrm{TI}}$. The rapid decay with the increasing L conforms to the relaxation of the spin selective injection through the interaction with the environment. Once $L \gg \lambda$, the transport properties converge to the drift-diffusion equations for all cases under consideration [126]. In the other extreme, the ballistic conduction dominates and a large asymmetry over the factor of 10 can be clearly achieved as desired. For the strong rachet effect, the calculation results also indicate the need for a large $G_{\mathrm{M}}^{\mathrm{M}}$ and/or a small $G_{\mathrm{TI}}^{\mathrm{M}}$ in reference to G_{TI}.

The impact of $G_{\mathrm{TI}}^{\mathrm{M}}/G_{\mathrm{TI}}$ and $G_{\mathrm{M}}^{\mathrm{M}}/G_{\mathrm{TI}}$ is analyzed in greater detail with L fixed at 3λ in Fig. 6.3(b). The star on the upper left corner indicates the limit of approx. 70 set by $T_{\mathrm{M}}^{\mathrm{M}}$. Evidently, the ratio approaches to the maximum when the conductance is dominated by the ballistic transport (i.e., a large $G_{\mathrm{M}}^{\mathrm{M}}/G_{\mathrm{TI}}$). As for the dependence on $G_{\mathrm{TI}}^{\mathrm{M}}/G_{\mathrm{TI}}$, the asymmetry ratio is not a monotonously decreasing function despite the initial impression. At the low limit, the large tunnel resistance between the electrode and the TI effectively blocks the sequential conduction involving the scattered paths, leaving the ratio to follow that of the direct conduction via ballistic paths. This diminishes any contribution from T_{TI} [Eq. (6.5)] for the asymmetry. Once $G_{\mathrm{TI}}^{\mathrm{M}}$ increases, the scattered paths start to draw the current and the ratio decreases rapidly as expected (i.e., a more significant role of the diffusive regime with a smaller ratio). When $G_{\mathrm{TI}}^{\mathrm{M}}$ becomes even larger toward the high limit, the asymmetry ratio deviates somewhat from the simple decay with the value determined by the interplay between $G_{\mathrm{M}}^{\mathrm{M}}T_{\mathrm{M}}^{\mathrm{M}}$ and $G_{\mathrm{TI}}T_{\mathrm{TI}}$. One potential complication is that $G_{\mathrm{TI}}^{\mathrm{M}}$ and $G_{\mathrm{M}}^{\mathrm{M}}$ may not be controlled independently as both of them are related to the tunneling characteristics. Nonetheless, a thinner tunnel barrier is preferred since ensuring a large contribution from the ballistic paths is more crucial for high asymmetry.

In summary, the nonreciprocal conductance between two narrow magnetic electrodes on a TI surface is predicated. This phenomenon requires that the distance between electrodes be comparable to the electron mean free path and the electrodes far from the TI boundaries to minimize the relaxation. The spin selective effect of the magnetic electrodes coupled with the intrinsic spin-momentum interlock causes the conductance imbalance which is far more significant than that based on the structural asymmetry. Our theoretical estimate indicates a clearly measurable nonreciprocal conductance between the forward and reverse biases even at infinitesimally small voltages. A key for experimental verification at room temperature is the improved sample quality as the characteristic dimension is limited by λ.

Chapter 7

Summary and future research

In this thesis, a list of novel devices have been proposed and extensively evaluated. This research is intrigue by the need to sustain the increasing capability of information processing and inspired by the new material properties. If we look into the variables, for which artificial manipulations can be induced based on our current physics knowledge, they falls upon three categories, i.e. electronics, photonics and magnetism. Until so far, these three systems are treated independently in our information processing systems and conversion devices are used in the connections. The logic operations are mainly accomplished in electronics, while photonics and magnetism are almost exclusively for communication and data storage respectively. The close entanglement of these systems with intrinsic controllability has been shown as a breaking point for potential new devices during the recent decade.

What topological insulator offers is the intrinsic correlation between electronic states and the magnetism (in terms of electron spin). As its electron momentum is coupled to electron spin, by controlling one, the other could be modulated. Given that the momentum is directly related to electric biases and visa versa, electric signals and magnetic signals can thus be integrated. This founds the basic notion for the devices listed in this thesis.

The most immediate and straightforward one is to control magnetization electrically. Chapter. 2 presents such a proposal. When a thin magnet is attached to TI surface, the exchange interaction between the surface magnetic ions of the magnet and the surface electronic states of TI cause the system free energy to depend on both magnetization and TI Fermi level. Setting the Fermi level to the Dirac point could significantly reduce the total free energy for out-of-plane magnetization. This is equivalent to an additional easy axis anisortopy term along the vertical direction that is controlled by a gate bias. Once the 90° magnetization rotation between in-plane and out-of-plane is controlled by the gate bias, the whole 180° switches can be achieved by accompanying the gate control with a TI surface current which is naturally spin polarized. The whole switching operation follows the Bennett clocking scheme. A detailed study of this

switching scheme is presented in Chapter. 2. The operating speed and reliability are verified by numerical simulations.

This switching scheme is also the foundation for the spin logic platform depicted in Chapter. 3. A necessary change is to use a graphene channel to supply the spin signal to accomplish the 180° switches. This decouples the spin signal from the direction of electron flow, so that the signal can be determined by the magnetization of cells at the upstream. More specifically, the spin polarization injected beneath the target magnet is determined by the spin dependent barrier at the upstream magnetic cell. Both cell to cell operations and a simple circuit of a 1-bit adder are discussed in Chapter. 3 to validate this platform. In addition, Section. 3.3.2 also validated an electrostatic approach to induce cell-to-cell interaction which leads to the ultra-low energy consumption, at attoJoule level per switch.

Chapter. 3 and Chapter. 2 has focused on the electric control of magnetization that the magnet's influences on TI surface transport properties are safely ignored in their setups. Such influences are investigated in Chapter. 4, assuming the magnetization is pinned or controlled by other means. The exchange interaction from the magnet changes the TI band structure. In-plane magnetization induces band shift in the $k_x k_y$ space and out-of-plane magnetization opens a band gap. These modifications strongly affects electron transport. Particularly, as the Dirac equation has the same duality compared to Maxwell's equations, the shift in k-space could result in electron transmission through a magnetic boundary similar to that of light transmission materials with different refraction index. Refraction of electron flow happens, which forms a transverse flow as the anomalous Hall current at the boundary. For low energy electrons, the band shift induced virtual band gap could confine the electron propagation. Such confinement by magnetic strips combined with a switching magnetic valve enables a switching type device that is proposed in Section. 4.3, resembling CMOS operations.

On the other hand, if the interdependence between magnetization and TI surface transport is fully considered, highly non-linear behaviors are discovered. In this scenario, both the magnetization and channel current vary simultaneously and several unusual dynamic behaviors are found. Most notably, the final magnetization may anti-align with the driving exchange field. This is found to be due to the secondary exchange field from the anomalous Hall current induced by the out-of-plane component of the magnetization. Normal behaviors are restored if the damping effect is large enough. At the intermediate stage, steady state oscillations happen, which can be used as efficient spin wave generators in magnetic insulators.

In Chapter. 6, the usage of magnetic metal is considered. Unlike magnetic insulators, direct contact of metal with TI would induce unwanted pinning of the surface state. Thus, the effect of spin polarized injection and absorption is the focus. We found the initial spin polarization together with the spin-momentum interlock effect of TI surface state leads to non-reciprocal conductance between two magnetic electrodes magnetized in parallel. An intuitive reason is that

the spin-momentum interlock causes the electron flow to favor a certain direction depending on its spin, and when the driving voltage is against this preference, the channel would show a high resistance. Such a phenomenon is modeled phenomenologically in Chapter. 6.

In a retrospect of all the devices proposed in this thesis, they follow a general routine of active electronics combined with passive magnetism, i.e. the power source and controlling signals are electric biases. This is natural logic as most systems rely on electric power and electric controls are easy with mature switches. Nevertheless, the other scenario also worth notice, i.e. active magnetic rotations induce passive electric signals. This notion is inspired by the proposal of spin wave logic and the well developed magnetic resonance studies on magnetic insulators. They indicate that magnetic rotations can be excited by either injecting spin wave or supplying electromagnetic wave at the microwave frequency. It is thus an interesting question if the system presented in Chapter. 5 can be used as a sourceless receiver (with electric biasing source through the channel, it surely could be used to detect the magnetic signal by conductance monitoring). The electrons redistribution as a response of the magnetization rotations needs to be modeled to answer this question. It is highly possible that electrons would distribute according to the magnetization or the direction of magnetic rotation, thus generating a voltage signal astride the magnet.

As it is mentioned at the beginning of this section, the integration of photonics with magnetism and electronics is also potentially productive. While the passive electronic response to magnetic oscillations could be a way to receive microwave signal, more close correlation is preferred for high efficiency and better performance. A possible proposal is use the TI-magnet heterostructure or magnetically doped TI as unit cells for photonic crystals. As has been presented in Chapter. 2 that a gate voltage could modulate the anisotropy profiles in such unit cells, the effective permittivity would be modulated resultingly. Thus the photonic response of the photonic crystal as whole could be electrically modulated. Such studies would require the equivalent permeability of each unit cell to be modeled according to the electronic/magnetic states. Finite difference time domain (FDTD) method could then be applied to numerically simulate the photonic behaviors.

REFERENCES

[1] Yuriy G. Semenov, Xiaopeng Duan, and Ki Wook Kim. Electrically controlled magnetization in ferromagnet-topological insulator heterostructures. *Physical Review B*, 86(16):161406, October 2012. Cited by 0001.

[2] W. Prellier, A. Fouchet, and B. Mercey. Oxide-diluted magnetic semiconductors: a review of the experimental status. *Journal of Physics: Condensed Matter*, 15(37):R1583, September 2003.

[3] Kevin R. Kittilstved, William K. Liu, and Daniel R. Gamelin. Electronic structure origins of polarity-dependent high-TC ferromagnetism in oxide-diluted magnetic semiconductors. *Nature Materials*, 5(4):291–297, April 2006.

[4] K. Sato, L. Bergqvist, J. Kudrnovsk, P. H. Dederichs, O. Eriksson, I. Turek, B. Sanyal, G. Bouzerar, H. Katayama-Yoshida, V. A. Dinh, T. Fukushima, H. Kizaki, and R. Zeller. First-principles theory of dilute magnetic semiconductors. *Reviews of Modern Physics*, 82(2):1633–1690, May 2010.

[5] Tomasz Dietl. A ten-year perspective on dilute magnetic semiconductors and oxides. *Nature Materials*, 9(12):965–974, December 2010.

[6] J. M. D. Coey. Dilute magnetic oxides. *Current Opinion in Solid State and Materials Science*, 10(2):83–92, April 2006.

[7] D.C. Ralph and M.D. Stiles. Spin transfer torques. *Journal of Magnetism and Magnetic Materials*, 320(7):1190–1216, April 2008.

[8] Luqiao Liu, Chi-Feng Pai, Y. Li, H. W. Tseng, D. C. Ralph, and R. A. Buhrman. Spin-torque switching with the giant spin hall effect of tantalum. *Science*, 336(6081):555–558, May 2012.

[9] Supriyo Datta, Sayeef Salahuddin, and Behtash Behin-Aein. Non-volatile spin switch for boolean and non-boolean logic. *Applied Physics Letters*, 101(25):252411, December 2012.

[10] J.A. Currivan, Youngman Jang, M.D. Mascaro, M.A. Baldo, and C.A. Ross. Low energy magnetic domain wall logic in short, narrow, ferromagnetic wires. *IEEE Magnetics Letters*, 3:3000104–3000104, 2012.

[11] D.E. Nikonov, G.I. Bourianoff, and T. Ghani. Proposal of a spin torque majority gate logic. *IEEE Electron Device Letters*, 32(8):1128–1130, August 2011.

[12] A. Lyle, S. Patil, J. Harms, B. Glass, X. Yao, D. Lilja, and Jian-Ping Wang. Magnetic tunnel junction logic architecture for realization of simultaneous computation and communication. *IEEE Transactions on Magnetics*, 47(10):2970–2973, 2011.

[13] Behtash Behin-Aein, Deepanjan Datta, Sayeef Salahuddin, and Supriyo Datta. Proposal for an all-spin logic device with built-in memory. *Nat Nano*, 5(4):266–270, April 2010. Cited by 0112.

[14] R. Ramesh and Nicola A. Spaldin. Multiferroics: progress and prospects in thin films. *Nature Materials*, 6(1):21–29, January 2007.

[15] C. a. F. Vaz. Electric field control of magnetism in multiferroic heterostructures. *Journal of Physics: Condensed Matter*, 24(33):333201, August 2012.

[16] A. H. Castro Neto, F. Guinea, N. M. R. Peres, K. S. Novoselov, and A. K. Geim. The electronic properties of graphene. *Reviews of Modern Physics*, 81(1):109, January 2009.

[17] M. I. Katsnelson, K. S. Novoselov, and A. K. Geim. Chiral tunnelling and the klein paradox in graphene. *Nature Physics*, 2(9):620–625, September 2006.

[18] Jiahao Kang, Deblina Sarkar, Yasin Khatami, and Kaustav Banerjee. Proposal for all-graphene monolithic logic circuits. *Applied Physics Letters*, 103(8):083113, August 2013.

[19] J. R. Williams, Tony Low, M. S. Lundstrom, and C. M. Marcus. Gate-controlled guiding of electrons in graphene. *Nature Nanotechnology*, 6(4):222–225, 2011. Cited by 0047.

[20] Wei Han, K.M. McCreary, K. Pi, W.H. Wang, Yan Li, H. Wen, J.R. Chen, and R.K. Kawakami. Spin transport and relaxation in graphene. *Journal of Magnetism and Magnetic Materials*, 324(4):369–381, February 2012. Cited by 0009.

[21] Fan-Ming Zhang, Ying He, and Xi Chen. Guided modes in graphene waveguides. *Applied Physics Letters*, 94(21):212105, May 2009.

[22] M. Z. Hasan and C. L. Kane. Colloquium: Topological insulators. *Reviews of Modern Physics*, 82(4):3045–3067, November 2010.

[23] Y. L. Chen, J.-H. Chu, J. G. Analytis, Z. K. Liu, K. Igarashi, H.-H. Kuo, X. L. Qi, S. K. Mo, R. G. Moore, D. H. Lu, M. Hashimoto, T. Sasagawa, S. C. Zhang, I. R. Fisher, Z. Hussain, and Z. X. Shen. Massive dirac fermion on the surface of a magnetically doped topological insulator. *Science*, 329(5992):659–662, August 2010. Cited by 0264.

[24] X. F. Kou, W. J. Jiang, M. R. Lang, F. X. Xiu, L. He, Y. Wang, Y. Wang, X. X. Yu, A. V. Fedorov, P. Zhang, and K. L. Wang. Magnetically doped semiconducting topological insulators. *Journal of Applied Physics*, 112(6):063912–063912–6, September 2012.

[25] T. Schlenk, M. Bianchi, M. Koleini, A. Eich, O. Pietzsch, T. O. Wehling, T. Frauenheim, A. Balatsky, J.-L. Mi, B. B. Iversen, J. Wiebe, A. A. Khajetoorians, Ph. Hofmann, and R. Wiesendanger. Controllable magnetic doping of the surface state of a topological insulator. *Physical Review Letters*, 110(12):126804, March 2013.

[26] Jian-Min Zhang, Wenguang Zhu, Ying Zhang, Di Xiao, and Yugui Yao. Tailoring magnetic doping in the topological insulator bi2se3. *Physical Review Letters*, 109(26):266405, December 2012.

[27] B. D. Kong, Y. G. Semenov, C. M. Krowne, and K. W. Kim. Unusual magnetoresistance in a topological insulator with a single ferromagnetic barrier. *Applied Physics Letters*, 98(24):243112–243112–3, June 2011. Cited by 0019.

[28] Takehito Yokoyama. Current-induced magnetization reversal on the surface of a topological insulator. *Physical Review B*, 84(11):113407, 2011.

[29] Ion Garate and M. Franz. Inverse spin-galvanic effect in the interface between a topological insulator and a ferromagnet. *Physical Review Letters*, 104(14):146802, April 2010.

[30] Kentaro Nomura and Naoto Nagaosa. Electric charging of magnetic textures on the surface of a topological insulator. *Physical Review B*, 82(16):161401, October 2010.

[31] Yunyou Yang, Zhong Xu, L. Sheng, R. Shen, and D. Y. Xing. Magnetoresistance in an ultrathin bi2se3 film between two ferromagnetic insulators. *Applied Physics Letters*, 99(18):182101, October 2011.

[32] Weidong Luo and Xiao-Liang Qi. Massive dirac surface states in topological insulator/magnetic insulator heterostructures. *Physical Review B*, 87(8):085431, February 2013. 00000.

[33] A. J. Jacobson and B. E. F. Fender. Covalency parameters in MnSe and MnSe2. *The Journal of Chemical Physics*, 52(9):4563, May 1970. 00000.

[34] Sumit Mandal and Shyamal K. Saha. Ni/graphene/ni nanostructures for spintronic applications. *Nanoscale*, 4(3):986–990, January 2012. 00006.

[35] Jian-Gang Zhu. Magnetoresistive random access memory: The path to competitiveness and scalability. *Proceedings of the IEEE*, 96(11):1786 –1798, November 2008. Cited by 0059.

[36] G. Prenat, B. Dieny, Wei Guo, M. El Baraji, V. Javerliac, and J.-P. Nozieres. Beyond MRAM, CMOS/MTJ integration for logic components. *IEEE Transactions on Magnetics*, 45(10):3400 –3405, October 2009.

[37] Shoun Matsunaga, Jun Hayakawa, Shoji Ikeda, Katsuya Miura, Haruhiro Hasegawa, Tetsuo Endoh, Hideo Ohno, and Takahiro Hanyu. Fabrication of a nonvolatile full adder based on logic-in-memory architecture using magnetic tunnel junctions. *Applied Physics Express*, 1(9):091301, 2008. Cited by 0140.

[38] Ki-Seung Lee, Seo-Won Lee, Byoung-Chul Min, and Kyung-Jin Lee. Threshold current for switching of a perpendicular magnetic layer induced by spin hall effect. *Applied Physics Letters*, 102(11):112410, March 2013.

[39] T. Maruyama, Y. Shiota, T. Nozaki, K. Ohta, N. Toda, M. Mizuguchi, A. A. Tulapurkar, T. Shinjo, M. Shiraishi, S. Mizukami, Y. Ando, and Y. Suzuki. Large voltage-induced magnetic anisotropy change in a few atomic layers of iron. *Nature Nanotechnology*, 4(3):158–161, March 2009.

[40] Kuntal Roy, Supriyo Bandyopadhyay, and Jayasimha Atulasimha. Hybrid spintronics and straintronics: A magnetic technology for ultra low energy computing and signal processing. *Applied Physics Letters*, 99(6):063108, August 2011.

[41] E. Liu, J. Z. Zhang, W. Zhang, P. K. J. Wong, L. Y. Lv, Y. Zhai, J. Wu, Y. B. Xu, and H. R. Zhai. Influence of au capping layer on the magnetic properties of ultrathin epitaxial fe3o4/GaAs(001) film. *Journal of Applied Physics*, 109(7):07C121, April 2011.

[42] Wei-Gang Wang, Mingen Li, Stephen Hageman, and C. L. Chien. Electric-field-assisted switching in magnetic tunnel junctions. *Nature Materials*, 11(1):64–68, 2012. Cited by 0000.

[43] Gary A. Prinz. Hybrid ferromagnetic-semiconductor structure. *Science*, 250(4984):1092–1097, November 1990.

[44] Yu. S. Dedkov, A. Generalov, E. N. Voloshina, and M. Fonin. Structural and electronic properties of fe3o4/graphene/ni(111) junctions. *physica status solidi (RRL) Rapid Research Letters*, 5(7):226–228, July 2011.

[45] Y. G. Semenov, J. M. Zavada, and K. W. Kim. Electrical control of exchange bias mediated by graphene. *Physical Review Letters*, 101(14):147206, October 2008.

[46] X. Hao, J. S. Moodera, and R. Meservey. Thin-film superconductor in an exchange field. *Physical Review Letters*, 67(10):1342–1345, September 1991.

[47] Martin Weisheit, Sebastian Fhler, Alain Marty, Yves Souche, Christiane Poinsignon, and Dominique Givord. Electric field-induced modification of magnetism in thin-film ferromagnets. *Science*, 315(5810):349–351, January 2007.

[48] Charles H. Bennett. The thermodynamics of computationa review. *International Journal of Theoretical Physics*, 21(12):905–940, December 1982.

[49] Ivan Cimrk. A survey on the numerics and computations for the landau-lifshitz equation of micromagnetism. *Archives of Computational Methods in Engineering*, 15(3):277–309, September 2008.

[50] C. Augustine, G. Panagopoulos, B. Behin-Aein, S. Srinivasan, A. Sarkar, and K. Roy. Low-power functionality enhanced computation architecture using spin-based devices. In *2011 IEEE/ACM International Symposium on Nanoscale Architectures (NANOARCH)*, pages 129 –136, June 2011.

[51] Giorgio Bertotti, I.D. Mayergoyz, C. Serpico, and M. D'Aquino. Geometrical analysis of precessional switching and relaxation in uniformly magnetized bodies. *IEEE Transactions on Magnetics*, 39(5):2501–2503, 2003.

[52] William Fuller Brown. Thermal fluctuations of a single-domain particle. *Physical Review*, 130(5):1677–1686, June 1963. Cited by 2021.

[53] D.V. Berkov. Fast switching of magnetic nanoparticles: simulation of thermal noise effects using the langevin dynamics. *IEEE Transactions on Magnetics*, 38(5):2489–2495, 2002.

[54] Dmitri V. Berkov. Magnetization dynamics including thermal fluctuations: Basic phenomenology, fast remagnetization processes and transitions over high-energy barriers. In *Handbook of Magnetism and Advanced Magnetic Materials*. John Wiley & Sons, Ltd, 2007.

[55] D. Pantel, S. Goetze, D. Hesse, and M. Alexe. Reversible electrical switching of spin polarization in multiferroic tunnel junctions. *Nature Materials*, 11(4):289–293, April 2012. 00048.

[56] D. Chiba, M. Sawicki, Y. Nishitani, Y. Nakatani, F. Matsukura, and H. Ohno. Magnetization vector manipulation by electric fields. *Nature*, 455(7212):515–518, September 2008. 00255.

[57] K. L. Wang, J. G. Alzate, and P. Khalili Amiri. Low-power non-volatile spintronic memory: STT-RAM and beyond. *Journal of Physics D: Applied Physics*, 46(7):074003, February 2013. 00004.

[58] Dmytro Pesin and Allan H. MacDonald. Spintronics and pseudospintronics in graphene and topological insulators. *Nature Materials*, 11(5):409–416, May 2012.

[59] Hvard Haugen, Daniel Huertas-Hernando, and Arne Brataas. Spin transport in proximity-induced ferromagnetic graphene. *Physical Review B*, 77(11):115406, March 2008. Cited by 0162.

[60] H. X. Yang, A. Hallal, D. Terrade, X. Waintal, S. Roche, and M. Chshiev. Proximity effects induced in graphene by magnetic insulators: First-principles calculations on spin filtering and exchange-splitting gaps. *Physical Review Letters*, 110(4):046603, January 2013.

[61] Adrian G. Swartz, Patrick M. Odenthal, Yufeng Hao, Rodney S. Ruoff, and Roland K. Kawakami. Integration of the ferromagnetic insulator EuO onto graphene. *ACS Nano*, 6(11):10063–10069, November 2012.

[62] X. Duan, V. A. Stephanovich, Y. G. Semenov, and K. W. Kim. Magnetic domain wall transfer via graphene mediated electrostatic control. *Applied Physics Letters*, 101(1):013103–013103–4, July 2012. Cited by 0000.

[63] Qi I. Yang, Merav Dolev, Li Zhang, Jinfeng Zhao, Alexander D. Fried, Elizabeth Schemm, Min Liu, Alexander Palevski, Ann F. Marshall, Subhash H. Risbud, and Aharon Kapitulnik. Emerging weak localization effects on a topological insulatorinsulating ferromagnet (bi2se3-EuS) interface. *Physical Review B*, 88(8):081407, August 2013.

[64] A. R. Akhmerov and C. W. J. Beenakker. Boundary conditions for dirac fermions on a terminated honeycomb lattice. *Physical Review B*, 77(8):085423, February 2008.

[65] S. A. Thiele, J. A. Schaefer, and F. Schwierz. Modeling of graphene metal-oxide-semiconductor field-effect transistors with gapless large-area graphene channels. *Journal of Applied Physics*, 107(9):094505–094505–8, May 2010.

[66] Y. G. Semenov, K. W. Kim, and J. M. Zavada. Spin field effect transistor with a graphene channel. *Applied Physics Letters*, 91(15):153105, October 2007.

[67] S.C. Chan, Kenneth L. Shepard, and P.J. Restle. Distributed differential oscillators for global clock networks. *IEEE Journal of Solid-State Circuits*, 41(9):2083–2094, 2006.

[68] J. Kiermaier, S. Breitkreutz, I. Eichwald, M. Engelstdter, X. Ju, G. Csaba, D. Schmitt-Landsiedel, and M. Becherer. Information transport in field-coupled nanomagnetic logic devices. *Journal of Applied Physics*, 113(17):17B902–17B902–3, March 2013.

[69] Xiaofeng Yao, Jonathan Harms, A. Lyle, F. Ebrahimi, Yisong Zhang, and Jian-Ping Wang. Magnetic tunnel junction-based spintronic logic units operated by spin transfer torque. *IEEE Transactions on Nanotechnology*, 11(1):120–126, January 2012.

[70] A. Imre, G. Csaba, L. Ji, A. Orlov, G. H. Bernstein, and W. Porod. Majority logic gate for magnetic quantum-dot cellular automata. *Science*, 311(5758):205–208, January 2006. Cited by 0441.

[71] M. Sharad, C. Augustine, G. Panagopoulos, and K. Roy. Spin-based neuron model with domain-wall magnets as synapse. *IEEE Transactions on Nanotechnology*, 11(4):843–853, 2012.

[72] Xiaodong Li, Xiaopeng Duan, and Ki Wook Kim. Controlling electron propagation on a topological insulator surface via proximity interactions. *Physical Review B*, 89(4):045425, January 2014.

[73] Vadim V. Cheianov, Vladimir Fal'ko, and B. L. Altshuler. The focusing of electron flow and a veselago lens in graphene p-n junctions. *Science*, 315(5816):1252–1255, March 2007.

[74] Tony Low and Joerg Appenzeller. Electronic transport properties of a tilted graphene p-n junction. *Physical Review B*, 80(15):155406, October 2009.

[75] Ren Hammer, Christian Ertler, and Walter Ptz. Solitonic dirac fermion wave guide networks on topological insulator surfaces. *Applied Physics Letters*, 102(19):193514, May 2013.

[76] P. E. Allain and J. N. Fuchs. Klein tunneling in graphene: optics with massless electrons. *arXiv:1104.5632*, April 2011. Eur. Phys. J. B 83, 301-317 (2011).

[77] Huiwen Ji, J. M. Allred, Ni Ni, Jing Tao, M. Neupane, A. Wray, S. Xu, M. Z. Hasan, and R. J. Cava. Bulk intergrowth of a topological insulator with a room-temperature ferromagnet. *Physical Review B*, 85(16):165313, April 2012.

[78] Min Seok Jang, Hyungjun Kim, Harry A. Atwater, and William A. Goddard Iii. Time dependent behavior of a localized electron at a heterojunction boundary of graphene. *Applied Physics Letters*, 97(4):043504, July 2010.

[79] Ren Hammer and Walter Ptz. Staggered grid leap-frog scheme for the dirac equation. *Computer Physics Communications*, 185(1):40–52, January 2014.

[80] Chaoyu Chen, Zhuojin Xie, Ya Feng, Hemian Yi, Aiji Liang, Shaolong He, Daixiang Mou, Junfeng He, Yingying Peng, Xu Liu, Yan Liu, Lin Zhao, Guodong Liu, Xiaoli Dong, Jun Zhang, Li Yu, Xiaoyang Wang, Qinjun Peng, Zhimin Wang, Shenjin Zhang, Feng Yang, Chuangtian Chen, Zuyan Xu, and X. J. Zhou. Tunable dirac fermion dynamics in topological insulators. *Scientific Reports*, 3, August 2013.

[81] J. A. Sobota, S. Yang, J. G. Analytis, Y. L. Chen, I. R. Fisher, P. S. Kirchmann, and Z.-X. Shen. Ultrafast optical excitation of a persistent surface-state population in the topological insulator bi2se3. *Physical Review Letters*, 108(11):117403, March 2012.

[82] Yuri D. Glinka, Sercan Babakiray, Trent A. Johnson, Alan D. Bristow, Mikel B. Holcomb, and David Lederman. Ultrafast carrier dynamics in thin-films of the topological insulator bi2se3. *Applied Physics Letters*, 103(15):151903, October 2013.

[83] A. Crepaldi, F. Cilento, B. Ressel, C. Cacho, J. C. Johannsen, M. Zacchigna, H. Berger, Ph. Bugnon, C. Grazioli, I. C. E. Turcu, E. Springate, K. Kern, M. Grioni, and F. Parmigiani. Evidence of reduced surface electron-phonon scattering in the conduction band of bi2se3 by nonequilibrium ARPES. *Physical Review B*, 88(12):121404, September 2013.

[84] Xiao-Liang Qi, Taylor L. Hughes, and Shou-Cheng Zhang. Topological field theory of time-reversal invariant insulators. *Physical Review B*, 78(19):195424, November 2008.

[85] Dashdeleg Baasanjav, O. A. Tretiakov, and Kentaro Nomura. Magnetoelectric effect in topological insulator films beyond the linear response regime. *Physical Review B*, 90(4):045149, July 2014.

[86] S. Kanai, M. Yamanouchi, S. Ikeda, Y. Nakatani, F. Matsukura, and H. Ohno. Electric field-induced magnetization reversal in a perpendicular-anisotropy CoFeB-MgO magnetic tunnel junction. *Applied Physics Letters*, 101(12):122403, September 2012.

[87] Yoichi Shiota, Takayuki Nozaki, Frdric Bonell, Shinichi Murakami, Teruya Shinjo, and Yoshishige Suzuki. Induction of coherent magnetization switching in a few atomic layers of FeCo using voltage pulses. *Nature Materials*, 11(1):39–43, January 2012.

[88] Tao Wu, Alexandre Bur, Ping Zhao, Kotekar P. Mohanchandra, Kin Wong, Kang L. Wang, Christopher S. Lynch, and Gregory P. Carman. Giant electric-field-induced reversible and permanent magnetization reorientation on magnetoelectric ni/(011) [pb(mg1/3nb2/3)o3](1x)[PbTiO3]x heterostructure. *Applied Physics Letters*, 98(1):012504, January 2011.

[89] Jian-Gang (Jimmy) Zhu and Chando Park. Magnetic tunnel junctions. *Materials Today*, 9(11):36–45, November 2006.

[90] S. Ikeda, J. Hayakawa, Young Min Lee, F. Matsukura, Yuzo Ohno, T. Hanyu, and H. Ohno. Magnetic tunnel junctions for spintronic memories and beyond. *IEEE Transactions on Electron Devices*, 54(5):991–1002, 2007. 00201.

[91] Jia-Mian Hu, Zheng Li, Long-Qing Chen, and Ce-Wen Nan. High-density magnetoresistive random access memory operating at ultralow voltage at room temperature. *Nature Communications*, 2:553, November 2011.

[92] Jian Zhu, J. A. Katine, Graham E. Rowlands, Yu-Jin Chen, Zheng Duan, Juan G. Alzate, Pramey Upadhyaya, Juergen Langer, Pedram Khalili Amiri, Kang L. Wang, and Ilya N. Krivorotov. Voltage-induced ferromagnetic resonance in magnetic tunnel junctions. *Physical Review Letters*, 108(19):197203, May 2012.

[93] T. Schneider, A. A. Serga, B. Leven, B. Hillebrands, R. L. Stamps, and M. P. Kostylev. Realization of spin-wave logic gates. *Applied Physics Letters*, 92(2):022505, January 2008.

[94] Ki-Suk Lee and Sang-Koog Kim. Conceptual design of spin wave logic gates based on a machzehnder-type spin wave interferometer for universal logic functions. *Journal of Applied Physics*, 104(5):053909, September 2008.

[95] Alexander Khitun, Dmitri E. Nikonov, and Kang L. Wang. Magnetoelectric spin wave amplifier for spin wave logic circuits. *Journal of Applied Physics*, 106(12):123909, December 2009.

[96] M. P. Kostylev, A. A. Serga, T. Schneider, B. Leven, and B. Hillebrands. Spin-wave logical gates. *Applied Physics Letters*, 87(15):153501, October 2005.

[97] A. Khitun, Mingqiang Bao, and K.L. Wang. Spin wave magnetic NanoFabric: A new approach to spin-based logic circuitry. *IEEE Transactions on Magnetics*, 44(9):2141–2152, September 2008.

[98] K. Sekiguchi, K. Yamada, S. M. Seo, K. J. Lee, D. Chiba, K. Kobayashi, and T. Ono. Nonreciprocal emission of spin-wave packet in FeNi film. *Applied Physics Letters*, 97(2):022508, July 2010.

[99] Y. Kajiwara, K. Harii, S. Takahashi, J. Ohe, K. Uchida, M. Mizuguchi, H. Umezawa, H. Kawai, K. Ando, K. Takanashi, S. Maekawa, and E. Saitoh. Transmission of electrical signals by spin-wave interconversion in a magnetic insulator. *Nature*, 464(7286):262–266, March 2010.

[100] W. Eerenstein, N. D. Mathur, and J. F. Scott. Multiferroic and magnetoelectric materials. *Nature*, 442(7104):759–765, August 2006.

[101] Haiming Yu, O. d'Allivy Kelly, V. Cros, R. Bernard, P. Bortolotti, A. Anane, F. Brandl, R. Huber, I. Stasinopoulos, and D. Grundler. Magnetic thin-film insulator with ultra-low spin wave damping for coherent nanomagnonics. *Scientific Reports*, 4, October 2014.

[102] Yuriy G. Semenov, Xiaopeng Duan, and Ki Wook Kim. Voltage-driven magnetic bifurcations in nanomagnettopological insulator heterostructures. *Physical Review B*, 89(20):201405, May 2014.

[103] Xiaopeng Duan, Xiaodong Li, Yuriy G. Semenov, and Ki Wook Kim. Quasi-optical electron transport across a magnetically induced junction on a topological insulator surface. *Journal of Applied Physics*, 116(22):224301, December 2014.

[104] Dimitrie Culcer. Transport in three-dimensional topological insulators: Theory and experiment. *Physica E: Low-dimensional Systems and Nanostructures*, 44(5):860–884, February 2012.

[105] Dimitrie Culcer and S. Das Sarma. Anomalous hall response of topological insulators. *Physical Review B*, 83(24):245441, June 2011.

[106] J. G. Checkelsky, R. Yoshimi, A. Tsukazaki, K. S. Takahashi, Y. Kozuka, J. Falson, M. Kawasaki, and Y. Tokura. Trajectory of the anomalous hall effect towards the quantized state in a ferromagnetic topological insulator. *Nature Physics*, 10(10):731–736, October 2014.

[107] L. D. Alegria, H. Ji, N. Yao, J. J. Clarke, R. J. Cava, and J. R. Petta. Large anomalous hall effect in ferromagnetic insulator-topological insulator heterostructures. *Applied Physics Letters*, 105(5):053512, August 2014.

[108] Cui-Zu Chang, Jinsong Zhang, Minhao Liu, Zuocheng Zhang, Xiao Feng, Kang Li, Li-Li Wang, Xi Chen, Xi Dai, Zhong Fang, Xiao-Liang Qi, Shou-Cheng Zhang, Yayu Wang, Ke He, Xu-Cun Ma, and Qi-Kun Xue. Thin films of magnetically doped topological insulator with carrier-independent long-range ferromagnetic order. *Advanced Materials*, 25(7):1065–1070, February 2013.

[109] Naoto Nagaosa, Jairo Sinova, Shigeki Onoda, A. H. MacDonald, and N. P. Ong. Anomalous hall effect. *Reviews of Modern Physics*, 82(2):1539–1592, May 2010.

[110] Jinsong Zhang, Cui-Zu Chang, Peizhe Tang, Zuocheng Zhang, Xiao Feng, Kang Li, Li-li Wang, Xi Chen, Chaoxing Liu, Wenhui Duan, Ke He, Qi-Kun Xue, Xucun Ma, and Yayu Wang. Topology-driven magnetic quantum phase transition in topological insulators. *Science*, 339(6127):1582–1586, March 2013.

[111] Peter Hnggi and Fabio Marchesoni. Artificial brownian motors: Controlling transport on the nanoscale. *Reviews of Modern Physics*, 81(1):387–442, March 2009.

[112] V. I. Belinicher and B. I. Sturman. The photogalvanic effect in media lacking a center of symmetry. *Soviet Physics Uspekhi*, 23(3):199, March 1980.

[113] L. P. Kouwenhoven, B. J. van Wees, C. J. P. M. Harmans, J. G. Williamson, H. van Houten, C. W. J. Beenakker, C. T. Foxon, and J. J. Harris. Nonlinear conductance of quantum point contacts. *Physical Review B*, 39(11):8040–8043, April 1989.

[114] H. Linke, T. E. Humphrey, A. Lfgren, A. O. Sushkov, R. Newbury, R. P. Taylor, and P. Omling. Experimental tunneling ratchets. *Science*, 286(5448):2314–2317, December 1999.

[115] H. Linke, W. D. Sheng, A. Svensson, A. Lfgren, L. Christensson, H. Q. Xu, P. Omling, and P. E. Lindelof. Asymmetric nonlinear conductance of quantum dots with broken inversion symmetry. *Physical Review B*, 61(23):15914–15926, June 2000.

[116] A. Lfgren, C. A. Marlow, I. Shorubalko, R. P. Taylor, P. Omling, L. Samuelson, and H. Linke. Symmetry of two-terminal nonlinear electric conduction. *Physical Review Letters*, 92(4):046803, January 2004.

[117] C. A. Marlow, R. P. Taylor, M. Fairbanks, I. Shorubalko, and H. Linke. Experimental investigation of the breakdown of the onsager-casimir relations. *Physical Review Letters*, 96(11):116801, March 2006.

[118] H. Frster and M. Bttiker. Fluctuation relations without microreversibility in nonlinear transport. *Physical Review Letters*, 101(13):136805, September 2008.

[119] David Snchez and Markus Bttiker. Magnetic-field asymmetry of nonlinear mesoscopic transport. *Physical Review Letters*, 93(10):106802, September 2004.

[120] B. Szafran, M. R. Poniedziaek, and F. M. Peeters. Violation of onsager symmetry for a ballistic channel coulomb coupled to a quantum ring. *EPL (Europhysics Letters)*, 87(4):47002, August 2009.

[121] Jonathan Meair and Philippe Jacquod. Macroscopic coherent rectification in andreev interferometers. *Journal of Physics: Condensed Matter*, 24(27):272201, July 2012.

[122] Marius V. Costache and Sergio O. Valenzuela. Experimental spin ratchet. *Science*, 330(6011):1645–1648, December 2010.

[123] Shumpei Masuda and Katsuhiro Nakamura. Mesoscopic rectification in a quantum dot with spinorbit interaction. *Journal of Physics: Condensed Matter*, 19(21):216225, May 2007.

[124] Seokmin Hong, Vinh Diep, Supriyo Datta, and Yong P. Chen. Modeling potentiometric measurements in topological insulators including parallel channels. *Physical Review B*, 86(8):085131, August 2012.

[125] Jifa Tian, Isaac Childres, Helin Cao, Tian Shen, Ireneusz Miotkowski, and Yong P. Chen. Topological insulator based spin valve devices: Evidence for spin polarized transport of spin-momentum-locked topological surface states. *Solid State Communications*, 191:1–5, August 2014.

[126] A. A. Burkov and D. G. Hawthorn. Spin and charge transport on the surface of a topological insulator. *Physical Review Letters*, 105(6):066802, August 2010.

[127] P. Schwab, R. Raimondi, and C. Gorini. Spin-charge locking and tunneling into a helical metal. *EPL (Europhysics Letters)*, 93(6):67004, March 2011.

[128] Alex D. Gottlieb and Lisa Wesoloski. Bardeen's tunnelling theory as applied to scanning tunnelling microscopy: a technical guide to the traditional interpretation. *Nanotechnology*, 17(8):R57, April 2006. This article is a thorough tutorial on the traditional approach to Bardeen's tunnelling theory in the context of scanning tunnelling microscopy. We follow Duke's interpretation of Bardeen's theory as the tunnelling analogue of Oppenheimer's perturbation theory for field ionization of atomic hydrogen. We explain Oppenheimer's ideas, Fermi's golden rule, and Bardeen's formulae; and we derive the celebrated TersoffHamann formula using an argument due to Chen. Finally, we discuss the application of Bardeen's theory to scanning tunnelling microscopy beyond the TersoffHamann approximation.

[129] Wen-Yu Shan, Hai-Zhou Lu, and Shun-Qing Shen. Effective continuous model for surface states and thin films of three-dimensional topological insulators. *New Journal of Physics*, 12(4):043048, April 2010.

[130] A. Crpieux and C. Lacroix. Dzyaloshinskymoriya interactions induced by symmetry breaking at a surface. *Journal of Magnetism and Magnetic Materials*, 182(3):341–349, March 1998.

[131] A. N. Bogdanov and U. K. Rler. Chiral symmetry breaking in magnetic thin films and multilayers. *Physical Review Letters*, 87(3):037203, June 2001.

[132] P. C. Dorsey, S. E. Bushnell, R. G. Seed, and C. Vittoria. Epitaxial yttrium iron garnet films grown by pulsed laser deposition. *Journal of Applied Physics*, 74(2):1242–1246, July 1993.

[133] F. Giannazzo, S. Sonde, V. Raineri, and E. Rimini. Screening length and quantum capacitance in graphene by scanning probe microscopy. *Nano Letters*, 9(1):23–29, January 2009.

[134] J. Tworzydo, B. Trauzettel, M. Titov, A. Rycerz, and C. W. J. Beenakker. Sub-poissonian shot noise in graphene. *Physical Review Letters*, 96(24):246802, June 2006.

APPENDICES

Appendix A

Electrostatic control of magnetic anisotropy through TI surface states

For analysis of the underlying physics at the qualitative level, the easy axis rotation can be viewed as an effect of electron free energy reduction under the exchange interaction with proximate magnetic ions. When the magnetic layer has the magnetization in the in-plane direction, the interaction results in a shift of the TI Dirac cones in the momentum space. On the other hand, an energy gap can be generated between the Dirac cones and the dispersion becomes non-linear for the out-of-plane orientation with $M_z \neq 0$ (see Figure A.1 for the coordinate system). [22] From the thermodynamic point of view, the case with a band gap ($M_z \neq 0$) is expected to be energetically more favorable with lower electronic free energy than that with the shifted bands ($M_z = 0$) following a similar consideration demonstrated in bilayer graphene. [45] A departure of the Fermi energy ε_F from the energy level of the Dirac point ε_D suppresses this tendency: For $\varepsilon_F > \varepsilon_D$ the valence band energy decrease is partially compensated by the increase of energy in conduction electrons, whereas there are simply fewer active electrons in the case of $\varepsilon_F < \varepsilon_D$.

To proceed with a quantitative investigation, we define the chemical potential μ as $\mu = \varepsilon_F - \varepsilon_D$ and consider the thermodynamic potential of TI electrons interacting with the insulating magnet:

$$\Phi_e(\mu, T) = -T \sum_{b,\mathbf{k}} \ln \left(1 + \exp \frac{\mu - \varepsilon_{b,\mathbf{k}}}{T} \right) , \tag{A.1}$$

where the sum involves electronic bands b and wave vector $\mathbf{k}$ and T is the temperature in energy units. We are interested in the alteration of $\Phi_e(\mu, T)$ with the Fermi level varying near the Dirac point of the surface states. Thus, the rest of electronic states in Eq. (A.1) are irrelevant and the summation in $\Phi_e(\mu, T)$ can be safely restricted to the spectrum of surface Dirac fermions

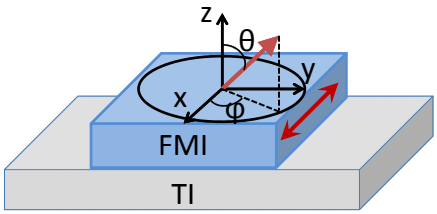

Figure A.1: Schematic illustration of the proposed structure consisting of an insulating ferromagnet (FMI) deposited on a TI. The controlling gate is not shown. The easy axis (two-sided arrow) is along the x direction without the gate voltage. The spherical polar coordinate θ and φ is used to describe the magnetization vector $\mathbf{M}$.

with 2D effective Hamiltonian [129]

$$H = \hbar v_F \left[\sigma \times \mathbf{k}\right] \cdot \hat{\mathbf{z}} + Dk^2 + \mathbf{G} \cdot \sigma \,, \tag{A.2}$$

where v_F is the electron Fermi velocity near the Dirac point, σ the Pauli matrix of electron spin, and D the material parameter for the quadratic term. The remaining expression in Eq. A.2 describes the energy of an electron spin in an effective exchange field $\mathbf{G} = \mathbf{m}G$ of the proximate magnet (in units of energy); $\mathbf{m} = \mathbf{M}/\left|\mathbf{M}\right|$ ensures the collinearity of the effective field and the magnetization ($\mathbf{M}$). Note that postulating homogeneous magnetization $\mathbf{M}$ over the nanomagnet interface assumes the negligible role of chiral symmetry breaking induced by the interface-mediated Dzyaloshinsky-Moriya interaction. [130] To ensure this, the interface must be smaller than the characteristic size of the chiral structures, $L_0 = 10ag_0/(g_0 - g)$ (where a and g are the lattice constant and the Landé factor of the magnetic material, respectively, and g_0=2.0023). [131] Since the g-factor of insulating or dielectric magnets such as $Y_3Fe_5O_{12}$ is essentially g_0 within the accuracy of measurement, [132] L_0 can be expected (at least, a few) orders of magnitude larger than a. Accordingly, the adopted postulation may be readily justified in typical nanoscale structures.

Introducing the polar and azimuthal angles θ and φ for vector $\mathbf{m}$ as shown in Figure A.1, the energy spectrum of the Hamiltonian in Eq. (A.2) can be expressed as

$$\varepsilon_{b,\mathbf{k}} = D_0 p^2 + b\sqrt{p^2 + G^2 + 2\mathbf{p} \cdot \hat{\mathbf{n}} G \sin\theta} \,. \tag{A.3}$$

Here $\mathbf{p} = \hbar v_F \mathbf{k}$ is the electron surface momentum in energy units, $\hat{\mathbf{n}} = -\sin\varphi\hat{\mathbf{x}} + \cos\varphi\hat{\mathbf{y}}$, $D_0 = D/\hbar^2 v_F^2$, and b ($= \pm 1$) denotes the conduction and valence bands, respectively. Equation (A.3) clearly illustrates the band reconstruction that lowers the energy of electrons near the top of valence band when $\mathbf{M}$ turns from the in-plane direction ($\theta = \pi/2$) to the out-of-plane position ($\theta = 0$). The valence band electrons ($b = -1$) contribute to this effect, while the conduction band electrons ($b = 1$) negate it. From the perspective of the magnetic-layer free energy, the proximity with a TI plays the role of a mediator enhancing the uniaxial magnetic anisotropy along the out-of-plane direction.

Following Eqs. (A.3) and (A.1), $\Phi_e(\mu, T)$ is an even function of the in-plane field $G\sin\theta$ that determines the dependence $\Phi_e(\mu, T) = -K_{\text{eff}}(\mu, T)\sin^2\theta$ and proportionality $K_{\text{eff}}(\mu, T) \sim G^2$ in the low-order expansion on G. A similar relation applies for $\Delta\Phi_e(\mu, T) = \Phi_e(\mu, T) - \Phi_e(0, T)$, which reflects the variable part of the TI mediated anisotropy energy

$$\Delta\Phi_e(\mu, T) = A\Delta K_{\text{eff}}(\mu, T)\sin^2\theta. \tag{A.4}$$

Here A is the area of the ferromagnet/TI interface and

$$\Delta K_{\text{eff}}(\mu, T) = f(\mu, T) D_0 G^2. \tag{A.5}$$

Computation of Eq. A.1 with Eq. A.3 confirms the validity of the definitions in Eq. A.4 and Eq. A.5. Accordingly, parameter $f(\mu, T)$ can be found numerically; the calculated outcome is plotted in Figure A.2 by using the material constants of Bi_2Se_3 ($v_F = 6 \times 10^7$ cm/s, $D = 13$ eV$\cdot\mathring{A}^2$). The results indicate the amplitude of anisotropy change with a surprisingly minor temperature dependence but a significant asymmetry in the chemical potential variation about the Dirac point (i.e., see $\mu > 0$ vs. $\mu < 0$). Qualitative understanding of the characteristic dependence can benefit from a simple analytical estimate $\Delta K_{\text{eff}} \simeq |\mu| G^2/8\pi\hbar^2 v_F^2$ that is obtained in the limit $T \to 0$ and $D \to 0$. The deduced proportionality of ΔK_{eff} on $|\mu|$ is a manifestation of the linear density of states (in energy) for the approximate conic dispersion relation [i.e., $D = 0$ in Eq. A.3]. Thus, the asymmetry observed in Figure A.2 about $\mu = 0$ can be explained by the unequal densities of states in the conduction ($b = 1$) and valence ($b = -1$) bands once the quadratic term of the energy dispersion ($D \neq 0$) is taken into account. When the strength of exchange interaction is assumed to be around $G = 40$ meV, [27] Eq. (A.5) predicts anisotropy variation as large as 0.5 meV/nm^2. In such a case, the contact area of tens of nanometers on each side may provide an eV-scale anisotropy energy change that guarantees a robust effect even at room temperature.

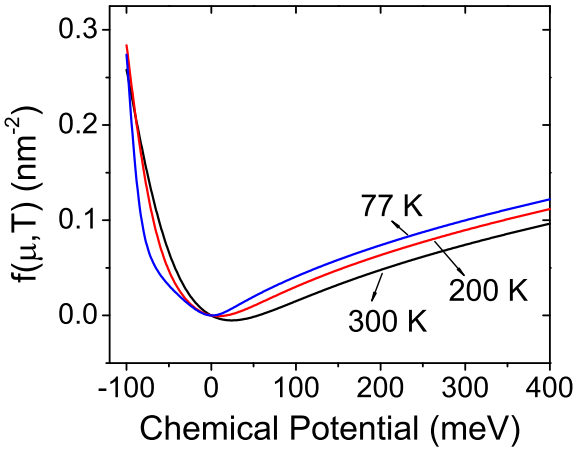

Figure A.2: Parameter $f(\mu, T)$ reflecting the TI mediated anisotropy as a function of chemical potential μ at temperatures 300 K, 200 K, and 77 K [see Eq. (A.5)]. Numerical calculations assume the material constants of Bi_2Se_3: $v_F = 6 \times 10^7$ cm/s and $D = 13$ eV$\cdot\mathring{A}^2$.

Appendix B

Spin splitting in graphene induced by multiple magnets

The Hamiltonian for the graphene electron can be expressed as:

$$H = \hbar v_F \mathbf{k} \cdot \sigma + 2G_0 \mathbf{m}(x) \cdot \mathbf{S}, \tag{B.1}$$

where $\mathbf{k}$ is the in-plane electron wave vector [$= -i(\partial/\partial x, \partial/\partial y, 0)$], σ the Pauli matrix vector defined on the graphene sublattice states, G_0 the exchange constant (as introduced previously), and $\mathbf{S}$ the electron spin operator. $\mathbf{m}(x)$ takes the value $\mathbf{m}_i$ of the corresponding region with the zero of the x axis set to the boundary between $\mathbf{M}_1$ and $\mathbf{M}_\mathrm{C}$: i.e., $\mathbf{m}(-L < x < 0) = \mathbf{m}_1$, $\mathbf{m}(0 < x < L_\mathrm{C}) = \mathbf{m}_\mathrm{C}$, $\mathbf{m}(L_\mathrm{C} < x < L_\mathrm{C} + L) = \mathbf{m}_2$, where L and L_C denote the length of the input/output and control magnets respectively; $\mathbf{m}_{1,2,\mathrm{C}}$ are their normalized magnetization. The narrow clearances between the magnets (i.e., the ungated regions) are ignored for simplicity as they are assumed to be smaller than the screening length which is typically several tens of nanometers in graphene[133]. The negligible spin-orbital interaction in graphene permits the eigenenergy to separate the contributions as $E_{k,\zeta} = E_k \pm \Delta_k(\mathbf{m}_1, \mathbf{m}_2, \mathbf{m}_\mathrm{C})$, where $2\Delta_k(\mathbf{m}_1, \mathbf{m}_2, \mathbf{m}_\mathrm{C})$ is the spin splitting of the orbital state k by the proximity exchange interaction. It is a function of $\mathbf{m}_1$, $\mathbf{m}_1$ and control magnet $\mathbf{m}_\mathrm{C}$. This is the crucial parameter that determines Eq. 3.4. If we pin $\mathbf{m}_1$ and $\mathbf{m}_\mathrm{C}$ ($\mathbf{m}_1 \perp \mathbf{m}_\mathrm{C}$), it becomes a function of $\mathbf{m}_2$ alone, which eases the discussion while capturing all the characters. Note that we take the NOT gate as the example here and the treatment of a COPY gate follows accordingly.

The estimation of spin splitting $2\Delta_k$ requires solving the eigenvalue problem of the Hamiltonian [Eq. (B.1)]. In each of the magnet capped regions ($Q = 1, 2, 3$), the eigenstates can be

expressed in the basis of $(+,1/2)$, $(+,-1/2)$, $(-,1/2)$, $(-,-1/2)$ as:

$$\Psi_Q = \begin{pmatrix} \psi_{Q,1} \\ \psi_{Q,2} \\ \psi_{Q,3} \\ \psi_{Q,4} \end{pmatrix}, \tag{B.2}$$

where $\pm$ represent the two lattice sites and $\pm 1/2$ the electron spin. By writing the general solution as a linear combination of the eigenstates, i.e.,

$$\Phi_Q = \sum_{j=1,2,3,4} c_{Q,j}\psi_{Q,j}e^{i\mathbf{k}_j\cdot\mathbf{r}}, \tag{B.3}$$

the problem is reduced to finding twelve coefficients $c_{Q,j}$ that are determined by the specific boundary conditions. Firstly, the wave function must satisfy the continuity condition at the two interfaces ($x = 0$ and $x = L_{\mathrm{C}}$). Secondly, the channel edges are treated as gapped graphene with additional term $E_g S_Z$ in Eq. (B.1) in the extreme limit $E_g \to \infty$. Then the calculations lead to:

$$\psi_{1,1} = -i\psi_{1,3}; \psi_{1,2} = -i\psi_{1,4}, \tag{B.4}$$

$$\psi_{3,1} = i\psi_{3,3}; \psi_{3,2} = i\psi_{3,4}. \tag{B.5}$$

For non-trivial solutions to exist, the following equation needs to be satisfied for the case $\mathbf{m}_2 = \mathbf{m}_1$:

$$\begin{aligned} 2\cos[2\frac{E}{\hbar v_F}(2L + L_{\mathrm{C}})] = 1 - \cos(2\frac{G_0}{\hbar v_F}L_{\mathrm{C}}) \\ - \cos(4\frac{G_0}{\hbar v_F}L) - \frac{1}{2}\{\cos[2\frac{G_0}{\hbar v_F}(2L - L_{\mathrm{C}})] \\ + \cos[2\frac{G_0}{\hbar v_F}(2L + L_{\mathrm{C}})]\}. \end{aligned} \tag{B.6}$$

In the simplest scenario of zero spin splitting [i.e., $G_0 = 0$], Eq. (B.6) reduces to

$$\cos[\frac{E}{\hbar v_F}(2L + L_{\mathrm{C}})] = 0 \tag{B.7}$$

that recovers the well-known result for graphene electron confinement: [64, 134]

$$E_{n,\zeta} = (n + \frac{1}{2})\frac{\pi\hbar v_F}{2L + L_{\mathrm{C}}}, \quad n = 0, \pm 1, ... \tag{B.8}$$

Note that each $E_{n,\zeta}$ in Eq. (B.8) is doubly degenerate in the spin index ζ ($=\pm\frac{1}{2}$). When the input and target magnets are coupled antiferromatically (i.e., $G_0 = \hbar v_F \pi / 2L_{\rm C}$), on the other hand, Eq. (B.6) results in

$$\sin[\frac{E}{\hbar v_F}(2L + L_{\rm C})] = 0. \tag{B.9}$$

This generates the spectrum

$$\begin{aligned} E_{n,\zeta} &= (n + \frac{1}{2})\frac{\pi\hbar v_F}{2L + L_{\rm C}} + \zeta\frac{\pi\hbar v_F}{2L + L_{\rm C}} \\ &= (n + \frac{1}{2})\frac{\pi\hbar v_F}{2L + L_{\rm C}} + \zeta\frac{2L_{\rm C}G_0}{2L + L_{\rm C}} \end{aligned} \tag{B.10}$$

Thus, the spin-splitting energy is

$$2\Delta_k(\mathbf{m}_2 = \mathbf{m}_1) = 2G_0\frac{\epsilon}{2 + \epsilon}. \tag{B.11}$$

where $\epsilon = L_{\rm C}/L$ (normally $\epsilon < 2$ for practical devices). Note that the no wavevector dependence is observed in the final result.

A similar procedure can be applied for the case of $\mathbf{m}_2 = -\mathbf{m}_1$ with $G_0 = \hbar v_F \pi / 2L_{\rm C}$. Straightforward algebra leads to the energy spectrum in the form

$$\cos[\frac{2E}{\hbar v_F}(2L + L_{\rm C})] = \cos(4\frac{G_0}{\hbar v_F}L), \tag{B.12}$$

$$E_{n,\zeta} = n\frac{\pi\hbar v_F}{2L + L_{\rm C}} + \zeta\frac{4LG_0}{2L + L_{\rm C}}. \tag{B.13}$$

The corresponding spin splitting is then

$$2\Delta_k(\mathbf{m}_2 = -\mathbf{m}_1) = 2G_0\frac{2}{2 + \epsilon}. \tag{B.14}$$

Following this method, the other cases for the $\mathbf{m}_2$ configurations directed along the $\mathbf{m}_C$ axis can also be calculated.

$$\Delta_k(\mathbf{m}_2 = \mathbf{m}_C) = \frac{1 + \epsilon}{2 + \epsilon}G_0; \tag{B.15}$$

$$\Delta_k(\mathbf{m}_2 = -\mathbf{m}_C) = \frac{1}{2 + \epsilon}G_0; \tag{B.16}$$

A further analysis indicates that $\mathbf{m}_2 = -\mathbf{m}_1$ results in the lowest thermodynamic potential for practical devices and is indeed the preferred state of the target magnet. It is worth noting that these results on energy splitting are expressed in terms of the ratio of the control magnet length over that of the unit cells, which can also be obtained by taking the length as normalization

factors for unrestricted graphene layer. Actually in this structure, the transverse quantum confinement is negligible for practical device size (e.g., 100 nm) as the thermal energy k_BT is well above quantization step $\Delta E = \pi/(2L + L_C)$ at room temperature.

Appendix C

Transmission calculation at arbitrary magnetic and electrostatic barrier

To simplify the notation, we make the momentum $\mathbf{p}$ and magnetization $\mathbf{m}$ have units in energy, i.e. $\mathbf{p} = (p_x, p_y) = \hbar v_F \mathbf{k}$ and $\beta \mathbf{m} \to \mathbf{m}$. The TI surface Hamiltonian thus gives:

$$\hat{H} = U + \sigma \times \mathbf{p} - \mathbf{m} \cdot \sigma \tag{C.1}$$

The resulting eigenenergy and eigenwavefunctions are

$$\begin{aligned} E &= U + b\sqrt{(p_x + m_y)^2 + (p_y - m_x)^2 + m_z^2} \\ \Phi &= \begin{bmatrix} \frac{(p_y - m_x) + i(p_x + m_y)}{|E-U| + b m_z} \\ 1 \end{bmatrix} \cdot e^{i[(p_x+m_y)x + (p_y - m_x)y]/\hbar v_F} \end{aligned} \tag{C.2}$$

where $b = 1$ for the conduction band and $b = -1$ for valence band. For the transmission problem through the magnetic valve as shown in Fig. 1, the $\hat{y}$ direction can be approximated as invariant as the valve boundary is along $\hat{y}$ and the width of the channel is normally several tens of nanometers that is large enough to ignore its influence. Thus, we use p_y and E as the base quantum numbers, and derive the momentum along $\hat{x}$ as

$$P_x = p_x + m_y = \sqrt{(E-U)^2 - (p_y - m_x)^2 - m_z^2} \tag{C.3}$$

Following the standard transmission problem solving procedure, the wavefunctions left to the valve, beneath the valve and right of the valve are written as:

$$
\begin{aligned}
\Phi^L &= A \begin{bmatrix} \frac{(p_y-m_x^L)+iP_x^L}{|E-U^M|+bm_z^L} \\ 1 \end{bmatrix} \cdot e^{i\left[P_x^L x+(p_y-m_x^L)y\right]/\hbar v_F} + B \begin{bmatrix} \frac{(p_y-m_x^L)-iP_x^L}{|E-U^M|+bm_z^L} \\ 1 \end{bmatrix} \cdot e^{i\left[-P_x^L x+(p_y-m_x^L)y\right]/\hbar v_F} \\
\Phi^M &= C \begin{bmatrix} \frac{(p_y-m_x^M)+iP_x^M}{|E-U^M|+bm_z^M} \\ 1 \end{bmatrix} \cdot e^{i\left[P_x^M x+(p_y-m_x^M)y\right]/\hbar v_F} + D \begin{bmatrix} \frac{(p_y-m_x^M)-iP_x^M}{|E-U^M|+bm_z^M} \\ 1 \end{bmatrix} \cdot e^{i\left[-P_x^M x+(p_y-m_x^M)y\right]/\hbar v_F} \\
\Phi^R &= F \begin{bmatrix} \frac{(p_y-m_x^R)+iP_x^R}{|E-U^R|+bm_z^R} \\ 1 \end{bmatrix} \cdot e^{i\left[P_x^R x+(p_y-m_x^R)y\right]/\hbar v_F}
\end{aligned}
\tag{C.4}
$$

where the superscript L, M, R represent the regions from left to right respectively. If the magnetic valve stretches from $x = 0$ to $x = L$, the boundary conditions gives $\Phi^L(x = 0) = \Phi^M(x = 0)$ and $\Phi^M(x = L) = \Phi^R(x = L)$. Following relations between the coefficients A, B, C, D, F can be derived:

$$
\begin{aligned}
C &= \frac{1}{2} e^{i(P_x^R - P_x^M)L/\hbar v_F} \left(1 + \frac{|E-U^M| + bm_z^M}{|E-U^R| + bm_z^R} \frac{p_y - m_x^R + iP_x^R}{iP_x^M} - \frac{p_y - m_x^M}{iP_x^M}\right) F \\
D &= \frac{1}{2} e^{i(P_x^R + P_x^M)L/\hbar v_F} \left(1 - \frac{|E-U^M| + bm_z^M}{|E-U^R| + bm_z^R} \frac{p_y - m_x^R + iP_x^R}{iP_x^M} + \frac{p_y - m_x^M}{iP_x^M}\right) F \\
A &= \frac{1}{2}[\left(1 + \frac{|E-U^L| + bm_z^L}{|E-U^M| + bm_z^M} \frac{p_y - m_x^M + iP_x^M}{iP_x^L} - \frac{p_y - m_x^L}{iP_x^L}\right) C \\
&\quad + \left(1 + \frac{|E-U^L| + bm_z^L}{|E-U^M| + bm_z^M} \frac{p_y - m_x^M - iP_x^M}{iP_x^L} - \frac{p_y - m_x^L}{iP_x^L}\right) D] \\
B &= \frac{1}{2}[\left(1 - \frac{|E-U^L| + bm_z^L}{|E-U^M| + bm_z^M} \frac{p_y - m_x^M + iP_x^M}{iP_x^L} + \frac{p_y - m_x^L}{iP_x^L}\right) C \\
&\quad + \left(1 - \frac{|E-U^L| + bm_z^L}{|E-U^M| + bm_z^M} \frac{p_y - m_x^M - iP_x^M}{iP_x^L} + \frac{p_y - m_x^L}{iP_x^L}\right) D]
\end{aligned}
\tag{C.5}
$$

The resulting transmission probability is given as

$$
T_0 = |\frac{E}{A}| \cdot |\frac{P_x^R}{P_x^L}| \tag{C.6}
$$

For a certain energy, summing up over all the available p_y state gives the energy dependent transmission probability T as used in Eq. 3.2. It should be noted that in this derivation, T is a function of the magnetic and electrostatic potential at all three regions. In the main paper, we assume the two guiding strips have pinned magnetization along $-\hat{y}$. The electrostatic potential is assumed the same over the whole channel to avoid unnecessary complexity due to electrostatic

barriers. This results in a uniform gate bias dependent TI surface potential. Consequently, the transmission probability becomes a function of electron energy, gate bias and the magnetization of the switching valve.

Appendix D

Phenomenological modeling of TI surface spin dependent transport

D.1 Ballistic coupling coefficient between electrodes

With the only assumption of spin conservation, the coupling between the electrodes and the TI surface [i.e., $\langle\psi^{\mathrm{FM}}(E,s)|\Delta V_b|\psi^{\mathrm{TI}}_{\beta}(k_x,k_y)\rangle$] follows the spin selective rule, which results in the coupling coefficient dependent on the TI electron momentum as shown by Eq. (3) in the main paper. Here, it should be noted that the states in the electrode is described by the energy E and the spin polarization s, while that in the TI is by the momentum according to the linear dispersion relation and the spin-momentum interlock. The overall physical picture for the direct ballistic coupling between two electrodes can be constructed by treating the TI surface states as the intermediary. Then, by taking advantage of the overlap integral through the tunnel barrier mentioned above, a formal expression for this coupling coefficient between electrodes can be written as:

$$t^{\mathrm{M}}_{\mathrm{M}}(E)=\sum_{k'_x}\sum_{k'_y}\frac{\langle\psi^{\mathrm{FM}}_{R}(E,s)|\Delta V_b|\psi^{\mathrm{TI}}_{\beta}(k'_x,k'_y)\rangle\langle\psi^{\mathrm{TI}}_{\beta}(k'_x,k'_y)|\Delta V_b|\psi^{\mathrm{FM}}_{L}(E,s)\rangle e^{i\beta k'_x L}}{E-E'+i0}, \tag{D.1}$$

where the subscripts for the FM states represent the electrode on the left (L) or the right (R) and $(\beta k'_x, k'_y)$ is the momentum of the TI surface state that couples to the electrodes. As in the main paper, we set k'_x a positive value and use β to denote the direction of electron flow. Given a width W for the channel, k'_y is then quantized as $k'_y = m\pi/W$, where $m = 0, \pm1, \pm2, \cdots$. If the electron has an energy $E' = \hbar v_F\sqrt{{k'_x}^2+{k'_y}^2}$, the upper bound for $|m|$ is determined accordingly by E'; i.e., $|m| \leq E'W/\pi\hbar v_F$. When the width is sufficiently large such that the quantization step π/W is negligible compared to $E'/\hbar v_F$, the summation over all possible k'_y

can be substituted by an integral. The same applies to the x direction as well. Indeed, we assume that the x direction is unconstrained, so k'_x essentially becomes continuous. In addition, it is more suitable to average the result over the system dimension. We adopt the change of notation to let $t_{\mathrm{M}}^{\mathrm{M}}$ denote such an averaged value hereinafter, i.e.,

$$\begin{aligned} t_{\mathrm{M}}^{\mathrm{M}}(E) &= \int_{-\infty}^{\infty} \int_{-\infty}^{\infty} \frac{\langle \psi_R^{\mathrm{FM}}(E)|\Delta V_b|\psi_\beta^{\mathrm{TI}}(k'_x,k'_y)\rangle\langle\psi_\beta^{\mathrm{TI}}(k'_x,k'_y)|\Delta V_b|\psi_L^{\mathrm{FM}}(E)\rangle}{E-E'+i0} \frac{k'_x}{\sqrt{{k'_x}^2+{k'_y}^2}} dk'_x dk'_y \\ &= \int_{-\infty}^{\infty} \int_{-\pi/2}^{\pi/2} \frac{\langle \psi_R^{\mathrm{FM}}(E)|\Delta V_b|\psi_\beta^{\mathrm{TI}}(E',\theta)\rangle\langle\psi_\beta^{\mathrm{TI}}(E',\theta)|\Delta V_b|\psi_L^{\mathrm{FM}}(E)\rangle}{E-E'+i0} \cos\theta \frac{E'}{\hbar v_F} d\theta dE'. \end{aligned} \tag{D.2}$$

This is a quasi-1D treatment that is valid given the invariance over y. The second expression indicates the change of variables according to $dk'_x dk'_y = \frac{E'}{\hbar v_F} dE' d\theta$ (i.e., the E-k relation). In addition, the phase factor $e^{ik'_x L}$ is dropped from the equation as it is for the interference of electrons with different wavevectors. The interference phenomenon requires very stringent conditions that are generally not supported in the realistic systems at room temperature. The $\cos\theta$ factor, or the $\frac{k'_x}{\sqrt{{k'_x}^2+{k'_y}^2}}$ term, explicitly accounts for the projection along the channel direction. The integral over the energy can be carried out by using Cauchy's residue theory. This is intuitively expected as the resonant case with $E' = E$ dominates the contribution. Thus, Eq. (D.2) becomes:

$$t_{\mathrm{M}}^{\mathrm{M}}(E) = -i\pi \int_{-\pi/2}^{\pi/2} \langle \psi_R^{\mathrm{FM}}(E)|\Delta V_b|\psi_\beta^{\mathrm{TI}}(E,\theta)\rangle\langle\psi_\beta^{\mathrm{TI}}(E,\theta)|\Delta V_b|\psi_L^{\mathrm{FM}}(E)\rangle \cos\theta d\theta. \tag{D.3}$$

Combined with the overlap integral given in Eq. (3) of the main paper, the coupling between the two electrodes through the TI surface states is finally given as (with $k'_x = E\cos\theta/\hbar v_F$ and $k'_y = E\sin\theta/\hbar v_F$):

$$t_{\mathrm{M}}^{\mathrm{M}}(E) = -i\pi \int_{-\pi/2}^{\pi/2} |\tau_0 \frac{E - s\hbar v_F(\beta k'_x + ik'_y)}{2E}|^2 \cos\theta d\theta = -i\pi|\tau_0|^2 \frac{E}{\hbar v_F}\left(1 - \frac{\pi}{4} s\beta\right). \tag{D.4}$$